Title

Investigations of Human Telomerase Recruitment and Catalysis

Author

Badstuebner, Mareike

Publication Date

2024

UNIVERSITY OF CALIFORNIA

SANTA CRUZ

INVESTIGATIONS OF HUMAN TELOMERASE RECRUITMENT AND CATALYSIS

A dissertation submitted in partial satisfaction
of the requirements for the degree of

DOCTOR OF PHILOSOPHY

In

CHEMISTRY

by

Mareike Badstübner
September 2024

The Dissertation of Mareike Badstübner is approved:

Professor Michael Stone, chair

Professor Seth Rubin

Professor Carol Greider

Peter Biehl
Vice Provost and Dean of Graduate Studies

Table of Contents Page

Chapter 1: Introduction

Chapter 2: Real-time detection of human telomerase DNA synthesis by multiplexed single-molecule FRET

Chapter 3: The interplay of TPP1-POT1-TIN2 and DNA structure during telomerase recruitment to telomeres

Chapter 4: 6-thio-2’-deoxyguanosine drives telomere shortening by impairing telomerase translocation after nucleotide addition

Chapter 5: Ongoing studies for *in vitro* investigations into telomere biology

LIST OF FIGURES AND TABLES

CHAPTER 1

CHAPTER 2

CHAPTER 3:

CHAPTER 4:

CHAPTER 5:

ABSTRACT

Mareike Badstübner

Investigations of human telomerase recruitment and catalysis

Telomeres are protective DNA caps that terminate each chromosome in eukaryotic cells. In humans, telomeres are comprised of hexameric GGTTAG repeats and form a single-stranded 3’ DNA overhang. To distinguish chromosome ends from DNA repair machinery, telomeres are bound by protein complexes called shelterin. Shortening of telomeres with each cell cycle can compromise the protective properties of telomeres. Critically short telomeres result in senescence and eventually apoptosis of these cells. In highly proliferative cells, such as bone marrow cells, telomere length is maintained by the enzyme telomerase. While mutations that compromise telomerase activity leads to fatal diseases such as dyskeratosis congenita, aberrant reactivation of telomerase activity in somatic tissues confers immortality in about 90% of cancer cells. This makes telomerase an attractive target for therapeutic intervention for these diseases.

The catalytically active core of telomerase is minimally comprised of protein (telomerase reverse transcriptase or hTERT in humans) and RNA (telomerase RNA or hTR in humans) components. During S-phase of the cell cycle, telomerase is recruited to telomeres by shelterin components. Once at the 3’ end telomerase uses its internal RNA template to add GGTTAG repeats to the 3’ end of telomeres. After each round of repeat addition, the enzyme must rearrange its RNA template in a process called repeat addition processivity.

In this thesis, I interrogate several aspects of telomerase activity. In chapter two, I focus on a novel single-molecule Förster Resonance Energy Transfer (smFRET) methodology that leverages existing sequencing machinery to observe the incorporation of nucleotides by telomerase in real-time, allowing us to study the kinetic properties of the telomerase catalytic cycle. Chapter three describes my approach to investigate how DNA structure formation in telomeres and presence of shelterin protein components regulate telomerase recruitment efficiency *in vitro*. I show that interaction of the shelterin subcomplex TPP1-POT1-TIN2 (TPT)

with telomerase positively regulates telomerase recruitment efficiency while potassium-induced ssDNA structure negatively regulates telomerase recruitment, even in the presence of TPT. In chapter 4, I study how use of the nucleotide analog 6-thio-dGTP by telomerase leads to inhibition of telomerase activity and show that incorporation of the analog leads to telomerase staling on the ssDNA, possibly due to defects in the template rearrangement mechanism. Finally, in the last chapter I discuss single molecule approaches that can advance ongoing studies of telomerase recruitment and catalysis and the challenges that these studies must overcome to be completed.

ACKNOWLEDGEMENTS

First and foremost, I would like to express my deepest gratitude to my advisor, Dr. Michael Stone. Your unwavering patience, belief in my potential, and insightful critiques have been instrumental in my growth as a scientist. You inspired me to pay attention to the finer details in every experiment and nurtured my curiosity to explore every variable. Your guidance, especially during the unprecedented challenges of the COVID-19 pandemic, helped me maintain my morale and perseverance. For all these reasons and more, I am deeply grateful.

I am also immensely thankful to my thesis committee members, Dr. Seth Rubin and Dr. Carol Greider. Your scientific expertise has been invaluable in critically evaluating the strengths and weaknesses of my research. Your feedback and advice have significantly contributed to the refinement of this thesis.

To all the members of the Stone Lab, past and present, I extend my heartfelt thanks. The camaraderie we shared made the graduate school journey more bearable. From collectively agonizing over failed experiments to brainstorming solutions to experimental bottlenecks, your support has been essential. The memories of our office shenanigans and intellectual debates will be cherished always.

I would also like to express my gratitude to the staff at PSB and the Chemistry and Biochemistry Department, who provided constant support and assistance, particularly during the difficulties posed by the pandemic. Your help in navigating my studies and administrative challenges was greatly appreciated.

A special thanks to our collaborators—Sam Sanford, Patricia Opresko, Kelly Nguyen, Zala Sekne, George Ghanim, and Neal Lue. Thank you for entrusting me with your scientific endeavors and for your invaluable contributions to this research.

To my family, both in Germany and the United States, thank you for your endless encouragement and inspiration. Your unwavering support over the years has been my backbone, motivating me to strive for excellence every day.

Finally, to my partner, Mark—thank you for always pushing me to face my fears in the name of growth, whether in the lab or on a rock cliff. Your adventurous spirit and ability to distract and motivate me during the tougher times of graduate school have been invaluable. I eagerly look forward to starting our life together.

CHAPTER 1: INTRODUCTION

The linear ends of eukaryotic chromosomes terminate in DNA caps known as telomeres. Human telomeres comprise six-nucleotide tandem repeats (5'-GGTTAG-3') that form a 9-15 kilobase pair long double stranded (dsDNA) and a 150-300 nucleotide single stranded (ssDNA) G-rich DNA region at each chromosome end.[1,2,3] The proper maintenance and protection of telomeres is essential to the genomic integrity of chromosomes and the survival of highly proliferative cells. Telomeric DNA is bound by telomere-specific protein complexes called shelterin, which prevent the end of chromosomes from being recognized as DNA damage by

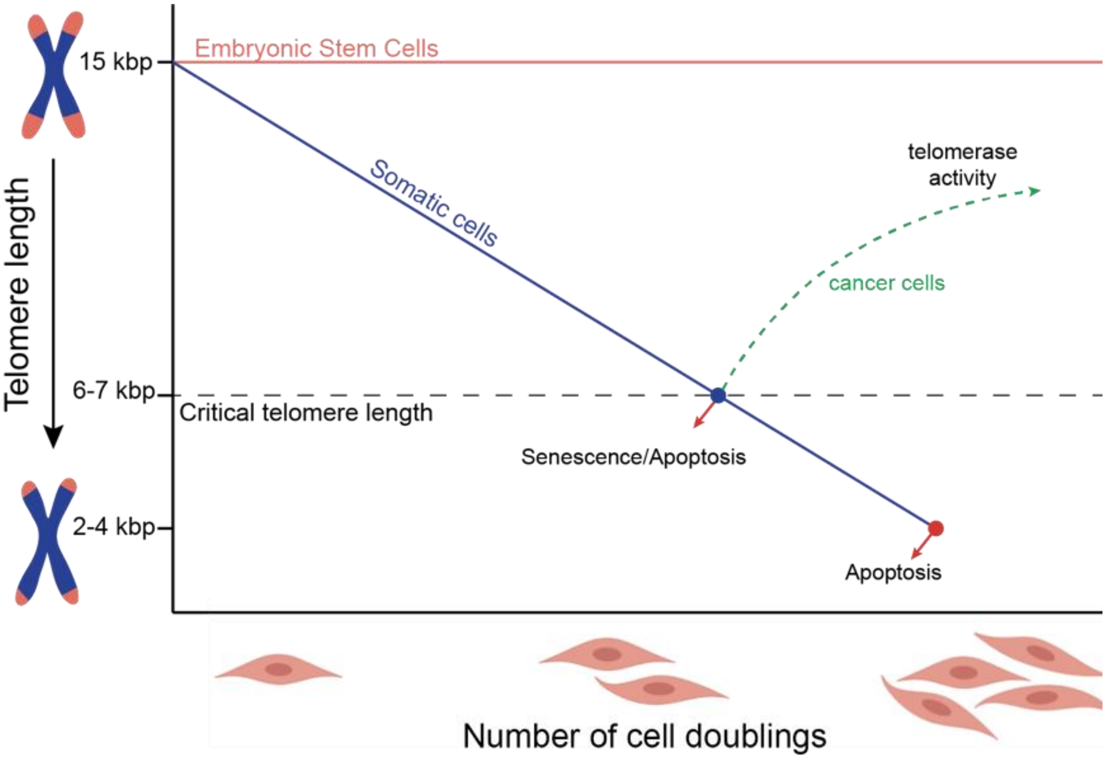

Figure 1. Telomere length is dependent on number of cell divisions and length maintenance mechanisms. In healthy somatic tissues, telomeres shorten with each cell division due to the end-replication problem. Once telomeres reach a critical length, cells can undergo senescence or apoptosis (blue dot) while further shortening to a critically short telomere eventually results in apoptosis (red dot). In 90% of cancerous tissues, telomere length is maintained by the aberrant reactivation of the enzyme telomerase (dashed green line). This increases the cell's proliferative potential and allows the cell to divide indefinitely, resulting in immortality.

DNA repair machinery.[4] This prevents non-homologous end-joining of chromosomes which would lead to cell death. Due to the end-replication problem, in which the DNA replication machinery is unable to completely replicate each DNA strand, telomeres shorten with every cell division. Once telomere shortening leads to critically short telomeres, healthy somatic cells enter senescence or undergo apoptosis (Figure 1).[5,6]

However, aberrant elongation of telomeres confers immortality in about 90% of cancer cells.[7,8] In these cells, as well as in healthy highly proliferative tissues, telomere length is maintained either by enzymatic addition of nucleotides by telomerase or by alternative lengthening of telomeres (ALT) pathways.[9,10] Telomerase is active in all tissues until shortly after birth.[11] It is then deactivated in most somatic tissues, contributing to the ageing of these

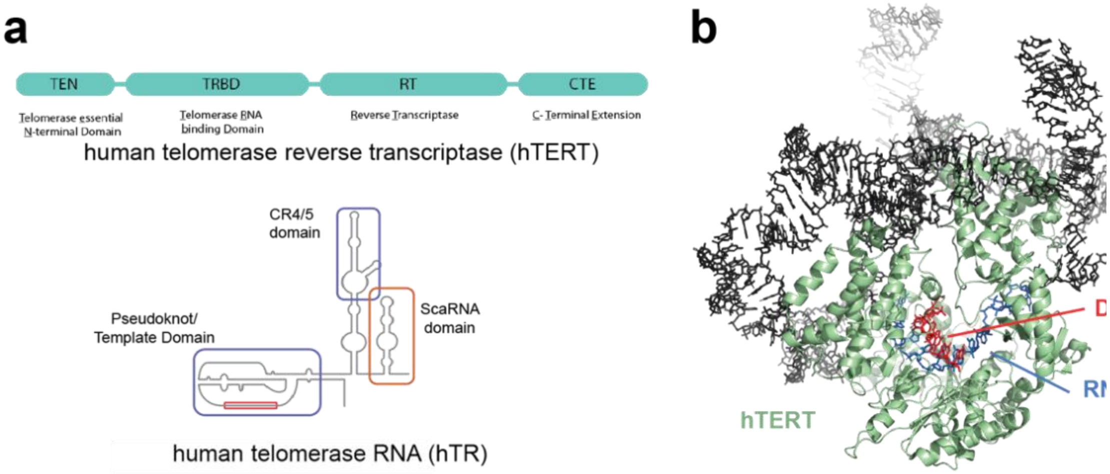

Figure 2. Telomerase components and structure of the catalytic core a. Cartoon representation of the molecular structure of the catalytic lobe of human telomerase bound to a TTAGGG$_3$ primer (PDB: 7BG9). Shown are the protein (hTERT, green) and RNA (hTR, gray) subunits as well as the RNA template region (blue) and DNA primer (red). **b.** The catalytic cycle of telomerase. Addition of dNTPs to a DNA-telomerase complex results in nucleotide addition until the template region is exhausted. Template translocation is then triggered in a process called repeat addition processivity (RAP). Template translocation increases the risk of DNA dissociation from the enzyme, posing a unique challenge to telomerase.

tissues over time due to the erosion of telomere length and other processes[12,13]. Elongation of telomeres by the enzyme telomerase ensures that highly proliferative cells can divide indefinitely, and that the genomic integrity of these cells is properly maintained (Figure 1).

The enzyme telomerase is a ribonucleoprotein minimally comprised of telomerase RNA (hTR in humans) and telomerase reverse transcriptase (hTERT in humans)[14]. Telomerase extends the 3' end of telomeres by binding the 3' ssDNA at the end of chromosome. Using its internal RNA template, telomerase adds 5'-GGTTAG-3' ssDNA repeats to the telomere, which is followed by template repositioning[15]. The use of an internal RNA template that needs to be repositioned after each repeat addition for continued activity is unique to telomerase and is termed repeat addition processivity (RAP) [16–18]. The molecular mechanism that underlies template repositioning is not well understood. However, previous studies have established that both G-quadruplex (GQ) formation in the G-rich telomere ssDNA and interaction with shelterin protein components increase RAP [19–22]. GQs are stable DNA structures that, among other G-rich sequences in the genome, form between three G-quartets of four telomeric repeats (Fig. 3A). These structures are stabilized by monovalent potassium ions, while the small atomic radius of lithium ions are insufficient for robust stabilization of GQs [23] .*In vitro* studies have found that the absence of GQ formation in telomeres decreases the RAP efficiency of telomerase (Fig. 3C).[22] Further, it has been shown that GQs in the 3' region of telomere DNA negatively regulates telomerase activity *in vitro* (Fig. 3B).[24] This suggests that GQs both positively and negatively regulate telomerase activity in cells, but more research has to be conducted to further investigate the role of GQs in telomerase activity.

Telomerase activity is also regulated by shelterin. The shelterin complex specifically binds telomeres and is comprised of six proteins.[4] Homologs of the shelterin complex exist in and are essential to telomerase activity in all eukaryotes. In humans, each shelterin complex minimally comprises the dsDNA binding homodimers TRF1 and TRF2, TIN2 and TPP1 or the ssDNA binding POT1, which tethers TPP1 and TIN2 to dsDNA region of the telomere (Fig. 4). While the number and distribution of shelterin complexes on each telomere is unknown, it has been established that they are responsible for two critical functions.

First, the occupation of telomere DNA by the DNA-binding components of shelterin (TRF1/2 and POT1) render it inaccessible to DNA repair machinery and other DNA binding factors. Improper protection of telomeres due to the lack of one or more shelterin components can lead to chromosome end-joining or predisposition to cancer.[25,26] For example, mutations that compromise the ssDNA binding abilities of POT1 lead to fused chromosomes in human HeLa cells and predispose humans to cancer.[27–29] Secondly, the heterotrimer TPP1-POT1-TIN2 (TPT) is crucial for proper telomere recruitment and regulation *in vivo.*[30,31]In human cells, telomerase is recruited to telomeres by an interaction with the shelterin component TPP1.[32,33] Studies have discovered that a region in the OB domain of TPP1 termed the TEL (TPP1 asparagine and leucine rich) patch interacts with the TEN (telomerase essential domain) of telomerase.[33] Disruptions of this interaction cause disease phenotypes in humans and results

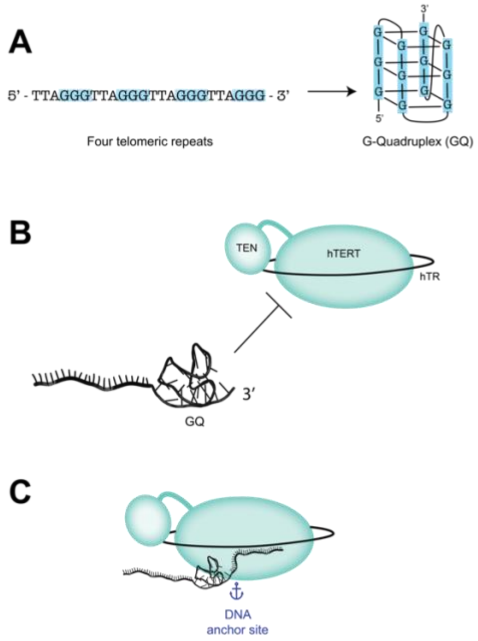

4 A. Cartoon representation of four telomeric ssDNA repeats folding into a stable GQ structure.**B.** GQ formation at the 3' end of telomeres has been shown to inhibit telomerase activity (GQ structure PDB: 6XT7). **C.** GQ-formation in nascent DNA during the telomerase catalytic cycle stimulates telomerase processivity.

in inactivity of the enzyme in human cell lines.[34,35] However, how the shelterin complex achieves proper telomere protection from DNA repair mechanisms while simultaneously promoting telomerase activity remains unclear.

In chapter II of this thesis, I focus on the development of a novel single-molecule Förster Resonance Energy Transfer (smFRET) approach to study the kinetics of nucleotide addition and RAP by telomerase *in vitro*. Utilizing the PacBio RS system and dye-labeled nucleotides, DNA primer and telomerase, we were able to observe incorporation of nucleotides into a DNA primer by telomerase in real time. The RS setup uses a zero-mode-waveguide (ZMW) approach which enables the use of biologically relevant concentrations of dye-labeled dATP and dGTP. We achieved the observation of multiple repeat synthesis by telomerase and discovered a significant time gap between dG6 and dG1/2, referring to $G_1G_2TTAG_6$ repeat positions, incorporation. We hypothesize that this pause represents template translocation kinetics. In addition, dG1/2 incorporation occurred in blocks of dG signal in the telomerase active site, rather than in pulses. We hypothesize that this difference in dG6 and dG1/2 incorporation kinetics point to structural rearrangements in hTERT or DNA repositioning that are separate from template relocation. The development of this novel method to study the

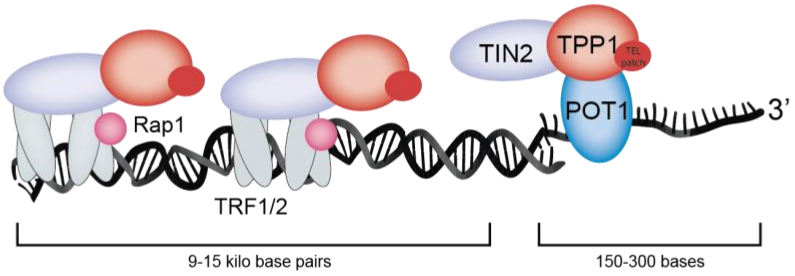

Figure 4. Cartoon Representation of shelterin bound to telomere DNA. The dsDNA binding proteins TRF1 and TRF2 (grey) bind the double-stranded portion of the telomere. Rap1 (pink) binding to TRF1/2 increases their specificity for telomere DNA. TRF1/2 also bind TIN2, which in turn tethers TPP1 and POT1 to the complex. POT1 binds single-stranded DNA (blue) while TPP1 (red) is responsible for telomerase recruitment. The heterotrimer POT1-TPP1-TIN2 (TPT) is essential for telomerase activity and processivity *in vivo*.

kinetics of telomerase catalysis enables future studies of the effect of DNA structure and the presence of shelterin components on telomerase kinetics.

In chapter III, I focus on how DNA structure and shelterin components affect telomerase recruitment efficiency *in vitro*. Our study builds on recent cryo-EM advances of the structure of telomerase bound to DNA primer and the shelterin subcomplex TPP1-POT1-TIN2 (TPT).[36] The structure led to a new model of TPT-mediated telomerase recruitment. This model proposes that TPP1 and POT1 collaboratively facilitate telomerase association with telomeric DNA. While TPP1 stabilizes the flexible TEN domain of telomerase, POT1 enhances DNA primer interaction with the TEN and IFD domains of hTERT. However, these structural advances were unable to resolve the details of the dynamics of TPT-mediated telomerase recruitment. In addition, the study lacks a detailed analysis of the role of GQ formation in telomerase recruitment, and how resolution of GQs by POT1 can promote telomerase binding to ssDNA.[19,37] Here, I use a smFRET approach to determine the effect of GQ formation and TPT presence on the recruitment efficiency of telomerase *in vitro*. Our findings suggest that while the interaction between the telomerase TEN domain and the TPP1 TEL patch promotes telomerase recruitment, it cannot overcome the negative effect of DNA structure formation. We propose a model in which in the cell, GQ formation at the single-stranded telomere DNA tail ensures continued telomere protection while shelterin serves to sequester telomerase and increases the probability of successful telomerase binding to the 3' end.

In chapter IV, I focus on how incorporation of the dGTP analog 6-thio-dGTP into telomere DNA leads to telomerase inhibition.[38,39] Treatment of cancer patients with 6-thio-dGTP has been shown to cause rapid telomerase-dependent telomere shortening and cell death in cancerous tissues but not in healthy cells.[40,41] This positions 6-thio-dGTP as an attractive candidate for a telomerase-targeted chancer therapy. However, the molecular mechanism by which the nucleotide analog inhibits telomerase is not well understood. Here, I present a study that was conducted in collaboration with the Opresko Lab at University of Pittsburgh. Our results suggest that incorporation of 6-thio-dGTP into telomere DNA does not stall telomerase by preventing the DNA-RNA hybrid from forming in the active site, which could lead to dissociation of the enzyme. Instead, results from a smFRET-based telomerase assay shows that telomerase does not dissociate from the DNA primer but instead forms a non-extendable state of the RNA-DNA hybrid in the active site. The details of this 6-thio-dGTP-induced non-extendable state are still unknown and invite further, potentially structure-based studies.

In chapter V of this thesis, I discuss studies that were started, but not completed during my training and suggest potential future experiments. First, I discuss how we can leverage our advances in ZMW-based smFRET assays to dissect the mechanism of RAP promotion by TPT. Next, I discuss preliminary data from real-time single-molecule FRET experiments using our lab’s total internal reflection (TIRF) microscopy setup that shed light on the mechanism and dynamics of telomerase recruitment in real time. Further, I discuss how changing experiment conditions could provide novel insight into the effectors of telomerase recruitment efficiency. I then discuss how telomerase recruitment and activity studies could be advanced to more closely mimic intracellular conditions of the telomere, such as the inclusion of chromatin and a complete set of shelterin components. Finally, I discuss the ongoing collaborative effort to elucidate telomere maintenance mechanisms beyond telomerase. Primase-Polymerase-alpha is responsible for C-strand fill in after telomerase activity and has been shown to be stimulated by the telomere-specific complex CST.[42] The primase subunit first synthesizes a RNA primer, that is then handed off to the polymerase subunit which then adds nucleotides to the RNA to create an RNA-DNA hybrid.[43] Here, I will describe preliminary results of a study that aims to elucidate the mechanism by which the DNA-RNA hybrid is handed off from the primase to the polymerase active site.

References

1. All gene-sized DNA molecules in four species of hypotrichs have the same terminal sequence and an unusual 3’ terminus. | PNAS. Accessed July 26, 2024. https://www.pnas.org/doi/abs/10.1073/pnas.78.5.3015

2. Canela A, Vera E, Klatt P, Blasco MA. High-throughput telomere length quantification by FISH and its application to human population studies. *Proc Natl Acad Sci U S A*. 2007;104(13):5300-5305. doi:10.1073/pnas.0609367104

3. Wright WE, Tesmer VM, Huffman KE, Levene SD, Shay JW. Normal human chromosomes have long G-rich telomeric overhangs at one end. *Genes Dev*. 1997;11(21):2801-2809. doi:10.1101/gad.11.21.2801

4. de Lange T. Shelterin: the protein complex that shapes and safeguards human telomeres. *Genes Dev*. 2005;19(18):2100-2110. doi:10.1101/gad.1346005

5. Takai H, Smogorzewska A, de Lange T. DNA damage foci at dysfunctional telomeres. *Curr Biol CB*. 2003;13(17):1549-1556. doi:10.1016/s0960-9822(03)00542-6

6. d’Adda di Fagagna F, Reaper PM, Clay-Farrace L, et al. A DNA damage checkpoint response in telomere-initiated senescence. *Nature*. 2003;426(6963):194-198. doi:10.1038/nature02118

7. Shay JW, Bacchetti S. A survey of telomerase activity in human cancer. *Eur J Cancer Oxf Engl 1990*. 1997;33(5):787-791. doi:10.1016/S0959-8049(97)00062-2

8. Robinson NJ, Schiemann WP. Telomerase in Cancer: Function, Regulation, and Clinical Translation. *Cancers*. 2022;14(3):808. doi:10.3390/cancers14030808

9. Greider CW, Blackburn EH. Identification of a specific telomere terminal transferase activity in Tetrahymena extracts. *Cell*. 1985;43(2 Pt 1):405-413. doi:10.1016/0092-8674(85)90170-9

10. Sohn EJ, Goralsky JA, Shay JW, Min J. The Molecular Mechanisms and Therapeutic Prospects of Alternative Lengthening of Telomeres (ALT). *Cancers*. 2023;15(7):1945. doi:10.3390/cancers15071945

11. Cong YS, Wright WE, Shay JW. Human Telomerase and Its Regulation. *Microbiol Mol Biol Rev*. 2002;66(3):407-425. doi:10.1128/MMBR.66.3.407-425.2002

12. Harley CB, Vaziri H, Counter CM, Allsopp RC. The telomere hypothesis of cellular aging. *Exp Gerontol*. 1992;27(4):375-382. doi:10.1016/0531-5565(92)90068-b

13. Garcia CK, Wright WE, Shay JW. Human diseases of telomerase dysfunction: insights into tissue aging. *Nucleic Acids Res*. 2007;35(22):7406-7416. doi:10.1093/nar/gkm644

14. Feng J, Funk WD, Wang SS, et al. The RNA component of human telomerase. *Science*. 1995;269(5228):1236-1241. doi:10.1126/science.7544491

15. Wu RA, Upton HE, Vogan JM, Collins K. Telomerase Mechanism of Telomere Synthesis. *Annu Rev Biochem*. 2017;86:439-460. doi:10.1146/annurev-biochem-061516-045019

16. Greider CW. Telomerase is processive. *Mol Cell Biol*. 1991;11(9):4572-4580. doi:10.1128/mcb.11.9.4572-4580.1991

17. Zhao Y, Abreu E, Kim J, et al. Processive and Distributive Extension of Human Telomeres by Telomerase Under Homeostatic and Non-equilibrium Conditions. *Mol Cell*. 2011;42(3):297-307. doi:10.1016/j.molcel.2011.03.020

18. Blackburn EH, Greider CW, Henderson E, Lee MS, Shampay J, Shippen-Lentz D. Recognition and elongation of telomeres by telomerase. *Genome*. 1989;31(2):553-560. doi:10.1139/g89-104

19. Colgin LM, Baran K, Baumann P, Cech TR, Reddel RR. Human POT1 Facilitates Telomere Elongation by Telomerase. *Curr Biol*. 2003;13(11):942-946. doi:10.1016/S0960-9822(03)00339-7

20. Wang F, Podell ER, Zaug AJ, et al. The POT1-TPP1 telomere complex is a telomerase processivity factor. *Nature*. 2007;445(7127):506-510. doi:10.1038/nature05454

21. Xu M, Kiselar J, Whited TL, Hernandez-Sanchez W, Taylor DJ. POT1-TPP1 differentially regulates telomerase via POT1 His266 and as a function of single-stranded telomere DNA length. *Proc Natl Acad Sci U S A*. 2019;116(47):23527-23533. doi:10.1073/pnas.1905381116

22. Jansson LI, Hentschel J, Parks JW, et al. Telomere DNA G-quadruplex folding within actively extending human telomerase. *Proc Natl Acad Sci*. 2019;116(19):9350-9359. doi:10.1073/pnas.1814777116

23. Bhattacharyya D, Mirihana Arachchilage G, Basu S. Metal Cations in G-Quadruplex Folding and Stability. *Front Chem*. 2016;4:38. doi:10.3389/fchem.2016.00038

24. Zahler AM, Williamson JR, Cech TR, Prescott DM. Inhibition of telomerase by G-quartet DNA structures. *Nature*. 1991;350(6320):718-720. doi:10.1038/350718a0

25. Marcand S. How do telomeres and NHEJ coexist? *Mol Cell Oncol*. 2014;1(3):e963438. doi:10.4161/23723548.2014.963438

26. Bhari VK, Kumar D, Kumar S, Mishra R. Shelterin complex gene: Prognosis and therapeutic vulnerability in cancer. *Biochem Biophys Rep*. 2021;26:100937. doi:10.1016/j.bbrep.2021.100937

27. Gu P, Wang Y, Bisht KK, et al. Human Pot1 OB-fold mutations unleash rampant telomere instability to initiate tumorigenesis. *Oncogene*. 2017;36(14):1939-1951. doi:10.1038/onc.2016.405

28. Pinzaru AM, Hom RA, Beal A, et al. Telomere Replication Stress Induced by POT1 Inactivation Accelerates Tumorigenesis. *Cell Rep*. 2016;15(10):2170-2184. doi:10.1016/j.celrep.2016.05.008

29. WIJAYA A, HIDAYATULLAH F, SETYABUDHI V, PAHLEVI F, INDRA R, NURSETA T. Profile of POT1 as telomerase shelterin component discriminates between cervical cancer and normal cervical cells. *Turk J Med Sci*. 2017;47(2):417-423. doi:10.3906/sag-1512-123

30. Schmidt JC, Zaug AJ, Cech TR. Live Cell Imaging Reveals the Dynamics of Telomerase Recruitment to Telomeres. *Cell*. 2016;166(5):1188-1197.e9. doi:10.1016/j.cell.2016.07.033

31. Schmidt JC, Dalby AB, Cech TR. Identification of human TERT elements necessary for telomerase recruitment to telomeres. Greider C, ed. *eLife*. 2014;3:e03563. doi:10.7554/eLife.03563

32. Tejera AM, Stagno d'Alcontres M, Thanasoula M, et al. TPP1 Is Required for TERT Recruitment, Telomere Elongation during Nuclear Reprogramming, and Normal Skin Development in Mice. *Dev Cell*. 2010;18(5):775-789. doi:10.1016/j.devcel.2010.03.011

33. Nandakumar J, Bell CF, Weidenfeld I, Zaug AJ, Leinwand LA, Cech TR. The TEL patch of telomere protein TPP1 mediates telomerase recruitment and processivity. *Nature*. 2012;492(7428):285-289. doi:10.1038/nature11648

34. Bisht K, Smith EM, Tesmer VM, Nandakumar J. Structural and functional consequences of a disease mutation in the telomere protein TPP1. *Proc Natl Acad Sci*. 2016;113(46):13021-13026. doi:10.1073/pnas.1605685113

35. Graniel JV, Bisht K, Friedman A, et al. Differential impact of a dyskeratosis congenita mutation in TPP1 on mouse hematopoiesis and germline. *Life Sci Alliance*. 2022;5(1):e202101208. doi:10.26508/lsa.202101208

36. Sekne Z, Ghanim GE, van Roon AMM, Nguyen THD. Structural basis of human telomerase recruitment by TPP1-POT1. *Science*. 2022;375(6585):1173-1176. doi:10.1126/science.abn6840

37. Hwang H, Buncher N, Opresko PL, Myong S. POT1-TPP1 regulates telomeric overhang structural dynamics. *Struct Lond Engl*. 2012;20(11):1872-1880. doi:10.1016/j.str.2012.08.018

38. Sanford SL, Welfer GA, Freudenthal BD, Opresko PL. How DNA damage and non-canonical nucleotides alter the telomerase catalytic cycle. *DNA Repair*. 2021;107:103198. doi:10.1016/j.dnarep.2021.103198

39. Sanford SL, Welfer GA, Freudenthal BD, Opresko PL. Mechanisms of telomerase inhibition by oxidized and therapeutic dNTPs. *Nat Commun*. 2020;11:5288. doi:10.1038/s41467-020-19115-y

40. Mender I, Gryaznov S, Dikmen ZG, Wright WE, Shay JW. Induction of Telomere Dysfunction Mediated By the Telomerase Substrate Precursor 6-Thio-2'-Deoxyguanosine. *Cancer Discov*. 2015;5(1):82-95. doi:10.1158/2159-8290.CD-14-0609

41. Yu S, Wei S, Savani M, et al. A Modified Nucleoside 6-thio-2’-deoxyguanosine Exhibits Anti-tumor Activity in Gliomas. *Clin Cancer Res Off J Am Assoc Cancer Res*. 2021;27(24):6800-6814. doi:10.1158/1078-0432.CCR-21-0374

42. Lue NF, Chan J, Wright WE, Hurwitz J. The CDC13-STN1-TEN1 complex stimulates Pol α activity by promoting RNA priming and primase-to-polymerase switch. *Nat Commun*. 2014;5(1):5762. doi:10.1038/ncomms6762

43. Kuchta RD, Reid B, Chang LM. DNA primase. Processivity and the primase to polymerase alpha activity switch. *J Biol Chem*. 1990;265(27):16158-16165. doi:10.1016/S0021-9258(17)46202-8

CHAPTER 2: Real-Time detection of human telomerase DNA synthesis by multiplexed single-molecule FRET

As published in the Biophysical Journal

ABSTRACT

Genomic stability in proliferating cells critically depends on telomere maintenance by telomerase reverse transcriptase. Here we report the development and proof-of-concept results of a single-molecule approach to monitor the catalytic activity of human telomerase in real time and with single-nucleotide resolution. Using zero-mode waveguides and multi-color FRET, we recorded the processive addition of multiple telomeric repeats to individual DNA primers. Unlike existing biophysical and biochemical tools, the novel approach enables the quantification of nucleotide-binding kinetics prior to nucleotide incorporation. Moreover, it provides means to dissect the unique translocation dynamics that telomerase must undergo after synthesis of each hexameric DNA repeat. We observed an unexpectedly prolonged binding dwell time of dGTP in the enzyme active site at the start of each repeat synthesis cycle, suggesting that telomerase translocation is composed of multiple rate-contributing sub-steps that evade classical biochemical analysis.

INTRODUCTION

Telomere homeostasis is critical to tissue development and regeneration. The telomerase enzyme synthesizes the repetitive telomere DNA that, together with telomere-binding proteins, protects linear chromosome ends (1,2). Enzyme dysfunction causes premature aging diseases, while aberrantly upregulated telomerase activity confers replicative immortality to most cancers (3,4). Telomerase is a ribonucleoprotein (RNP) reverse transcriptase (RT) that uses an integral RNA-template to synthesize telomeric DNA-repeats (Fig.1A). In humans, the telomerase RNA (TR) template sequence rC1-rC2-rA3-rA4-rU5-rC6 specifies the hexameric

DNA-repeat sequence dG1-dG2-dT3-dT4-dA5-dG6 (1). The telomerase enzyme (E) is moderately processive and exhibits two modes of processivity (NAP/RAP). Nucleotide-addition processivity (NAP) describes the sequential binding and incorporation of up to six cognate nucleotides (N) into the DNA substrate (D), releasing pyrophosphate (PP_i) upon nucleotide hydrolysis (Fig.1A, and scheme 1).

$$E + D_{\boldsymbol{n}} \rightleftharpoons E \cdot D_{\boldsymbol{n}} + N \rightleftharpoons E \cdot D_{\boldsymbol{n}} \cdot N \longrightarrow E \cdot D_{\boldsymbol{n}"\mathbf{1}} + PP_i \text{ (Scheme 1)}$$

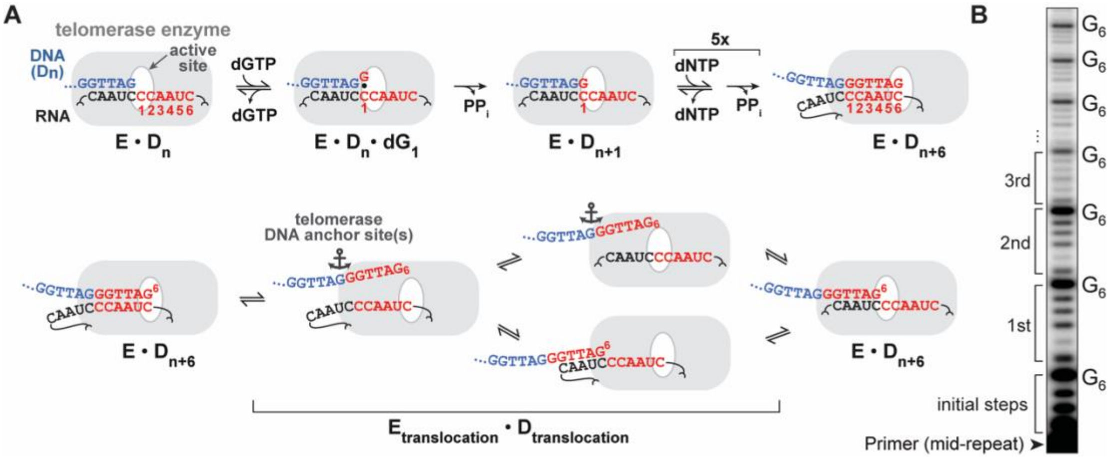

Figure 1. The human telomerase catalytic cycle. A. Schematic of the processive telomerase RNP reverse transcription reaction. Top, nucleotide addition occurs in six steps for a full telomeric DNA repeat. Binding and incorporation of the first dG1 nucleotide is shown in enhanced detail. RNA template positions are numbered in red. Below, processive repeat addition is enabled by DNA/RNA translocation steps that reset the telomerase enzyme. Two possible paths of DNA/RNA repositioning and hybrid formation are shown. **B.** Gel-based analysis of the telomerase reaction extending a radio-labeled DNA primer $(TTAGGG)_3$. Initial steps indicate the completion of the mid-repeat primer. Subsequent full repeats are numbered to the left of the gel.

NAP is associated with single-nucleotide translocation steps of the TR-template in the active site. However, for processive nucleotide addition to continue past the incorporation of dG6, the short integral RNA template must be repositioned to allow for subsequent dG1 binding – a process underlying repeat-addition processivity (RAP). RAP describes the addition of multiple repeats to a single DNA-substrate, and specifically refers to the successful transition from dG6 to dG1 incorporation, initiating a new round of nucleotide addition (Fig.1A, bottom) (5). RAP requires larger-scale translocation steps that include melting of the DNA/RNA duplex, resetting of the RNA template from rC6 to rC1, and formation of a new DNA/RNA hybrid in the telomerase active site. The structural rearrangements required to promote RAP may be described by the dynamic equilibrium (6) depicted in scheme 2.

$$E_{\boldsymbol{rC6}} \cdot D_{\boldsymbol{n"6}} \rightleftharpoons E_{\boldsymbol{translocation}} \cdot D_{\boldsymbol{translocation}} \rightleftharpoons E_{\boldsymbol{rC1}} \cdot D_{\boldsymbol{n"6}} \dashrightarrow NAP \text{ (Scheme 2)}$$

$E\boldsymbol{translocation} \cdot D\boldsymbol{translocation}$ represents the totality of transient intermediate states during RAP-translocation (Fig.1A, bottom). After melting of the RNA/DNA-duplex, RAP relies on a tether between various telomerase ‘anchor-sites’ and the dynamic DNA product, reducing the probability of DNA-dissociation (7,8). The RAP-translocation mechanism remains largely undetermined, and its analysis is challenged by the presence of dynamic and transient states sampled by telomerase and the DNA product.

Current methods to investigate telomerase activity include primer-extension assays that monitor the growing DNA chain (9). Using sequencing gels and radiography, ensemble telomerase reactions can be analyzed at defined end-points and with single-nucleotide resolution (Dn vs Dn+1) (Fig.1B) (10). The moderate degree of telomerase processivity becomes apparent in a characteristic gel-band pattern where each band represents extended DNA-products. Notably, repeat synthesis by telomerase is slow, with an average time span of several minutes per individual repeat under our assay conditions.9 The RAP transitions comprise the slowest steps in the telomerase cycle, providing a proportionally larger time-window for DNA-dissociation to occur (11). The respective DNA-products terminating in dG6 therefore dominate the telomerase product distribution (Fig.1B). The gel-band intensities enable global kinetic modeling of telomerase repeat synthesis (11); however, investigation of mechanistic sub-steps demand biophysical approaches with greater spatiotemporal resolution.

Recently, extensive cryo-EM efforts have provided insight into the architecture of the ciliate and human telomerase RNP, including higher-resolution snapshots of the DNA/RNA hybrid in the active site in the presence of telomerase protein cofactors (12-14). Structural studies of telomerase are challenged by the conformational heterogeneity intrinsic to the enzyme; however, the static structures are invaluable to the design and interpretation of single-molecule approaches that aim to correlate structural heterogeneity with enzyme function. Recent single-molecule assays are able to probe the growing DNA product in real time ($E \cdot D$/ vs $E \cdot D$/"0), but mechanistic and kinetic insights into NAP and RAP cycles were obstructed by DNA structural dynamics (10,15,16). Here we present a FRET-based single-molecule assay that monitors telomerase NAP-steps by means of fluorescence-dye labeled nucleotide analogs. This approach allowed us to demarcate the RAP-translocation steps over multiple consecutive repeat cycles, and simultaneously assess DNA conformational dynamics.

RESULTS

We developed a single-molecule real-time assay that directly visualizes telomerase-nucleotide complexes (E·Dn·N) and permits simultaneous detection of functional structural dynamics during the telomere synthesis reaction. The method overcomes several technical challenges in single-molecule studies, facilitating experiments that (i) increase the concentration of dye-coupled nucleotides to physiologically relevant concentrations, (ii) differentiate enzyme-bound nucleotides from unspecific fluorescence signals, and (iii) enable real-time identification of conformational dynamics that govern enzyme function (Fig.S1). The technique builds on the Pacific Biosciences SMRT-sequencing approach (SMRT: single-molecule real-time, Fig.2A and Fig.S1) (25). However, a key differentiating principle of our approach is the use of Förster Resonance Energy Transfer (FRET) to measure the transfer of energy between dye-conjugated nucleotide analogs and an enzyme-linked fluorescent dye (Fig.2B).

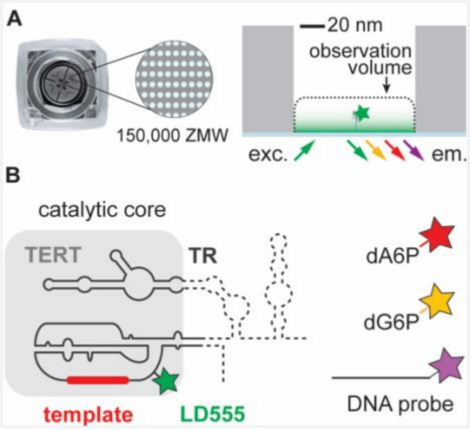

Figure 2. Principal components of the human telomerase ZMW-FRET approach. A. Zero-mode waveguide array chips used for telomerase multicolor ZMW-FRET. **B.** Schematic of human telomerase reverse transcriptase (TERT) and the telomerase RNA (TR, solid and dashed lines). LD555 at the U42 dye-labeling site is highlighted. The catalytic core is formed by TERT and essential domains of TR (solid lines). At right, FRET acceptor components used in this study.

In contrast to the direct excitation of fluorescent components across the visible light spectrum employed in SMRT sequencing, the use of FRET permits experiments to be conducted at higher, near physiological, concentrations of acceptor-dye conjugated nucleotide analogs (Fig.3 and Fig.S1) (26). Of the three telomeric nucleotides (dTTP, dATP, dGTP), we employed dye-coupled dATP and dGTP analogs to serve as FRET acceptor molecules (Fig. S2).

We reasoned that the combination of unmodified dTTP with color-coded dATP/dGTP analogs will produce unambiguous FRET patterns during extension of a telomeric DNA primer by reporting on rU and rC template positions (Fig.3A-B). Also, the FRET patterns could be expected to delineate the start and endpoint of RAP-translocation steps in real time by reporting on the rC$_6$ and rC$_1$ template positions ($\underline{G_1}\underline{G_2}TT\underline{A_5}\underline{G_6}$ – translocation – $\underline{G_1}\underline{G_2}TT\underline{A_5}\underline{G_6}$) (Fig.3B). As in SMRT sequencing, the phosphate-linked dye-moieties are released upon nucleotide incorporation, removing the FRET signal, and yielding a natural DNA product that does not interfere with downstream processes, such as DNA structure formation or anchor-site interactions (25). In a multiplexed FRET approach, concurrent DNA structural dynamics could then be visualized in parallel using a spectrally distinct dye-labeled DNA-probe bound to the nascent telomere DNA (Fig.3A). The $rA_{3/4}$ template positions (dTTP) and RAP translocation steps were expected to present as ‘dark’ states in absence of a FRET acceptor.

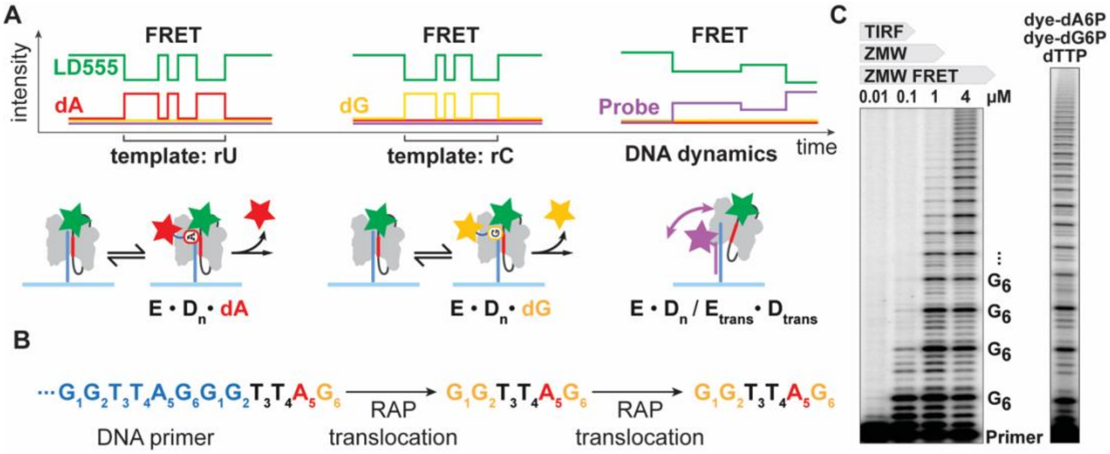

Figure 3. Concept of the telomerase ZMW-FRET approach. A. Principal signals expected from multiplexed ZMW-FRET applied to real-time analysis of telomerase. Dye-coupled hexaphosphate nucleotide analogs dA6P (red) and dG6P (yellow) interact reversibly with telomerase (E). Eventual irreversible nucleotide incorporation into the DNA (D) releases the dye moiety and removes FRET. At right, a Cy5.5-labeled DNA-probe (magenta) can bind to nascent telomere DNA and reports on DNA structural dynamics. Telomerase is immobilized via a telomeric DNA primer (**B**) that is extended repetitively guiding expectations and interpretation of telomerase ZMW-FRET measurements. **C.** Telomerase primer extension assays resolved on sequencing gels after 90 minutes reaction time (see Methods). At left, telomerase requires micro-molar nucleotide concentrations. An approximated range of dye-coupled nucleotide analog concentrations accessible by different single-molecule methods is given above the gel. TIRF, total internal reflection fluorescence. At right, telomerase utilizes dye-dN6P at micro-molar concentrations as used in ZMW-FRET (3.5 µM dye-dG6P, 8 µM dye-dA6P, and 10 µM dTTP).

We employed this FRET-based approach to visualize E·Dn·N complexes directly (i.e. states just prior to nucleotide-incorporation) and in real time. A ‘self-healing’ FRET-donor fluorescence dye (LD555) was coupled to the telomerase RNA (TR) subunit at residue U42 (Fig.2B) (6,27). Structural models suggest that this labeling site was within FRET-range of the nucleotide binding pocket as well as the DNA-product exit path, enabling the multiplexed FRET approach (Fig.3A and Fig.S3A) (13,28). To facilitate site-specific dye-labeling, the catalytic TERT-protein

(‘Telomerase Reverse Transcriptase’) was reconstituted with essential domains of telomerase RNA in-vitro (Fig.2B). This core-complex of the telomerase RNP showed comparable activity to the telomerase holoenzyme isolated from human cells, and a U42-coupled dye-label did not interfere with DNA-repeat synthesis kinetics nor processivity (Fig.S3 and S4) (10,13,28). Hexaphosphate-aminohexyl dATP and dGTP nucleotide analogs (dye-dN6P) were synthesized at PacBio and coupled to fluorescence dyes following established protocols (Fig.S2B) (29). Importantly, telomerase incorporated both types of analogs in ensemble primer-extension assays with comparable activity to unmodified dNTP (Fig.3C).

To detect real-time telomerase activity using FRET, LD555-telomerase was incubated with a biotinylated (TTAGGG)3 DNA-primer, which terminates mid-repeat after the dG2 position and forms stalled enzyme-DNA complexes in the absence of the subsequent nucleotide dTTP (30). Complexes were immobilized on a Neutravidin-coated surface inside individual zero-mode waveguide (ZMW) wells using PacBio array-chips (Fig.2 and Fig.3A-B). The chips were then incubated with imaging mix containing dye-d(A/G)6P, but deficient of dTTP to prevent initiation of telomerase catalysis.

For imaging, chips were mounted on a ZMW-compatible PacBio RSII real-time sequencer (RS). Previous work has demonstrated the utility and customization of the RS instrument for single-molecule fluorescence spectroscopy (Fig.S2A) (20). Three or four-color emission traces from each ZMW were recorded at 10 Hz detector framerate (Fig. S5 and S6). To initiate telomerase primer extension, dTTP was added to the chip by automated pipetting after two minutes of data acquisition. The low background signal afforded by a combination of ZMW-confinement with single green laser-line excitation at 532 nm allowed for dye-dN6P concentrations that support robust telomerase activity (3.5 µM dG6P, 8 µM dA6P, 10 µM dTTP, Fig.3C).

We also performed separate experiments in the presence of Cy5.5-labeled DNA-oligonucleotides that are complementary to 2.5 telomeric repeats, serving to probe DNA synthesis and conformational changes during real-time telomerase activity (Fig.2B and Fig.3A) (10,12). We have previously shown that individual DNA-probes anneal to the nascent telomeric DNA product within FRET-range of a U42-coupled donor dye (10). Importantly, the binding of DNA-probe to the DNA product depended on telomerase activity and extrusion of nascent DNA from telomerase (10).

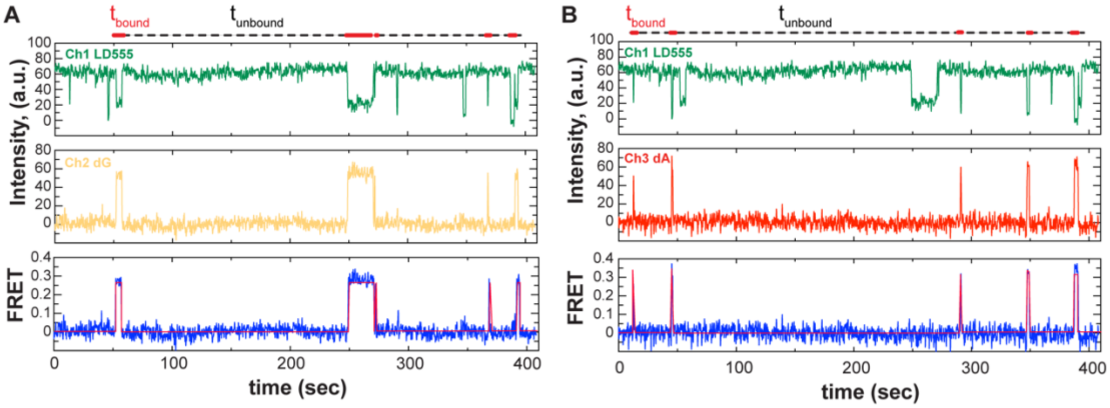

Figure 4. Representative ZMW-FRET traces showing dye-labeled dNTP analog binding events to telomerase. A. A representative donor (LD555, Ch1) dye intensity trace (top panel, green), acceptor dye-labeled dG analog (middle panel, Ch2 yellow), and estimated Ch1-Ch2 FRET trajectory (bottom panel, blue) with idealized smFRET trace fit in vbFRET shown in red (see Methods for details). Times spent in the dG-bound state (t_{bound}) and times spent in the nucleotide-unbound state ($t_{unbound}$) are indicated on the top of the plot. **B.** For the same trajectory show in A, the same donor (LD555, Ch1) dye intensity trace (top panel, green) is shown, along with an acceptor dye-labeled dA analog (middle panel, Ch3 red), and estimated Ch1-Ch3 FRET trajectory (bottom panel, blue) with idealized smFRET trace fit in vbFRET shown in red. Times spent in the dA-bound state (t_{bound}) and times spent in the nucleotide-unbound state ($t_{unbound}$) are indicated on the top of the plot.

We obtained two datasets of 876 and 2009 ZMW-traces (-/+ DNA-probe, respectively) that contained discernible FRET-events between LD555-telomerase and dye-dG6P (E·Dn·dG, yellow) or dye-dA6P (E·Dn·dA, red) (Fig.4 and Fig.S5-S7). In this way, bone fide binding events between telomerase and the dye-conjugated dNTPs can be distinguished from occasional ‘sticking’ events, wherein e.g. a dye-conjugated dG6P transiently interacts with the ZMW surface, accessible to direct and unintended green laser excitation.

Raw data was corrected for drift, channel crosstalk, and acceptor channel dark periods were set to zero to calculate an approximate FRET value for each donor-acceptor pair. We note the FRET values in our experiments are estimates since the true baseline of the donor channel could not accurately be determined for all traces analyzed. Nevertheless, the estimated FRET trajectories for each channel provide a useful signal for generating idealized state assignments using the previously published vbFRET software (21) (Fig. 4). Recent systematic evaluation of several state transition detection algorithms show that each has benefits and pitfalls, with the vbFRET algorithm performing well under standard camera-based smFRET experimental conditions (31,32). When appropriate, automated single molecule FRET analysis programs were employed to extract unbiased values for the lifetime distributions of high (bound) and low (unbound) FRET states. However, in certain contexts (see below) we elected to use an analysis approach that employs manual state assignment to reveal the full information content of the data. For example, currently available procedures (31) cannot take advantage of the information specific to telomerase which enables distinction between dG incorporation pre- and post-translocation events. Furthermore, each repeat cycle has the potential for local modulation (10), so averaging across multiple repeats would lose this important detail.

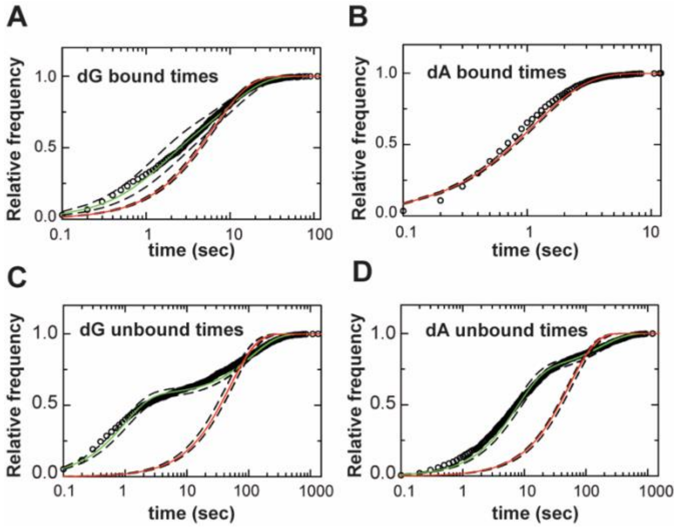

Figure 5. Lifetime histograms for nucleotide analog bound and unbound states. Cumulative lifetime histograms for telomerase in the indicated nucleotide analog bound or unbound states as depicted in Fig. 4 A and B. **A.** Cumulative lifetime histogram of telomerase-dG bound complexes fit with a single (red) or double (green) exponential function (n = 2,198) . **B.** Cumulative lifetime histogram of telomerase-dA bound complexes fit with a single (red) exponential function (n = 1,958). **C.** Cumulative lifetime histogram of telomerase-dG unbound states (time between binding events) fit with a single (red) or double (green) exponential function (n = 1,999). **D.** Cumulative lifetime histogram of telomerase-dA unbound states (time between binding events) fit with a single (red) or double (green) exponential function (n = 1,958). All fits were performed in MEMLET(22) and dashed lines in all plots represent the 95% confidence interval for the fit determined by MEMLET's bootstrapping function. Detailed fit parameters are listed in Supplementary Table S3.

Estimated FRET trajectories derived from 219 analyzed molecules were fitted to a two-state hidden Markov model in vbFRET, and the output used to extract lifetime distributions of the telomerase bound (E·Dn·dN) and unbound (E·Dn) states for dG6P or dA6P (Fig. 4 and 5). Interestingly, whereas the distribution of bound lifetimes for the E·Dn·dA complex was well-fit to a single-exponential function, the distribution of bound lifetimes for the E·Dn·dG complex displayed kinetic heterogeneity that was better fit by a double-exponential function (compare Fig. 5A and 5B). This unexpected result suggested the presence of at least two resolvable kinetically distinct E·Dn·dG complexes observed in our experiments. Similarly, the telomerase unbound lifetime distributions for both the dG6P (Fig. 5C) and dA6P (Fig. 5D) showed substantial kinetic heterogeneity and were better fit by a double-exponential model when compared to a single-exponential fit. Interestingly, this result is consistent with a recent report of kinetic heterogeneity in RNA-DNA and RNA-RNA hybrid duplex formation as measured by smFRET (33). In the context of the telomerase system studied here, our results suggest the nucleotide unbound states measured in our experiments encompass multiple, distinct, kinetic steps during telomerase catalysis, including the translocation steps necessary for repeat addition processivity (Fig. 1).

Having used semi-automated analysis to establish the presence of kinetic heterogeneity in our data, we next employed a manual analysis workflow to correlate the specific sequence of FRET signals with specific stages of telomerase catalysis, an approach that leverages a priori knowledge of the telomeric sequence. Non-cognate sampling events with lifetimes on the micro-second timescale are too short to be resolved in the RS measurement (100 ms per frame) and will contribute to the average background fluorescence (Fig. S8A). However, a feature of our method is the sensitivity to the reversible nature of cognate nucleotide association and dissociation that may occur prior to nucleotide incorporation ($E\cdot Dn+N \rightleftharpoons E\cdot Dn\cdot N$) (Fig. 3A and Fig. S8B). A given template position thereby often manifested as a cluster of FRET signals, rather than a single FRET peak, similar to what was previously described in ZMW-analysis of HIV reverse transcriptase using a SMRT-sequencing related approach (34).

Based upon the known sequence of the TR template, a successful telomerase single-molecule assay was expected to yield an initial ‘dark’ period prior to dTTP delivery and during extension of the (TTAGGG)3 primer by dT3 and dT4 (Fig. 3B and Fig. 6A-B). Completion of the initial repeat by dA5 and dG6 was expected to present as onset of FRET in the red and yellow channels, respectively (Fig. 3B and Fig. 6A-B). These initial patterns were observed in ~90% of all traces. Subsequent FRET-signals were expected to adhere to full telomeric repeat cycles, separated by a ‘dark’ phase that accounted for the telomerase translocation dynamics independent of the presence of nucleotides. In a total of 817 representative traces across both datasets, we identified 1134 repeat patterns that extended beyond the initial dA5/dG6 signals and indicated processive telomerase repeat addition (i.e. RAP). Analysis of each repeated pattern confirmed the presence of distinct phases that we assigned to known sub-steps in the telomerase reaction cycle: (i) a ‘dark’ RAP-translocation phase, (ii) G1/G2-FRET-clusters, (iii) a ‘dark‘ T3/T4-phase, and (iv) a A5/G6-FRET-cluster concluding the repeat (Fig. 6B and Fig. S9A). FRET signals for the G1/G2 pair are treated as a combined cluster in absence of differentiating information.

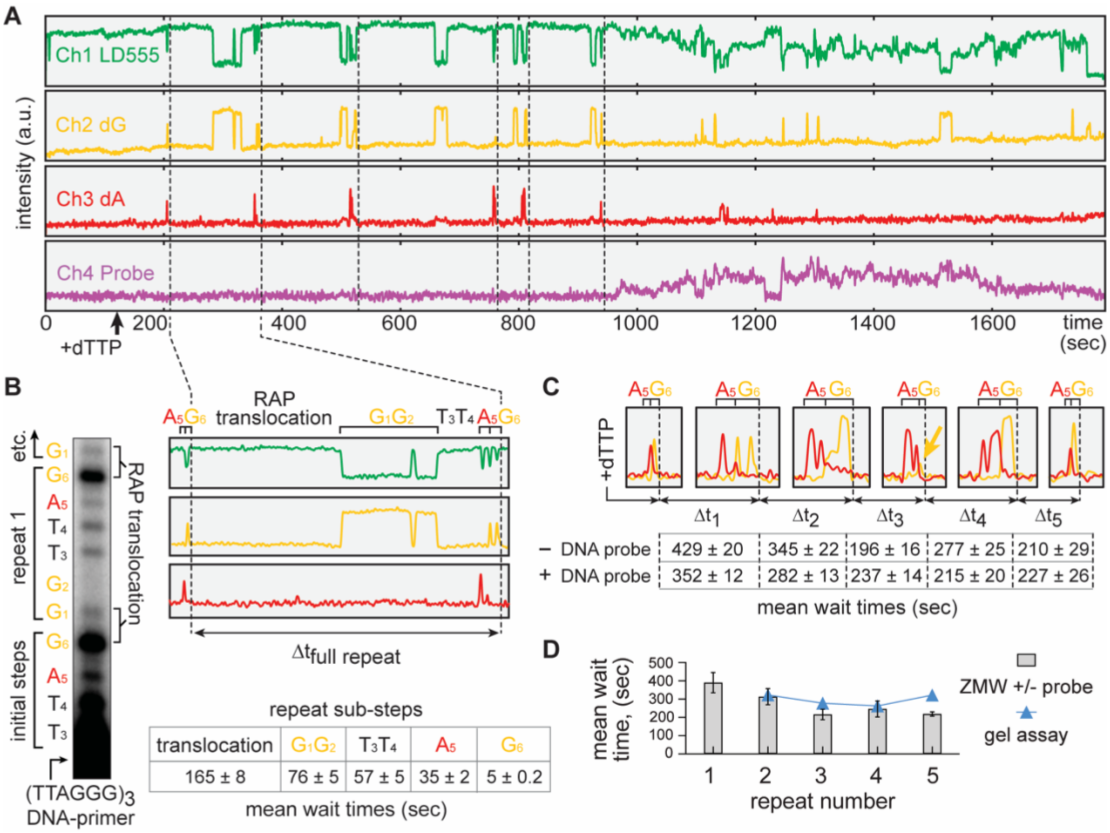

repeat sub-steps

translocation	G1G2	T3T4	A5	G6
165 ± 8	76 ± 5	57 ± 5	35 ± 2	5 ± 0.2

mean wait times (sec)

	Δt1	Δt2	Δt3	Δt4	Δt5
− DNA probe	429 ± 20	345 ± 22	196 ± 16	277 ± 25	210 ± 29
+ DNA probe	352 ± 12	282 ± 13	237 ± 14	215 ± 20	227 ± 26

mean wait times (sec)

Figure 6. Real-time ZMW analysis of human telomerase. A. Four-color trace from a single telomerase molecule. Detection channels are shown separately for clarity. Dashed lines separate discernible repeat patterns. **B.** At left, cropped gel lane visualizes early primer extension and informs expectations for ZMW sequencing. Sequence and numbers indicate telomeric DNA-repeats and the respective template position for each nucleotide. The RAP-translocation steps occur after completion of each respective repeat. At right, example of a repetitive FRET pattern consistent with a telomeric DNA repeat. Repeat sub-steps corresponding to nucleotide positions or the RAP-translocation steps are indicated. The mean duration of each sub-step is given below, $n_{\text{RAP-translocation}}=219$, $n_{G1G2}=373$, $n_{T3T4}=153$, $n_{A5}=577$, $n_{G6}=576$. Errors are standard error of the mean. **C.** A5/G6 motifs enlarged from trace in (A). dG6 incorporations as repeat-end signatures are indicated (dashed lines) and yield repeat wait times for kinetic analysis (Δt), cf. Fig.S9. Below, mean wait times for individual repeats derived from two RS datasets. Errors are standard error of the mean. **D.** Mean wait times for individual repeats derived from ZMW and telomerase gel assay. Error bars indicate the standard deviation across duplicate ZMW experiments. The rate constants are consistent with values derived from gel-based telomerase ensemble assays (blue data points) (10).

To validate the real-time measurement of processive telomere repeat synthesis, we extracted repeat wait times between individual G6-incorporation (Fig. 6C and Fig. S9B). The obtained values from both independent datasets were consistent with previously reported corresponding rate constants derived from kinetic modeling of telomerase ensemble assays (10). Thus, ensemble biochemical and ZMW-based single-molecule telomerase assays yield similar kinetic parameters, further supporting the validity of the ZMW-FRET assay (Fig.6D) (10). Consistent with prior biochemical analysis of ensemble telomerase activity, the ‘dark’ RAP-translocation phase was the slowest sub-step within an individual repeat cycle with a mean duration 165 ± 8 seconds (Fig. 6B). An unexpected feature of our data was that dG6-incorporation occurred relatively soon after dG6 binding (5 ± 0.2 sec), whereas the G1/G2-FRET-clusters exhibited a substantially increased mean duration (76 ± 5 sec, Fig.4B, Fig. S7, and Fig. S9A). The prolonged G1/G2 clusters are unlikely to be explained by the simple combination of two successive dG-incorporation events and may suggest the existence of a long-lived state of the enzyme that results in slow dG incorporation kinetics at the beginning of each telomeric DNA repeat (Fig. S10). This result is consistent with the global analysis of dG binding kinetics that suggested the existence of multiple, kinetically distinct, E·Dn·dG complexes (Fig. 5A). Although the precise structural basis of this observation remains to be elucidated, it is plausible that additional translocation-related events occur after template repositioning and dG1-binding. These may include re-formation of the RNA/DNA hybrid, re-priming of the DNA 3’-end, and active-site closure (Fig. 1A and Fig. S10) (8).

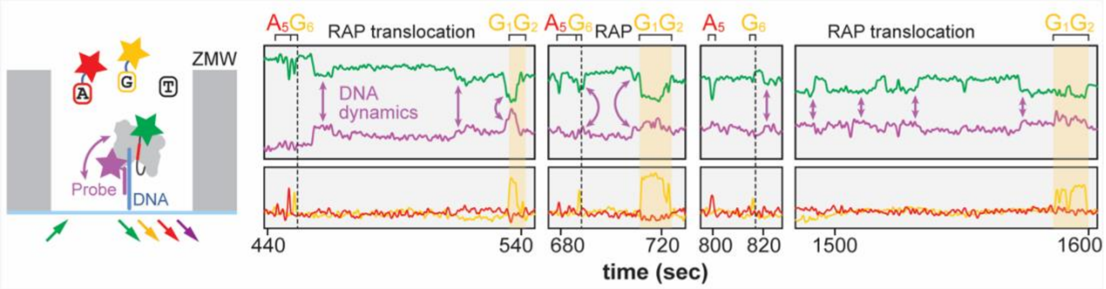

Figure 7. Multiplexed ZMW Telomerase Assay. At left, schematic of the experimental setup inside individual ZMWs. At right, telomerase DNA product dynamics are visualized in real time through binding of an acceptor-labeled DNA probe (top, detection channels 1+4, arrows highlight selected events). The time axis is broken to enlarge regions of interest, cf. Fig.S5. Concurrent nucleotide addition by the same telomerase enzyme (detection channels 2+3) is shown below.

In the presence of Cy5.5-DNA-probe, 605 of 2009 traces displayed FRET between LD555-telomerase and the Cy5.5-labeled probe (magenta) bound to the nascent telomere DNA product (Fig. 6A, Fig. 7, and Fig. S6). This observation represented a direct measurement of product DNA-dynamics resolved concurrently with nucleotide-addition cycles. Interestingly, we identified repeated instances of a Cy5.5-FRET increase during the RAP translocation phase and preceding the onset of G1/G2-clusters. We hypothesize the DNA-product undergoes positional rearrangements during RAP-translocation and thereby becomes accessible for the Cy5.5-DNA probe to bind (Fig.1A and Fig.7). Once bound to the DNA product, the DNA-probes could be expected to report on DNA product movements during subsequent repeat addition cycles and their RAP-translocation steps (Fig.7). For example, while the onset of G1/G2 clusters suggested successful translocation of the RNA template in the active site, future experiments are needed to assign translocation-related Cy5.5-FRET events to DNA-product dynamics before, during, or after formation of the new DNA/RNA duplex (Fig.1A and Fig.7). However, the ability to resolve individual nucleotide-bound enzymes and product DNA-dynamics at specific stages of telomerase repeat synthesis provides a powerful illustration of the information-rich data that can be obtained by combining SMRT-sequencing with single-molecule FRET in the study of telomerase.

DISCUSSION

The ZMW-FRET approach presented here tracks individual telomerase enzymes in real time through multiplexed and quantitative single-molecule analysis. We were thus able to monitor the cyclic nature of telomere repeat synthesis, differentiating the association, incorporation, and dynamics of nucleotides and the DNA substrate. The method enabled the determination of wait-time distributions for the synthesis of individual telomeric repeats as well as for kinetic sub-steps, such as the DNA/RNA translocation pause. Notably, the average repeat synthesis wait times were consistent with gel-based kinetic analysis of telomerase repeat synthesis, supporting the validity of ZMW-FRET in studying the mechanism of telomerase.

Telomerase is a slow enzyme and within the 30-minute measurement window on the PacBio RSII, we rarely observed more than five consecutive repeats, as can be expected for stochastic events with a time constant of around five minutes. While gel-based assays allow for the study of longer DNA products (11), the finite measurement time in ZMW-FRET will bias the distributions of later repeats towards shorter wait times. Previous studies demonstrated that the length of the nascent DNA product influences telomerase activity (10). While longer DNA products can fold into DNA structures that modulate telomerase kinetics, previous studies demonstrated telomerase processivity following the first repeat addition was lower than subsequent repeats (35), possibly because the short DNA primers form weaker interactions with the anchor sites of telomerase. Future ZMW-FRET experiments can employ varying lengths of the starting primer to investigate the influence of short and long DNA products on telomerase function in real time, thereby avoiding a wait time bias that arises after five or more repeats.

In addition to the observation of multiple consecutive repeats, our proof-of-concept data also revealed differential binding and incorporation kinetics of dGTP at the end and beginning of individual telomeric repeats (dG6 versus dG1, respectively). This finding is a specific feature of the ZMW-FRET approach in that it can detect nucleotide-bound states of the enzyme in real time. Due to cognate (and non-cognate) nucleotide sampling of the enzyme active site, the identity of template positions might be encoded in signal clusters rather than single pulses (34). ZMW measurements of fast polymerase systems, that require higher framerates, may visualize a larger contribution of non-cognate nucleotide sampling. The slow reaction speed of telomerase enables lower framerates that reduce the impact of this limitation. Adding to existing models for telomerase translocation mechanisms, we hypothesize that the prolonged G1/G2 clusters present a cognate dGTP-bound state after successful relocation of the TR-template. The unique telomerase RAP-translocation may therefore include rate-contributing rearrangements of the TERT-protein or DNA 3'-end that are uncoupled from TR-template positioning but are required to complete dG1-incorporation. The processivity-stimulating cofactors 'Protection-of-telomeres 1' (POT1) and 'Telomere-Protection-Protein 1' (TPP1) are known to engage the TERT-protein as well as the telomerase DNA product to speed up the telomerase reaction (35,36). The ZMW-FRET approach is uniquely suited to test the hypothesis that POT1-TPP1 will enhance DNA-translocation efficiency thereby reducing the duration of the G1/G2-clusters and increasing telomerase RAP. Our proof-of-concept experiments include a dye-labeled DNA probe that can bind to the nascent DNA product of actively extending telomerase in a manner analogous to POT1-TPP1. More generally, we expect the method described herein will find future application in telomere and telomerase research, enabling direct correlation of structural states observed in static cryo-EM structures with dynamical sub-steps required for telomere length maintenance.

MATERIALS AND METHODS

RNA Preparation

RNA in-vitro transcription. In vitro transcription (IVT) DNA templates for hTR CR4/5 (hTR 239-328), hTR template/pseudoknot (hTR t/PK, 32-195 and 63-195) were generated by PCR fusing the T7 promotor to the respective DNA sequence of hTR (Supplementary Table 1) (10). A total of 400 µl PCR reactions were added directly to the IVT mix. IVTs were carried out using homemade T7 RNA polymerase in 5 ml reactions of 40 mM Tris-HCl, pH 8.0, 35 mM MgCl2, 0.01% (v/v) Triton X-100, 5 mM DTT, 1 mM spermidine, 2.5 mM each NTP and 40 U RNasin Plus (Promega). The reactions were incubated overnight at 37°C followed by the addition of 10 U TURBO DNase (Thermo Fisher Scientific) and incubation for 15 min at 37°C. The RNA was enriched by isopropanol precipitation and purified by denaturing urea polyacrylamide gel electrophoresis (PAGE). The IVT mix of hTR t/PK 63-195 destined for splinted ligation reactions (see below) was modified to contain 1 mM of each NTP and 5 mM GMP to obtain 5′ monophosphate groups.

RNA dye-labeling

To generate dye-labeled telomerase, the synthetic hTR template/pseudoknot (t/PK) fragment 32-62 was purchased from Dharmacon with an internal 5-Aminohexylacrylamino-uridine (5-LC-N-U) at position U42 (Table S1) (17). The RNA was deprotected using provided deprotection buffer (Dharmacon) and following manufacturer’s instructions. Deprotected RNA was desalted using G-25 MidiTrap gravity columns (GE Healthcare), followed by ethanol precipitation in presence of 300 mM sodium acetate, pH 5.2. The pellet was resuspended in 100 µl

0.1 M sodium bicarbonate and brought to a concentration of 200 nmol/ml. For dye- coupling, 20 nmol RNA were combined with an equal volume of anhydrous DMSO containing 100 nmol LD555 (Lumidyne Technologies). The mix was incubated in the dark for 2 h at 37°C, desalted using gravity columns, and dried using a vacufuge (Eppendorf). RNA pellets were dissolved in 60 µl 0.1 M triethylamine acetate (TEAA), pH 7.5, and dye-labeled RNA was purified by HPLC in a 0.1 M TEAA to 60% acetonitrile gradient on a reversed phase C8 column (Agilent Technologies).

RNA ligation

Synthetic and dye-labeled hTR 32-62 was ligated to in vitro transcribed hTR t/PK 63-195 by splinted RNA ligation(17). A 200 µl reaction contained 800 pmol of LD555-hTR 32-62, 1600 pmol hTR 63-195, and 1600 pmol DNA splint (Supplementary Table 1) in 0.5x T4 DNA ligase buffer (NEB). The mix was incubated for 5 min at 95°C and for further 10 min at 30°C. 200 µl ligation mix (1.5x T4 DNA ligase buffer, 8000 U T4 DNA ligase (NEB), 2 mM ATP and 200 U RNasin Plus) was added to the reaction and incubated overnight at 30°C. 10 U TURBO DNase were added and incubated for 15 min at 37°C. The RNA was then phenol-chloroform extracted, ethanol precipitated, and purified by urea PAGE.

Telomerase Reconstitution

Human telomerase was reconstituted in rabbit reticulocyte lysate (RRL, Promega TnT Quick Coupled Transcription/Translation kit) following the manufacturers specifications(18) . Specific to telomerase, 200 µl TnT mix were supplemented with 5 µg of the plasmid pNFLAG-hTERT (19) and 1 µM of in vitro transcribed (see above) and unlabeled hTR fragments (hTR template/pseudoknot and CR4/5). In reconstitutions of dye-labeled telomerase, the LD555 t/PK fragment (see above) was added at 0.1 µM final concentration owing to lower relative yields after RNA ligation and dye labeling. The reaction mix was incubated for 3 h at 30°C and quenched with 5 µl of 0.5 M EDTA, pH 8.0 for 30 min at room temperature. For immuno-purification of telomerase, beads from 50 ul ANTI-FLAG M2-agarose bead slurry (Sigma-Aldrich) were washed three times by suspension in 750 µl wash buffer (50 mM Tris-HCl, pH 8.3, 3 mM MgCl2, 2 mM DTT, 100 mM NaCl), centrifugation for 30 seconds at 2350 rcf, and removal of the supernatant. Beads were subsequently blocked twice for 15 min in blocking buffer (50 mM Tris-HCl, pH 8.3, 3 mM MgCl2, 2 mM DTT, 500 µg/ml BSA, 50 µg/ml glycogen, 100 µg/ml yeast tRNA) under end-over- end agitation at 4°C. Blocked beads were collected by centrifugation, resuspended in 200 µl blocking buffer and added to the telomerase reconstitution reaction in RRL. This binding step was left to proceed for 2 h at 4°C under end-over-end agitation. The beads were then pelleted and washed three times in wash buffer containing 300 mM NaCl, followed by three further wash steps in wash buffer containing 100 mM NaCl. Elution of telomerase from the beads was performed by adding 60 µl elution buffer (50 mM Tris-HCl, pH 8.3, 3 mM MgCl2, 2 mM DTT, 750 µg/ml 3xFLAG peptide, 20% glycerol) to the beads and incubation for 1h at 4°C under orbital agitation. The mix was then transferred to a Nanosep MF 0.45 µM centrifugal filter and eluate was collected by centrifugation at 10,000 rcf for 1 min. 5 µl aliquots (3 µl in case of dye-labeled telomerase) were prepared in Lo-bind tubes (Eppendorf), flash frozen in liquid nitrogen and stored at -80°C until use.

32P-end-labeling of DNA primers

50 pmol of DNA primer was labeled with gamma- 32P ATP and T4 polynucleotide kinase (NEB) in a 50 ul reaction in 1x PNK buffer (NEB). The mix was incubated for 1 h at 37°C followed by heat inactivation of T4 PNK at 65°C for 20 min. The primers were purified on Centrispin columns (Princeton Separations) and brought to a final concentration of 50 nM in nuclease-free water.

Primer extension assays

Bulk activity assays were performed using 5 µl immuno- purified telomerase brought to 15 µl reaction volume of 50 mM Tris-HCl, pH 8.3, 50 mM KCl, 3 mM MgCl2, 2 mM DTT(6). 32P-end-labeled DNA primers were used at 50 nM and nucleotide concentrations were as indicated (ranging from 0.1 µM to 10 µM of each dATP, dTTP and dGTP). Dye-dG6P and dye-dA6P were used at 3.5 µM and 8 µM, respectively, to be consistent with RS assay conditions. dTTP was used at 10 μM when mixed with dye-dG6P and dye-dA6P. Reactions were incubated for 90 min at 30°C and quenched with 200 μl TES (10 mM Tris-HCl, pH 7.5, 1 mM EDTA, 0.1% SDS). For kinetic analysis, reactions were chased after 10 min incubation with 20 μM unlabeled primer and samples quenched at 10 min intervals. DNA products were phenol-chloroform extracted and ethanol precipitated. DNA pellets were resuspended in formamide gel loading buffer (50 mM Tris Base, 50 mM boric acid, 2 mM EDTA, 80% (v/v) formamide, 0.05% (w/v) each bromophenol blue and xylene cyanol) and resolved on a 12% denaturing urea PAGE gel. The gel was then dried and imaged using a storage phosphor screen and Typhoon scanner (GE Healthcare).

RS assay

Chip preparation and enzyme immobilization. RS chips (SMRT cell, PacBio) were washed three times each with 40 μl TP50 buffer (50 mM Tris-HCl, pH 8.0, 50 mM KCl). 20 μl Neutravidin was supplied to the chip and incubated for 5 min at room temperature. Neutravidin was removed, followed by three wash steps each with 40 μl telomerase buffer (50 mM Tris-HCl, pH 8.3, 50 mM KCl, 3 mM MgCl2). 5 nM stocks of biotin-(TTAGGG)3-primer in TLi (50 mM Tris-HCl, pH 8.3, 50 mM LiCl) were heated to 95°C for 3 min to melt primer aggregates or G-rich structures. Primers were cooled on ice. 3 μl immuno-purified LD555-telomerase was combined with 1 μl of 5 nM heat-treated primer and incubated for 20 min at 30°C. 16 ul of telomerase buffer was added to this mix at room temperature. The resulting 20 μl enzyme mix was supplied to an RS chip, sealed with parafilm, and incubated for 15 min at 30°C. The enzyme mix was removed, and the chip washed three times each with telomerase buffer.

RS setup and chip imaging

The RSII real-time DNA sequencer (RS, PacBio) was initialized from the user interface (20). The green laser (532 nm) was set to a laser power of 0.24 μW/μm2. A calibration measurement was previously conducted at the same laser power as a reference according to the manufacturer's instructions. The movie length was 30 minutes at a frame rate of 10 Hz. The chip clamp temperature (~ZMW temperature) was 30°C. A dispense protocol was selected for fluidic delivery of 20 µl delivery solution (see below) to the chip at 140 seconds into the movie. After initialization, enzyme-treated chips were supplied with telomerase imaging buffer (50 mM Tris-HCl, pH 8.3, 50 mM KCl, 3 mM MgCl2, 2.5% (v/v) N-Formylmorpholine, 3.5 µM dye-dG6P, 8 µM dye-dATP, oxygen-scavenging system [2.5 mM PCA (protocatechuic acid), 2.5 mM TSY, and 2x PCD (protocatechuate-3,4-dioxygenase), purchased from Pacific Bioscience]) and the silica surface of the chip was cleaned with methanol. Chips were then mounted in the SMRT-cell chamber of the RS. Telomerase imaging "delivery" solution (imaging buffer including 20 µM dTTP, and 40 nM DNA probe where indicated) was provided in a 96well sample plate in the sample chamber of the RS and kept at 4°C until delivery. Data acquisition was started from the RS user interface (20).

Data analysis

Fluorescence trace extraction and data analysis were performed with a set of custom-written Matlab scripts (available upon request). Procedures adhered to the principal workflow described below. The RS generates approximately 150,000 four-color traces per ZMW experiment. To down-select data for ZMWs that, in principle, possessed active telomerase complexes, the raw data traces were computationally screened for fluorescence intensity anti-correlation between detection channels 1 (green) and 3 (red), indicating energy transfer between the respective fluorophores. The down-selected trace subset was then manually screened for photophysical artifacts or noise. The manually curated trace subset was used for two different analysis workflows as described below.

Semi-automated processing and idealized trace generation

Individual data traces were pre-processed for FRET state assignment using the previously published vbFRET software suite (21). Trace pre-processing was performed according to the following workflow: (i) crop the region of interest to remove photobleaching events or initial noise in the trace due to buffer exchange; (ii) donor channel (Ch1) drift correction; (iii) channel crosstalk correction; (iv) baseline correction of acceptor channels (Ch2, Ch3, and/or Ch4); (v) calculation of effective FRET values for each channel and fine adjust of channel crosstalk correction due to optical variation between ZWMs, (vi) visual removal of any artifactual (non-anticorrelated) signals from traces; (vii) dynamic calculation of FRET threshold values to set unbound state to zero prior to automated state assignment; and (viii) file export for each trace in vbFRET compatible format. Idealized traces were subsequently generated using the HMM module of vbFRET to fit a simple two-state model to each FRET trace. The output of vbFRET was then used to automatically extract on-time and off-time distributions for dG (Ch2) and dA (Ch3) binding events which were fit using the MEMLET analysis software (22). Detailed fit parameters are listed in Supplementary Table S3. Figures were subsequently prepared using Graphpad Prism.

Manual assignment and kinetic analysis of telomerase phases in individual traces
Individual traces were viewed using a custom and interactive Matlab script (Fig. S11, all scripts are available upon request). The assignment script allows the user to highlight any suspected telomerase sub-step in a point-and-click approach: Basically, the start (e.g. G6 intensity upward transition) and end (e.g. G6 intensity downward transition) of signal clusters were selected by mouse-click, generating an idealized (noise-free) trace that displays all state transitions that were selected manually in the raw data window (Fig.S11, raw data window vs idealized trace window). The script permitted state assignment in different colors and with different amplitudes to aid visual distinction of the states (Fig.S11, red states are A5, yellow states are G6, gray states are RAP and G1/G2 phases). The purpose of the idealized state trace was to demarcate the time-points of state transitions for kinetic analysis. The time-points of state transitions were extracted in Matlab and allowed calculation of both wait times in-between signal clusters, as well as life-times of signal clusters. Time-distributions were fit with exponential functions in

Matlab MEMLET (22) and plotted in Graphpad Prism. Rate constants for single irreversible kinetic steps were calculated as the inverse of the mean of the life-time population. Reported estimates of the standard error of the mean for each measured wait time were determined using the bootstrapping function within Matlab MEMLET(22-24). While manual state-assignment for kinetic analysis was performed using raw data traces (Fig.S11), we corrected traces for bleed-through and background for clarity in the figures (Fig.S8A).

REFERENCES

1. Blackburn, E. H., and K. Collins. 2011. Telomerase: an RNP enzyme synthesizes DNA. *Cold Spring Harb Perspect Biol*. 3(5), doi: 10.1101/cshperspect.a003558

2. de Lange, T. 2005. Shelterin: the protein complex that shapes and safeguards human telomeres. *Genes Dev*. 19(18):2100-2110, doi: 10.1101/gad.1346005,

3. Aubert, G., and P. M. Lansdorp. 2008. Telomeres and aging. *Physiol Rev*. 88(2):557-579, doi: 10.1152/physrev.00026.2007,

4. Shay, J. W., and S. Bacchetti. 1997. A survey of telomerase activity in human cancer. *Eur J Cancer*. 33(5):787-791, doi: 10.1016/S0959-8049(97)00062-2,

5. Greider, C. W. 1991. Telomerase is processive. *Mol Cell Biol*. 11(9):4572-4580, doi: 10.1128/mcb.11.9.4572,

6. Parks, J. W., and M. D. Stone. 2014. Coordinated DNA dynamics during the human telomerase catalytic cycle. *Nat Commun*. 5:4146, doi: 10.1038/ncomms5146,

7. Lue, N. F. 2005. A physical and functional constituent of telomerase anchor site. *J Biol Chem*. 280(28):26586-26591, doi: 10.1074/jbc.M503028200,

8. Wu, R. A., H. E. Upton, J. M. Vogan, and K. Collins. 2017. Telomerase Mechanism of Telomere Synthesis. *Annu Rev Biochem*. 86:439-460, doi: 10.1146

9. Greider, C. W., and E. H. Blackburn. 1985. Identification of a specific telomere terminal transferase activity in Tetrahymena extracts. *Cell*. 43(2 Pt 1):405-413

10. Jansson, L. I., et al., 2019. Telomere DNA G-quadruplex folding within actively extending human telomerase. *Proc Natl Acad Sci U S A*. 116(19):9350-9359

11. Bagshaw, C. R., J. Hentschel, and M. D. Stone. 2021. The Processivity of Telomerase: Insights from Kinetic Simulations and Analyses. *Molecules*. 26(24)

12. Jiang, J., Y. Wang, L. Susac, H. Chan, R. Basu, Z. H. Zhou, and J. Feigon. 2018. Structure of Telomerase with Telomeric DNA. *Cell*. 173(5):1179-1190 e1113

13. Ghanim, G. E., A. J. Fountain, A. M. van Roon, R. Rangan, R. Das, K. Collins, and T. H. D. Nguyen. 2021. Structure of human telomerase holoenzyme with bound telomeric DNA. *Nature*. doi: 10.1038/s41586-021-03415-4,

14. Sekne, Z., G. E. Ghanim, A. M. van Roon, and T. H. D. Nguyen. 2022. Structural basis of human telomerase recruitment by TPP1-POT1. *Science*. 375(6585):1173-1176

15. Hwang, H., P. Opresko, and S. Myong. 2014. Single-molecule real-time detection of telomerase extension activity. *Sci Rep*. 4:6391, doi: 10.1038/srep06391,

16. Patrick, E. M., J. D. Slivka, B. Payne, M. J. Comstock, and J. C. Schmidt. 2020. Observation of processive telomerase catalysis using high-resolution optical tweezers. *Nat Chem Biol*. 16(7):801-809, doi: 10.1038/s41589-020-0478-0,

17. Akiyama, B. M., and M. D. Stone. 2009. Assembly of complex RNAs by splinted ligation. *Methods Enzymol*. 469:27-46, doi: 10.1016/S0076-6879(09)69002-9,

18. Weinrich, S. L., R. et al. 1997. Reconstitution of human telomerase with the template RNA component hTR and the catalytic protein subunit hTRT. *Nat Genet*. 17(4):498-502, doi: 10.1038/ng1297-498

19. Drosopoulos, W. C., R. Direnzo, and V. R. Prasad. 2005. Human telomerase RNA template sequence is a determinant of telomere repeat extension rate. *J Biol Chem*. 280(38):32801-32810, doi: 10.1074/jbc.M506319200,

20. Chen, J., R. V. Dalal, A. N. Petrov, A. Tsai, S. E. O'Leary, K. Chapin, J. Cheng, M. Ewan, P. L. Hsiung, P. Lundquist, S. W. Turner, D. R. Hsu, and J. D. Puglisi. 2014. High-throughput platform for real-time monitoring of biological processes by multicolor single-molecule fluorescence. *Proc Natl Acad Sci U S A*. 111(2):664-669

21. Bronson, J. E., J. Fei, J. M. Hofman, R. L. Gonzalez, Jr., and C. H. Wiggins. 2009. Learning rates and states from biophysical time series: a Bayesian approach to model selection and single-molecule FRET data. *Biophys J*. 97(12):3196-3205

22. Woody, M. S., J. H. Lewis, M. J. Greenberg, Y. E. Goldman, and E. M. Ostap. 2016. MEMLET: An Easy-to-Use Tool for Data Fitting and Model Comparison Using Maximum-Likelihood Estimation. *Biophys J*. 111(2):273-282

23. Efron, B. a. T., R. 1982. The jackknife, the bootstrap and other resampling plans. Society for Industrial and Applied Mathematics.

24. Numerical Recipes in C++: The Art of Scientific Computing. 2002. W.H. Press, Cambridge University Press, Cambridge, United Kingdom.

25. Eid et al. 2009. Real-time DNA sequencing from single polymerase molecules. *Science*. 323(5910):133-138, doi: 10.1126/science.1162986,

26. Goldschen-Ohm, M. P., D. S. White, V. A. Klenchin, B. Chanda, and R. H. Goldsmith. 2017. Observing Single-Molecule Dynamics at Millimolar Concentrations. *Angew Chem Int Ed Engl*. 56(9):2399-2402, doi: 10.1002/anie.201612050

27. Zheng, Q., S. Jockusch, Z. Zhou, R. B. Altman, H. Zhao, W. Asher, M. Holsey, S. Mathiasen, P. Geggier, J. A. Javitch, and S. C. Blanchard. 2017. Electronic tuning of self-healing fluorophores for live-cell and single-molecule imaging. *Chem Sci*. 8(1):755-762, doi: 10.1039/C6SC02976K,

28. Nguyen, T. H. D., J. Tam, R. A. Wu, B. J. Greber, D. Toso, E. Nogales, and K. Collins. 2018. Cryo-EM structure of substrate-bound human telomerase holoenzyme. *Nature*. 557(7704):190-195, doi: 10.1038/s41586-018-0062-x,

29. Korlach, J., A. Bibillo, J. Wegener, P. Peluso, T. T. Pham, I. Park, S. Clark, G. A. Otto, and S. W. Turner. 2008. Long, processive enzymatic DNA synthesis using 100% dye-labeled terminal phosphate-linked nucleotides. *Nucleosides Nucleotides Nucleic Acids*. 27(9):1072-1083, doi: 10.1080/15257770802260741,

30. Wallweber, G., S. Gryaznov, K. Pongracz, and R. Pruzan. 2003. Interaction of human telomerase with its primer substrate. *Biochemistry*. 42(2):589-600, doi: 10.1021/bi026914a

31. Gotz, M. et al. 2022. A blind benchmark of analysis tools to infer kinetic rate constants from single-molecule FRET trajectories. *Nat Commun*. 13(1):5402, doi: 10.1038/s41467-022-33023-3

32. Hadzic, M., R. Borner, S. L. B. Konig, D. Kowerko, and R. K. O. Sigel. 2018. Reliable State Identification and State Transition Detection in Fluorescence Intensity-Based Single-Molecule Forster Resonance Energy-Transfer Data. *J Phys Chem B*. 122(23):6134-6147, doi: 10.1021/acs.jpcb.7b12483

33. Steffen, F. D., M. Khier, D. Kowerko, R. A. Cunha, R. Borner, and R. K. O. Sigel. 2020. Metal ions and sugar puckering balance single-molecule kinetic heterogeneity in RNA and DNA tertiary contacts. *Nat Commun*. 11(1):104

34. Vilfan, I. D., Y. C. Tsai, T. A. Clark, J. Wegener, Q. Dai, C. Yi, T. Pan, S. W. Turner, and J. Korlach. 2013. Analysis of RNA base modification and structural rearrangement by single-molecule real-time detection of reverse transcription. *J Nanobiotechnology*. 11:8, doi: 10.1186/1477-3155-11-8,

35. Latrick, C. M., and T. R. Cech. 2010. POT1-TPP1 enhances telomerase processivity by slowing primer dissociation and aiding translocation. *EMBO J*. 29(5):924-933, doi: 10.1038/emboj.2009.409

36. Wang, F., E. R. Podell, A. J. Zaug, Y. Yang, P. Baciu, T. R. Cech, and M. Lei. 2007. The POT1-TPP1 telomere complex is a telomerase processivity factor. *Nature*. 445(7127):506-510, doi: 10.1038/nature05454,

SUPPLEMENTARY INFORMATION

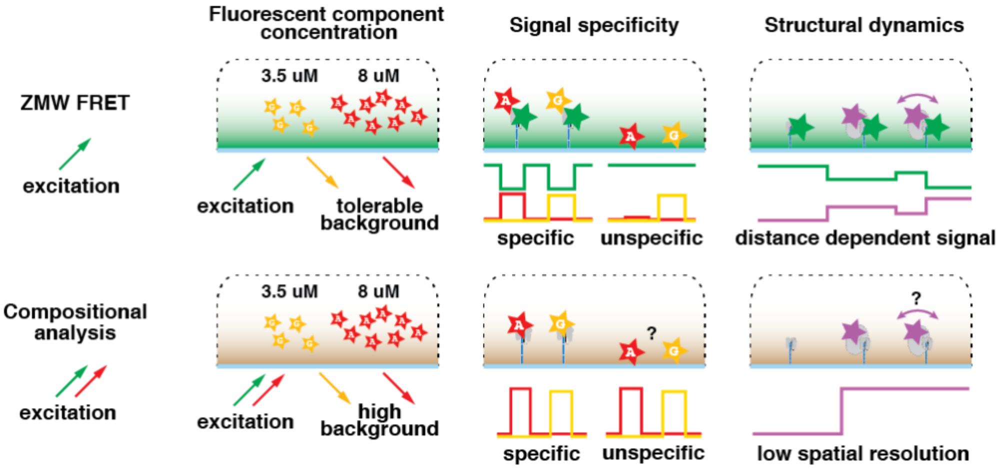

Figure S1. Specific advantages of ZMW-FRET over SMRT-sequencing when applied to mechanistic studies of telomerase reverse transcription or other biological systems.

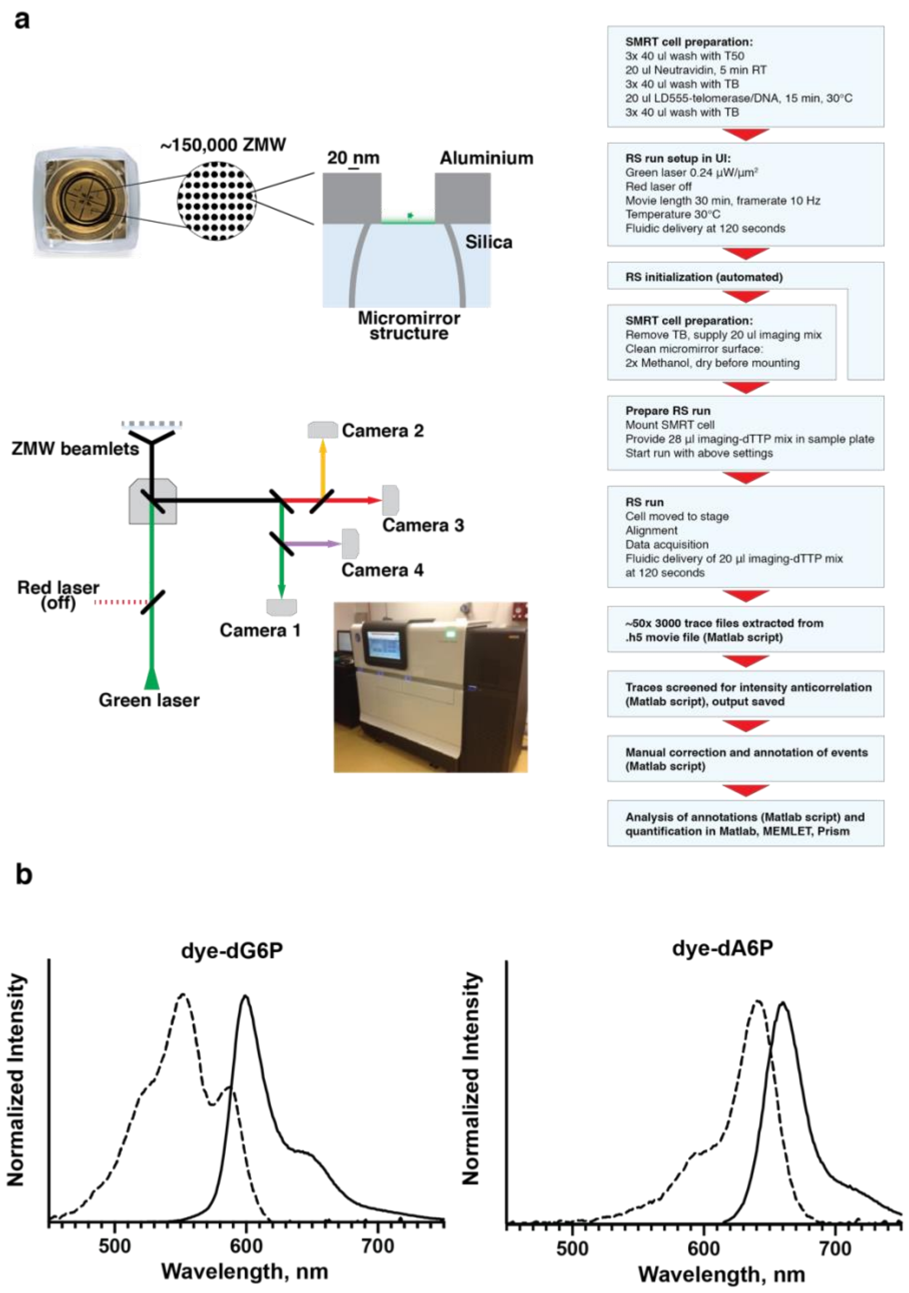

SMRT cell preparation:
3x 40 ul wash with T50
20 ul Neutravidin, 5 min RT
3x 40 ul wash with TB
20 ul LD555-telomerase/DNA, 15 min, 30°C
3x 40 ul wash with TB

RS run setup in UI:
Green laser 0.24 µW/µm^2
Red laser off
Movie length 30 min, framerate 10 Hz
Temperature 30°C
Fluidic delivery at 120 seconds

RS initialization (automated)

SMRT cell preparation:
Remove TB, supply 20 ul imaging mix
Clean micromirror surface:
2x Methanol, dry before mounting

Prepare RS run
Mount SMRT cell
Provide 28 µl imaging-dTTP mix in sample plate
Start run with above settings

RS run
Cell moved to stage
Alignment
Data acquisition
Fluidic delivery of 20 µl imaging-dTTP mix
at 120 seconds

~50x 3000 trace files extracted from .h5 movie file (Matlab script)

Traces screened for intensity anticorrelation (Matlab script), output saved

Manual correction and annotation of events (Matlab script)

Analysis of annotations (Matlab script) and quantification in Matlab, MEMLET, Prism

Figure S2. A. Experimental setup of ZMW chips and the PacBio RS II instrument used for telomerase ZMW-FRET real-time analysis. **B.** Excitation (dashed lines) and emission spectra of dye-dG6P and dye-dA6P.

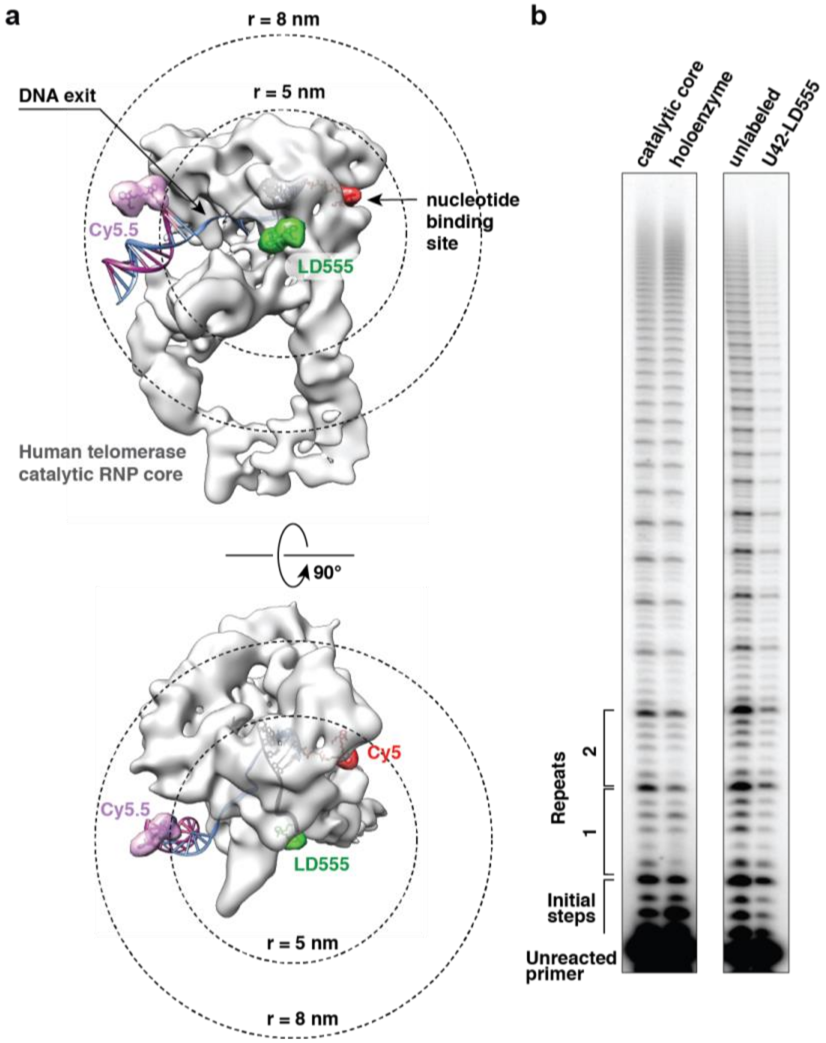

Figure S3. Human telomerase catalytic core. a. The cryo EM structure (EMDB 7518) approximates the minimal telomerase complex used in this study. Telomeric DNA (33 nt) is in blue, telomerase RNA template region in black. The nucleotide binding pocket is occupied with a coordinate model of dA6P-aminohexyl coupled to Cy5 (red). The U42 labeling site and approximate position of LD555 are indicated with a simulated density map of a standard Cy3 fluorescence dye moiety (green). A Cy5.5-DNA probe is annealed to nascent telomere DNA in a possible orientation outside the DNA exit cavity of telomerase. FRET radii around LD555 are indicated by dashed circles. Bottom, top view. **b.** Left, primer extension assays of the *in-vitro* reconstituted telomerase catalytic core compared to telomerase holoenzyme isolated from HEK293T cells. Right, primer extension assay of unlabeled telomerase catalytic core and LD555-telomerase catalytic core. Note that dye-labeled enzyme is reconstituted with limiting amounts of LD555-hTR fragments leading to lower enzyme yields and product band intensities.

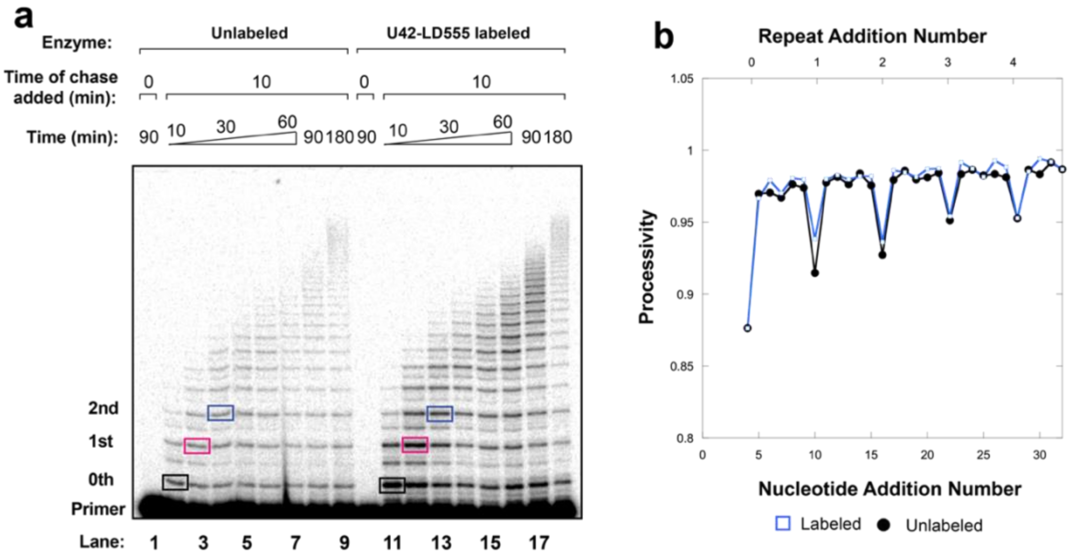

Figure S4. Activity of U42 TR labeled telomerase. a. Primer extension assay performed with 50 nM 32P-labeled DNA primer and 10 mM each of dGTP, dATP and dTTP. After 10 min incubation, 20 mM unlabeled DNA primer was added and the chase reaction followed by quenching samples at intervals during a further 170 minute incubation. Quantitative analysis of the band intensities determined using SAFA (1) showed that the progression of the modal repeat bands (boxed) followed a similar time course (see Supplementary Table S2 below). The higher intensity of the bands in the U42 TR-labeled telomerase indicated that the concentration of active enzyme was three times that of the unlabeled telomerase preparation, but their specific activities were similar. **b.** Analysis of the processivity of the U42 TR-labeled and unlabeled telomerase using the method of Peng et al (2) applied to the 180 min lanes (i.e. 10 min incubation + 170 min post-chase). The plots for the 90 min lanes were similar indicating the repeats 0 to 4 had reached their near end-point levels. Individual band intensities up to the 6th repeat were estimated using SAFA, while the further extended products, which were progressively less well resolved, were determined from the integrated area using the ImageJ Gel Analyze plug-in (https://imagej.nih.gov/nih-image/manual/tech.html). This allowed a correction factor to be applied to the processivity calculation to overcome the truncation problem when only a limited number of bands are resolved (3).

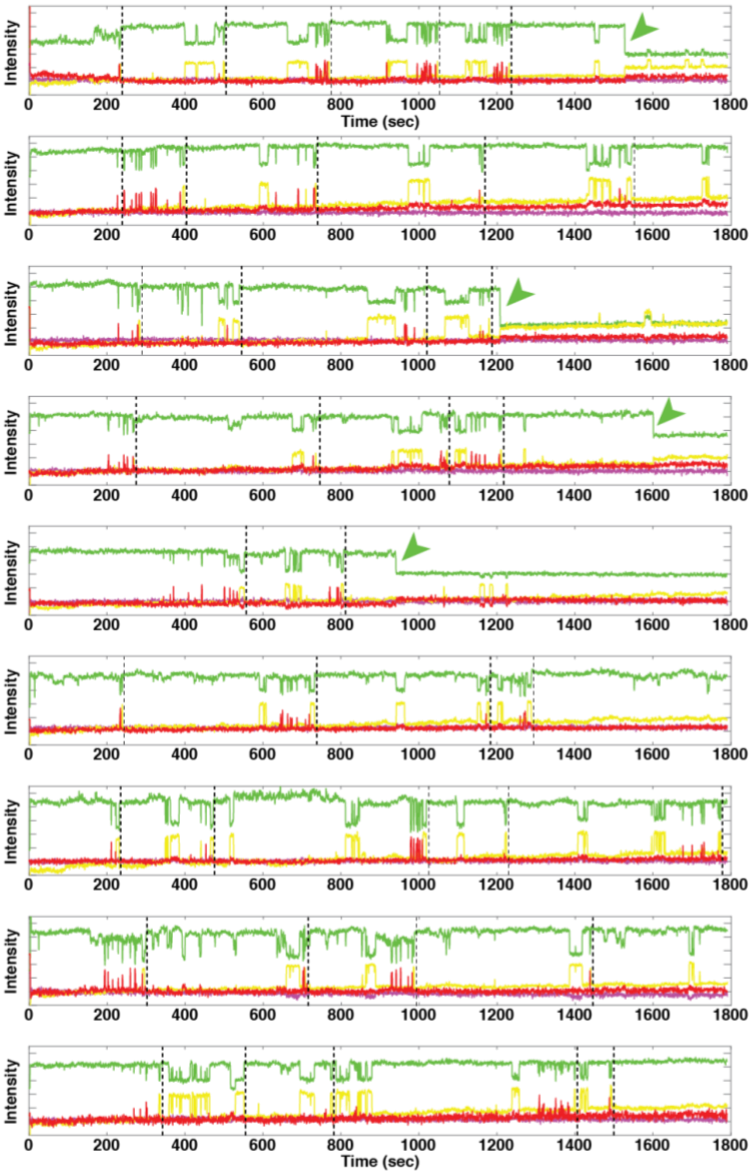

Figure S5. Example traces visualizing real-time telomerase activity by ZMW-FRET in absence of DNA-probe oligonucleotide. Dashed lines indicate dG6 incorporation events preceding a RAP phase, cf. Fig.4A-C. Loss of LD555 donor fluorescence (green arrows) represents DNA dissociation from telomerase or dye photo-bleaching. An offset is applied to the baseline of LD555 for clarity.

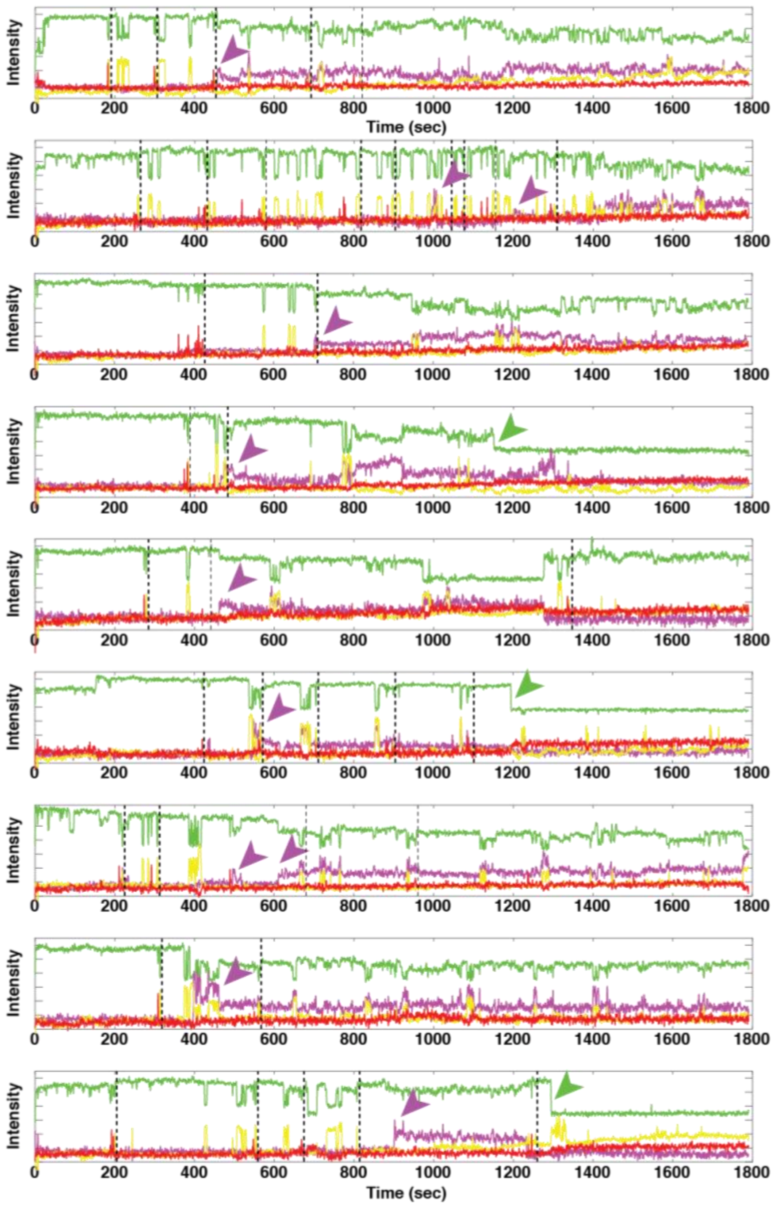

Figure S6. Example traces visualizing real-time telomerase activity by ZMW-FRET in presence of DNA-probe oligonucleotide (magenta). Dashed lines indicate dG6 incorporation events preceding a RAP phase, cf. Fig.4. Loss of LD555 donor fluorescence (green arrows) represents DNA dissociation from telomerase or dye photo-bleaching. An offset is applied to the baseline of LD555 for clarity. The association and onset of DNA-dynamics is indicated by arrowheads in magenta.

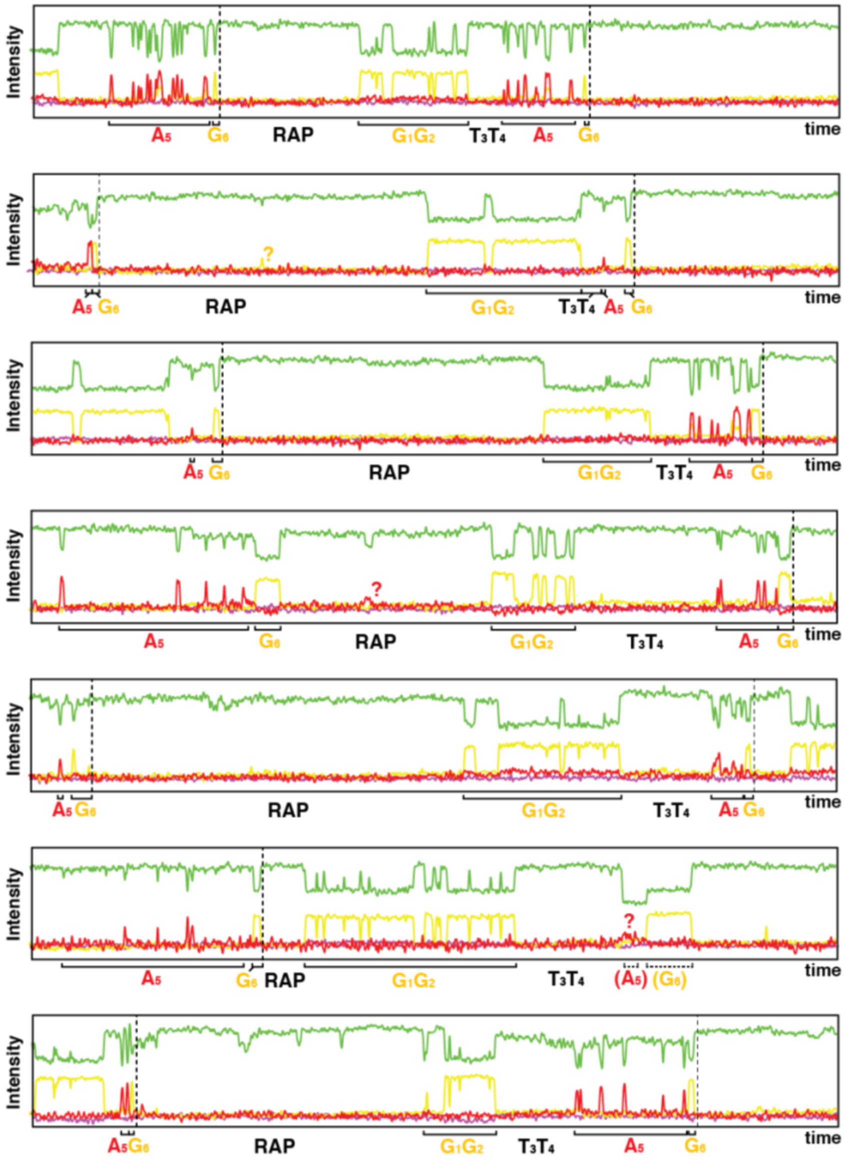

Figure S7. Example traces to highlight the repetitive FRET pattern that corresponds to individual telomeric repeats, cf. Fig.4B. The probabilistic nature of signal clusters is most prominent for A5 (red) and G1/G2 signals at template positions rU5 and rC1/rC2, respectively. The lifetimes of G1/G2 clusters exceed expectations for the homo-dimer G1/G2 and may indicate specific RAP steps to be completed after G1-binding, but prior to G1-incorporation, cf. Fig.S10.

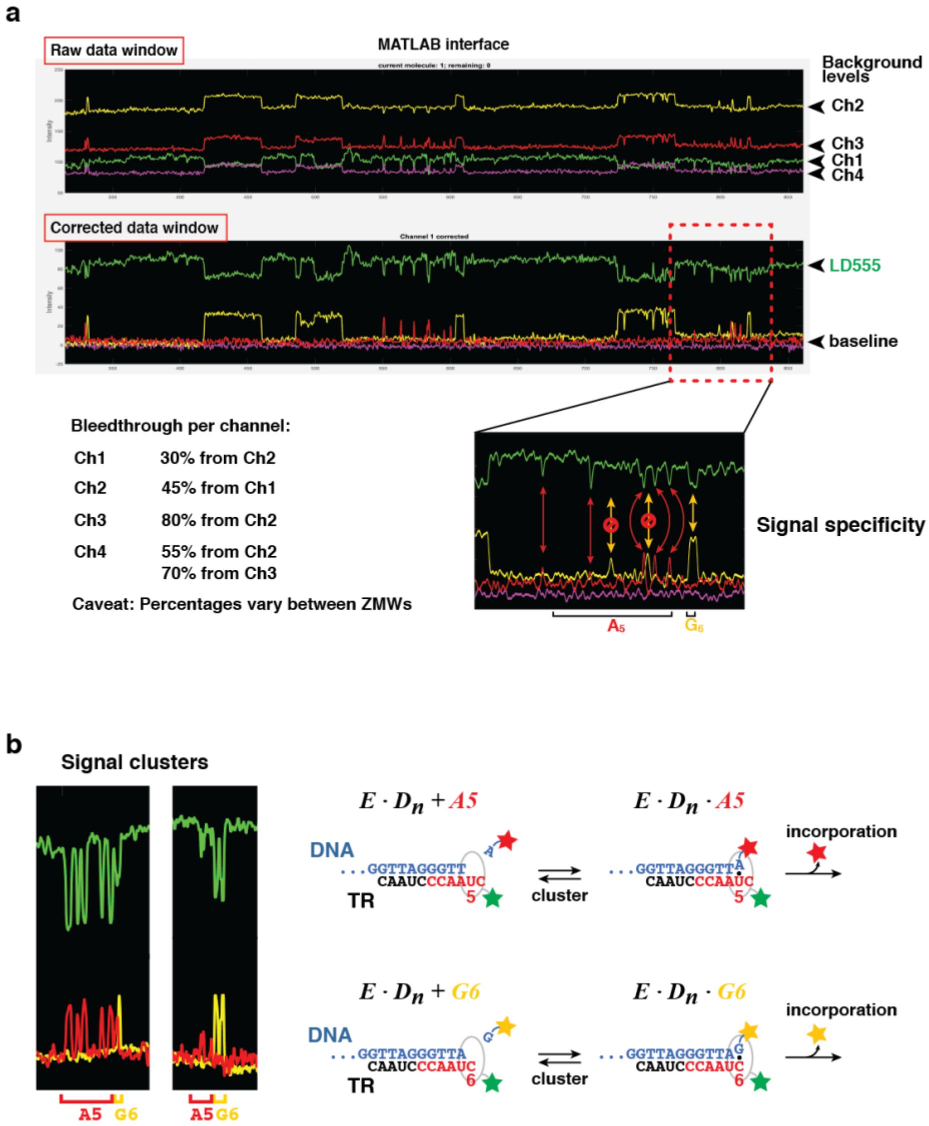

Bleedthrough per channel:

Ch1	30% from Ch2
Ch2	45% from Ch1
Ch3	80% from Ch2
Ch4	55% from Ch2 70% from Ch3

Caveat: Percentages vary between ZMWs

Figure S8. a. Crosstalk correction is performed in Matlab through relative signal subtraction. Percentages of relative bleed-through are given below. Values vary between ZMWs and are adjusted as needed by visual inspection of the respective trace. Enlarged section of the example trace shows anti-correlated (true) FRET events for an A5-cluster followed by a short G6 cluster. Bleed-through correction aids in the visual detection of unspecific Ch2 (yellow) events as highlighted by crossed arrows. **b.** FRET-pulses are heterogeneous and can appear as clusters, indicating nucleotide association and dissociation at a particular template position. Eventual incorporation leads to release of the fluorescence dye after nucleotide hydrolysis and loss of FRET, cf. Fig.3A.

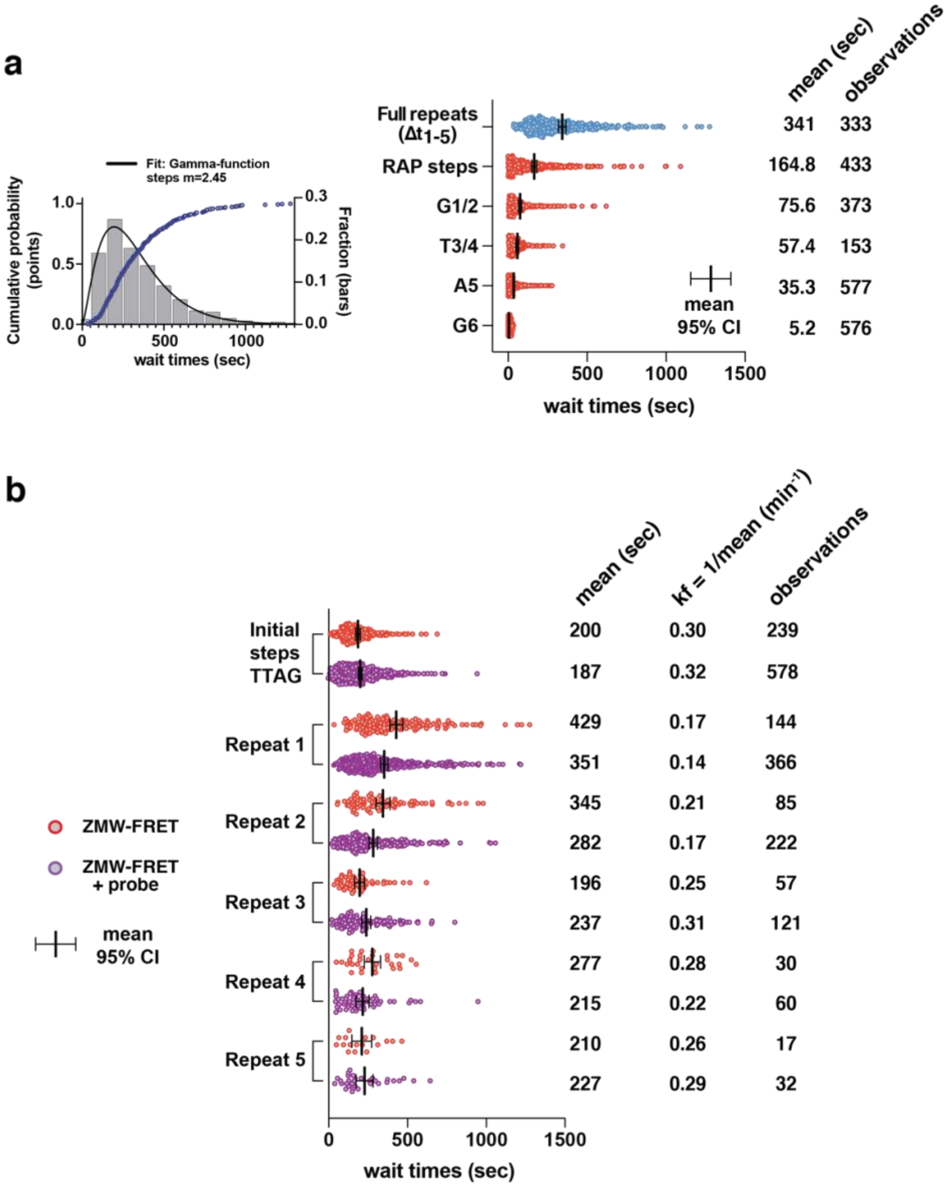

Figure S9. a. Wait time frequency distributions of full repeats and repeat sub-steps, cf. Fig.4B. The Gamma-function fit (Matlab MEMLET) indicates multiple rate-contributing steps within given repeats. At right, time distributions for the population of full repeats, as well as for repeat sub-steps are given with their mean and 95% confidence interval. **b.** Wait time distributions are given for individual repeats across two independent datasets in absence (red) and presence (magenta) of DNA probe, respectively. Wait times for the initial completion of the telomeric primer (TTAGGG)3 are included. The mean and 95% confidence intervals are indicated. Forward rate constants are calculated as kf = 1/mean to describe an individual repeat as single irreversible step.

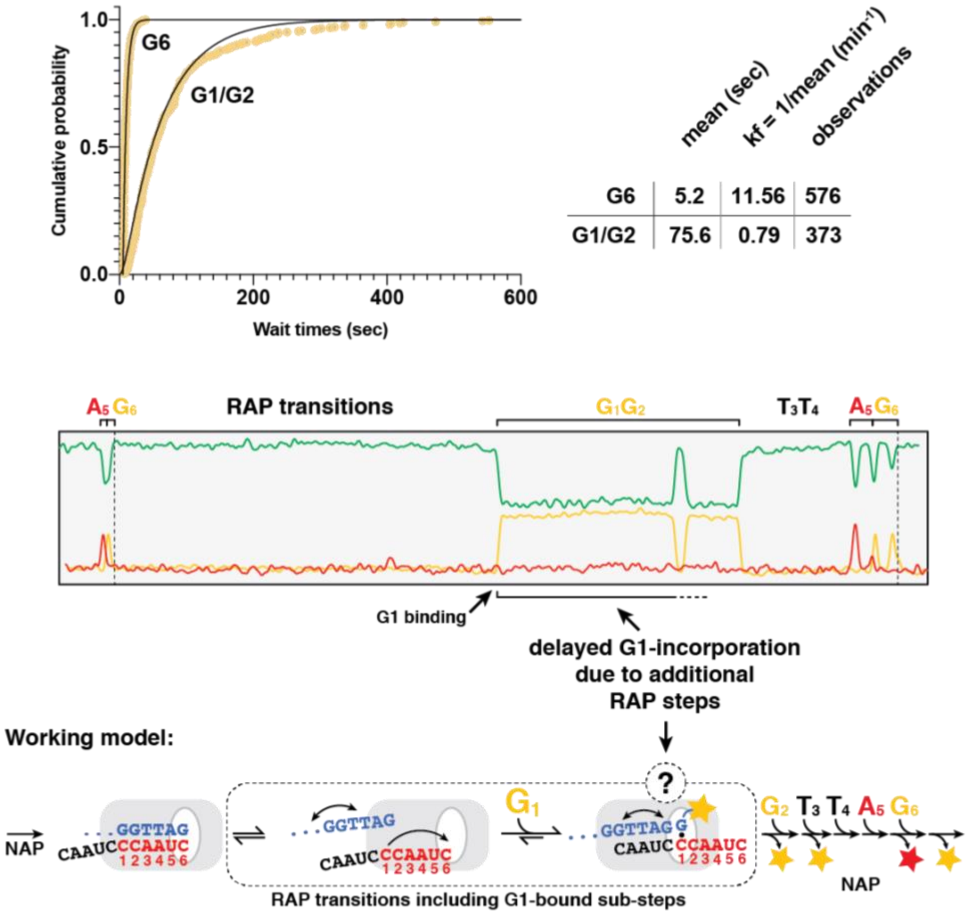

	mean (sec)	kf = 1/mean (min^{-1})	observations
G6	5.2	11.56	576
G1/G2	75.6	0.79	373

Figure S10. Comparison of cumulative frequency wait time distributions of G6 and G1/G2 clusters. Top panel, comparison of cumulative frequency wait time distributions of G6 and G1/G2 clusters. Single-exponential (G6) and double-exponential (G1/G2) fits are in black. Single-step rate constants are given for conceptual simplification and were calculated as kf = 1/mean. Below, example trace highlighting the prolonged life-times of G1/G2 clusters. The model schematic assigns a potential mechanism of mandatory RAP steps that delay G1-incorporation, resulting in prolonged dG1 dwell times as shown in Fig.4B and Fig.5.

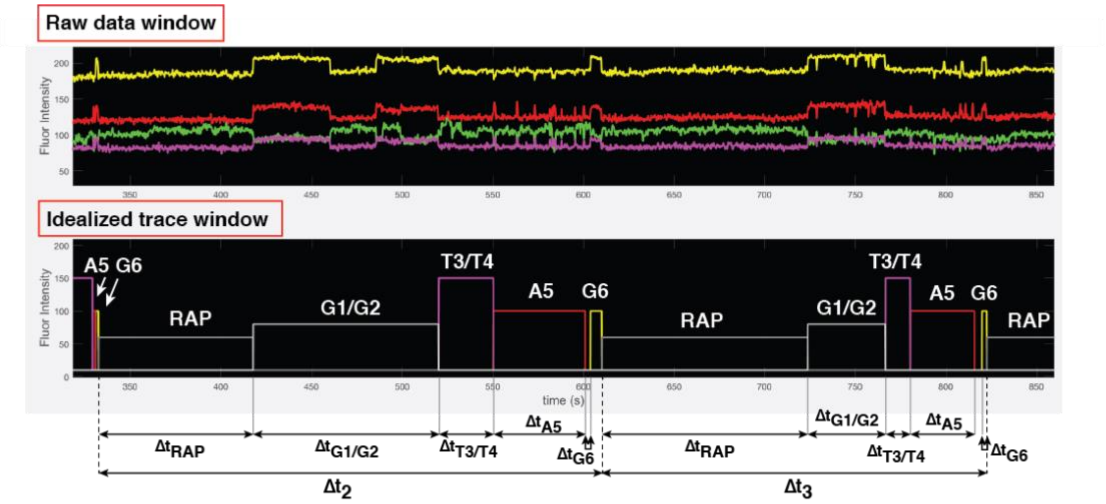

Figure S11. State assignment is performed manually in Matlab and raw data traces are converted to an "idealized state trace". The amplitudes of states are set to arbitrary values for visual distinction. Individual wait times between state transitions are extracted and analyzed as needed.

Table S1. Oligonucleotides used in this study (5′ to 3′).

DNA oligonucleotides were purchased from Integrated DNA Technologies, modified RNA fragments from Dharmacon.

Activity assay primer (5’ ^{32}P-labeled)	TTAGGGTTAGGGTTAGGG
RS telomerase primer	Biotin-TTAGGGTTAGGGTTAGGG
DNA probe (Cy5.5 labeled)	5AmMC6-CCCTAACCCTAACCC
hTR-t/PK RNA fragment (32-62)	GGGCCAUUUU(-5-N-U-)UGUCUAACCCUAACUGAGAA
DNA splint	CAGCGCGCGGGGAGCAAAAGCACGGCGCCTACGCCCTTCTCAGTTAGGGTTAGACAAAAAATGGCCACCACCCCTCCCAGG
IVT template T7 hTR 32 forward	TAATACGACTCACTATAGGGCCATTTTTTGTCTAACCC
IVT template hTR 195 reverse	AACGGGCCAGCAGCTGAC
IVT template T7 hTR 239 forward	TAATACGACTCACTATAGAACCCCGCCTGG
IVT template T7 hTR 328 reverse	GACCCGCGGCTGACAGAG
IVT template T7 hTR 63 forward	TAATACGACTCACTATAGGGCGTAGGCGCCGTG

Table S2. Modal band intensity analysis of telomerase kinetics

	Repeat#	10 min	20 min	30 min	40 min	50 min	60 min
Native telomerase	0	**33**	28	26	26	28	37
	1	14	**19**	18	17	15	15
	2	7	13	**16**	15	14	11
	3	4	7	**9**	**9**	7	7
	4	2	5	7	**8**	7	6
	5	3	4	4	6	**10**	4
	6	4	4	4	7	6	**8**
U42 Labeled telomerase	0	**100**	84	64	53	56	62
	1	38	**59**	46	27	33	29
	2	13	32	**39**	29	30	28
	3	6	19	**24**	21	14	17
	4	4	11	20	**28**	18	23
	5	2	5	10	15	**25**	23
	6	5	5	9	13	21	**27**

Table S2. Modal band intensities (highlighted in yellow) based on SAFA analysis (1) normalized to 100 for the 0th repeat 10 min time point for the U42-labeled telomerase preparation. (red) Note the high intensity for the 0th repeat 60 min time point in the native telomerase sample was due to smearing from the primer band.

Table S3. Fit parameters for kinetic lifetime distributions of telomerase bound and unbound states shown in Fig. 5.

Fitted Data	sample size, n	Function	Log-likelihood	A1	k1 (sec^{-1}	1-A (A2	k2 (sec^{-1})
dG bound (t_{bound})	2,198	single exponential	-6,968	NA	0.16	NA	NA
dG bound (t_{bound})	2,198	double exponential	-6,634	0.58	0.10	0.42	0.85
dA bound (t_{bound})	1,958	single exponential	-2,429	NA	0.87	NA	NA
dA bound (t_{bound})	1,958	double exponential	NA	NA	NA	NA	NA
dG unbound ($t_{unbound}$)	1,999	single exponential	-11,353	NA	0.018	NA	NA
dG unbound ($t_{unbound}$)	1,999	double exponential	-10,279	0.57	0.16	0.43	0.0082
dA unbound ($t_{unbound}$)	1,958	single exponential	-9,587	NA	0.018	NA	NA
dA unbound ($t_{unbound}$)	1,958	double exponential	-8,340	0.75	0.11	0.25	0.005

Single exponential fit function: F(x) = k1*exp(-k1*t)
Double exponential fit function: F(x) = A*k1*exp(-k1*t)+(1-A)*k2*exp(-k2*t)

References

1. Das, R., A. Laederach, S. M. Pearlman, D. Herschlag, and R. B. Altman. 2005. SAFA: semi-automated footprinting analysis software for high-throughput quantification of nucleic acid footprinting experiments. *RNA*. 11(3):344-354, doi: 10.1261/rna.7214405,
2. Peng, Y., I. S. Mian, and N. F. Lue. 2001. Analysis of telomerase processivity: mechanistic similarity to HIV-1 reverse transcriptase and role in telomere maintenance. *Mol Cell*. 7(6):1201-1211, doi: 10.1016/s1097-2765(01)00268-4,
3. Bagshaw, C. R., J. Hentschel, and M. D. Stone. 2021. The Processivity of Telomerase: Insights from Kinetic Simulations and Analyses. *Molecules*. 26(24), doi: 10.3390/molecules26247532,

CHAPTER 3: The interplay of TPP1-POT1-TIN2 and DNA structure during telomerase recruitment to telomeres

Abstract

Telomerase is essential for maintaining genome integrity in eukaryotes. Telomerase activity is regulated by the telomere-associated protein complex shelterin. The shelterin sub-complex TIN2-POT1-TPP1 (TPT) regulates telomere end protection, telomerase recruitment, and telomerase-catalyzed DNA synthesis. However, the molecular mechanism for how TPT both confers telomere end protection and positively regulates telomerase activity remains poorly defined. Here, we employ a single-molecule FRET approach to interrogate the effect of TPT on telomerase recruitment to the 3'-end of model telomeric DNA substrates in vitro. Experiments performed in conditions that disfavor G-quadruplex (GQ) folding in single-stranded telomeric DNA substrate significantly enhance recruitment efficiency. This result is consistent with a model wherein GQ structure antagonizes telomerase binding to single-stranded telomeric DNA. As expected, pre-binding of the model telomeric DNA substrate with TPT, a known GQ resolving protein complex, enhances telomerase recruitment efficiency. Surprisingly, the presence of a stoichiometric excess of TPT on the telomeric DNA was insufficient to eliminate the negative impact of GQ folding on telomerase recruitment efficiency in vitro. Taken together, our results demonstrate how the intrinsic propensity of single-stranded telomeric DNA to fold into GQ structures contributes to regulation of telomerase recruitment even in the presence of telomere-associated proteins.

INTRODUCTION

Telomeres consist of hexameric DNA repeats (GGTTAG in humans) and play a pivotal role in preserving the genomic integrity of eukaryotic chromosomes. In humans they encompass a lengthy double-stranded (ds) region (~9-15 kilobase pairs) and a single-stranded (ss) G-rich 3' tail (~90-150 nucleotides) (1-4). Telomere DNA is safeguarded by the shelterin complex which ensures protection from DNA repair machinery and prevents chromosomal instability (4).

Notably, mutations compromising the DNA binding properties of shelterin components can lead to severe chromosome abnormalities, emphasizing the critical role of this complex in maintaining genomic stability (3,5,6).

Telomere shortening with each cell division is driven by the end-replication problem and poses a threat to cellular viability (7,8). The end-replication problem arises due to the inability of conventional DNA replication machinery to completely replicate each DNA strand, which leads to erosion of terminal DNA. When telomeres reach a critically short length, most cells enter pathways that induce senescence or undergo apoptosis. Highly proliferative cells have evolved a countermeasure in the form of telomerase, a ribonucleoprotein consisting of telomerase reverse transcriptase (hTERT in humans), the integral telomerase RNA (hTR) subunit and several additional species-specific telomerase-associated proteins (9,10). During S-phase, telomerase is recruited to telomeres where it utilizes its internal RNA template to direct the processive synthesis of telomeric DNA repeats, a feature known as repeat addition processivity (RAP) (11,12). Careful regulation of telomerase activity is essential for cell health, as telomerase deficiencies lead to telomere biology disorders while aberrant telomerase activation is implicated in about 90% of cancers (13,14).

The shelterin sub-complex TIN2-POT1-TPP1 (TPT) is crucial for the protection of telomeres and the regulation of telomerase activity (15–17). The POT1 protein binds to the ss telomeric DNA to prevent it from being recognized as a site of DNA damage (18). TPP1, on the other hand, scaffolds POT1 and TIN2, which can bind to the dsDNA binding TRF1 and TRF2 proteins of shelterin (4). Moreover, TPP1 recruits telomerase to telomeres through an interaction with hTERT and thus regulates telomerase activity (15,19). TPT has also been shown to stimulate telomerase processivity in vitro (20). However, the molecular mechanism by which TPT facilitates telomerase recruitment and processivity while preventing dangerous processing by DNA damage response machinery is not well understood.

Our study builds on recent cryo-EM studies that have brought new insights into the structural basis of telomerase regulation by TPT (21). Telomerase was bound to a $(TTAGGG)_5$ primer and TPT was added to yield a TPT-telomerase-DNA complex. High-resolution imaging identified crucial regions within the telomerase essential N-terminal (TEN) domain and the insertion-in-fingers domain (IFD) of hTERT that highlight the significance of their interaction with TPP1 in telomerase regulation. POT1 exhibits greater flexibility than TPP1 and forms a gate in front of the telomerase active site. Notably, POT1 not only interacts with the DNA substrate as shown previously but also with hTERT. The proposed model from this structure posits that TPP1 and POT1 collaboratively facilitate telomerase association with telomeric DNA, with TPP1 stabilizing the flexible TEN domain and POT1 enhancing DNA interaction with the TEN and IFD domains of hTERT. However, these structural advances were unable to resolve the details of the dynamics of TPT-mediated telomerase recruitment.

Here, we employ several single-molecule Förster Resonance Energy Transfer (smFRET) - based assays to study TPT-DNA interactions and telomerase recruitment efficiency on model telomeric DNA substrates. In addition, by studying the TPT-DNA complexes in different salt conditions (KCl or LiCl) we investigate how telomeric DNA structure impacts telomerase recruitment, even in the presence of TPT. We find that TPT binds to a five-repeat $(TTAGGG)_5$ telomeric DNA substrate (5R) with low nanomolar affinity. Conditions that promote the formation of intramolecular G-Quadruplex (GQ) structures (i.e. the presence of K+ ions) reduce the affinity of TPT binding when compared to the same interaction measured in buffers disfavoring GQ formation (i.e. the presence of Li+). This is consistent with the notion that GQ structures can antagonize TPT binding. Using a novel single-molecule assay that directly monitors binding of telomerase to the 3’ end of DNA substrates by FRET, we demonstrate that conditions that favor GQ folding result in lower telomerase binding efficiency. Surprisingly, this result persists in the presence of TPT, suggesting that DNA structure contributes to regulation of telomerase recruitment even when known GQ-resolving proteins are bound to the telomeric substrate.

RESULTS

To monitor telomerase-DNA dynamics at telomere ends during recruitment, and to build on recent structural insights, we designed a single-stranded DNA (ssDNA) construct that comprises five telomeric repeats (5R) terminating in TTAGGG-3’ and a 5’ 19-nucleotide non-telomeric handle (Fig. 1A, Table S1). The guanine-rich and repetitive properties of telomeric ssDNA promote G-quadruplex (GQ) formation (22,23), which can inhibit telomerase binding and activity (24) but was also shown to promote processivity within an actively extending

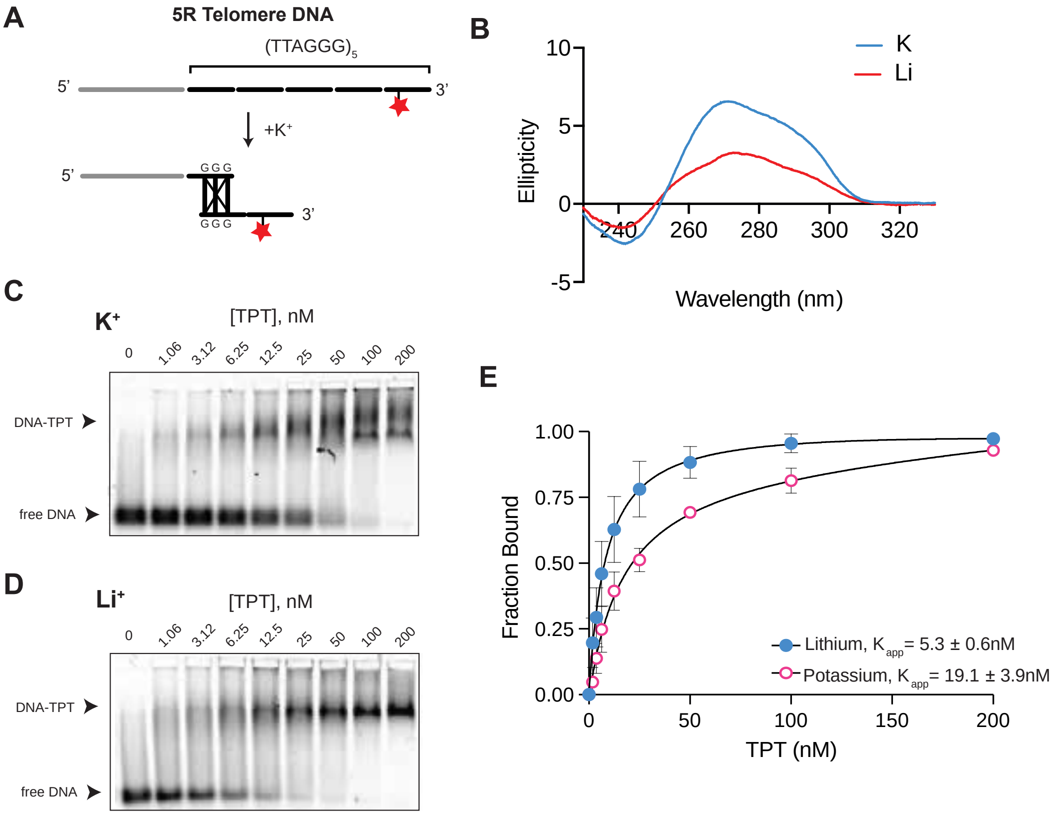

Figure 1. DNA structure and protein binding analysis and of a telomeric DNA substrate (5R). A. Cartoon schematic of a five-repeat telomeric oligo folding G-quadruplex structures in presence of K+. Cy5-labeling at T6 from the 3’ end allows for use in smFRET assays and detection in electromobility shift assays (EMSA). **B.** Circular dichroism of 5R revealed formation of hybrid-form GQs in K+ (blue) but not in Li+ (red). **C.** Electromobility shift assays performed at 5 nM DNA and increasing TPT concentrations show a differential banding pattern in K+ (bottom) compared to Li+ (top). D. EMSA data was analyzed using a quadratic fit and revealed apparent dissociation constants of TPT for 5R in both cation conditions.

telomerase complex (25). POT1, and therefore TPT, can resolve these structures and bind telomeric DNA with high affinity (26,27).

We first aimed to determine whether 5R can form GQs under our experimental conditions. To evaluate the secondary structure of 5R, we performed circular dichroism (CD) spectroscopy analysis in potassium (K^+) and lithium (Li^+) conditions. It is well documented that potassium ions can be coordinated within and stabilize GQ structure (28). The monovalent cations neutralize the buildup of negative charge from electronegative oxygen ions at the center of each G-quartet. In contrast, the smaller atomic radius of lithium prevents this cation from effectively stabilizing GQ structure. Our CD data show the hallmark ellipticity peaks of hybrid GQ structure in 50 mM potassium conditions, with a negative peak at 245 nm, and positive peaks at 265 nm and 290 nm (29). This result confirms that the 5R DNA construct forms GQ structure in potassium conditions. In lithium conditions the negative peak at 245 nm persists, but the peaks at 265 nm and 290 nm are replaced by a single peak at ~270 nm. This result indicates that lithium may facilitate the formation of transient GQ or related intermediate structures within the 5R DNA but does not substantially stabilize the hybrid GQ structure observed in K^+ (Fig. 1B).

We next measured the binding of TPT to the model 5R telomeric DNA substrate. The 5R DNA contains multiple POT1-binding sites (5'-TAGGGTTAG-3') and, in theory, a maximum of two sites can be bound simultaneously (Fig. 2A) (30). However, binding of TPT to ssDNA has not been explored in detail and the large size of the heterotrimeric complex might prevent simultaneous binding of more than one TPT complex to 5R DNA due to steric hindrance. To address this question, we used electromobility shift assays (EMSA) to measure the formation of TPT-5R complexes. Experiments were performed in either Li^+ or K^+ binding conditions to analyze the effect of GQ stability on TPT binding affinity (Fig. 1C and D). All experiments were conducted using human TPT comprised of full-length versions of each protein subunit co-expressed and purified to homogeneity (Supplemental Fig. S1).

Importantly, all EMSAs were conducted using a Cy5 labeled 5R DNA so that the results of ensemble biochemical experiments can be directly related to our subsequent smFRET experiments. To ensure the presence of the internal Cy5 dye label on the 5R DNA does not substantially perturb binding, we conducted experiments with a POT1 ssDNA binding substrate comprised of three telomeric DNA repeats (mut3R) but harboring mutations that force POT1 to bind to the binding site most proximal to the 3' end where the internal Cy5 dye is located (Supplementary Fig. S2). We observed robust binding of POT1 to Cy5-mut3R substrate, with a KD_{app} ~ 3nM, consistent with previous binding affinities reported for the POT1-DNA interaction (31). In the reported POT1-DNA crystal structure (PDB 1XJV) the dT that is labeled in our Cy5-labed mut3R and 5R DNA substrates, is coaxially stacked with two nearby tyrosine moieties and makes several base-specific polar contacts with POT1 (32). The consequence of this geometry is that the exocyclic methyl group at the C5-position of the dT base, where the Cy5 is conjugated via a 12-carbon flexible linker, is oriented outward toward the solvent (Supplementary Fig. S2). Taken together, we conclude that the site-specific conjugation of a Cy5 dye to our 5R substrate does not perturb POT1-DNA interactions.

Binding isotherms from multiple experimental replicates were fit with a quadratic binding expression to account for ligand depletion across the titration range. Our results yielded apparent dissociation constants (Kd_{app}) of 5.3 ± 0.6 nM in lithium and 19.1 ± 3.9 nM in potassium (Fig. 1E). The observed difference in dissociation constants between Li^+ and K^+ aligns with expectations of lower binding affinity in potassium due to the energetic penalty incurred by protein-mediated GQ unfolding. Interestingly, we noted a qualitative difference in the EMSA banding patterns between the two cation conditions. In Li^+ the binding of TPT shifts the 5R DNA to a single high molecular weight TPT-DNA complex that increases in intensity with increasing TPT concentration (Fig. 1D). In contrast, the same experiment conducted in K^+ gave rise to a single high molecular weight complex at low/mid TPT concentrations, but then a more discrete second band emerged at the highest TPT concentrations (Fig. 1C). As a control, EMSAs were also performed on the same 5R DNA substrate with just the purified full-length POT1 protein (Supplemental Fig. S3). These EMSAs showed the emergence of a lower molecular weight shift at low protein concentration, while a second higher molecular band emerges at higher protein concentrations in both cation conditions. This result is consistent with two POT1 proteins binding to the 5R DNA substrate simultaneously. Together, our results show that TPT binds to our dye-labeled 5R telomeric DNA substrate with high affinity and that heterogeneity within the TPT-DNA complex persists when binding in the presence of the GQ stabilizing K^+ cation.

We next sought to examine the structural properties of TPT-5R complexes observed in our bulk experiments using smFRET. For this purpose, we designed a 5R construct that is site-specifically labeled with both a FRET donor and acceptor dye (Fig. 2A), together with a 5' biotin moiety to enable surface immobilization and single-molecule imaging by total internal reflection fluorescence (TIRF) microscopy. In principle, this 5R construct will report on DNA structural dynamics within the 5R ssDNA in absence and presence of TPT (Fig. 2A). In the absence of TPT 5R exhibits a heterogenous FRET behavior with populations centered at ~0.45 and ~0.6 in K^+ (Fig. 2B). Individual smFRET time trajectories in this condition reveal dynamic interconversion of the 5R ssDNA between well-defined FRET states, likely representing interconversion between different conformational GQ isomers. In the presence of Li^+, the FRET distribution is less heterogenous, with a primary FRET population centered at ~0.45 and a small additional peak at ~ 0.6 (Fig. 2C). Single-molecule FRET traces in Li+ reveal a primarily stable FRET behavior with transient sampling of a higher FRET conformation. Next, we incubated surface-immobilized 5R telomeric DNA in the presence of 100 nM TPT, a concentration expected to saturate binding of the DNA substrate. When TPT is introduced in the presence of K^+ we observe persistent FRET heterogeneity, with defined peaks at ~0.3. ~0.45, and ~0.6 (Fig. 2D). In contrast, the same amount of TPT introduced to 5R in Li^+ results in a predominant low FRET peak centered at ~0.3, with several minor FRET populations also present (Fig. 2E). The TPT-dependent emergence of a low FRET peak in both K^+ and Li^+

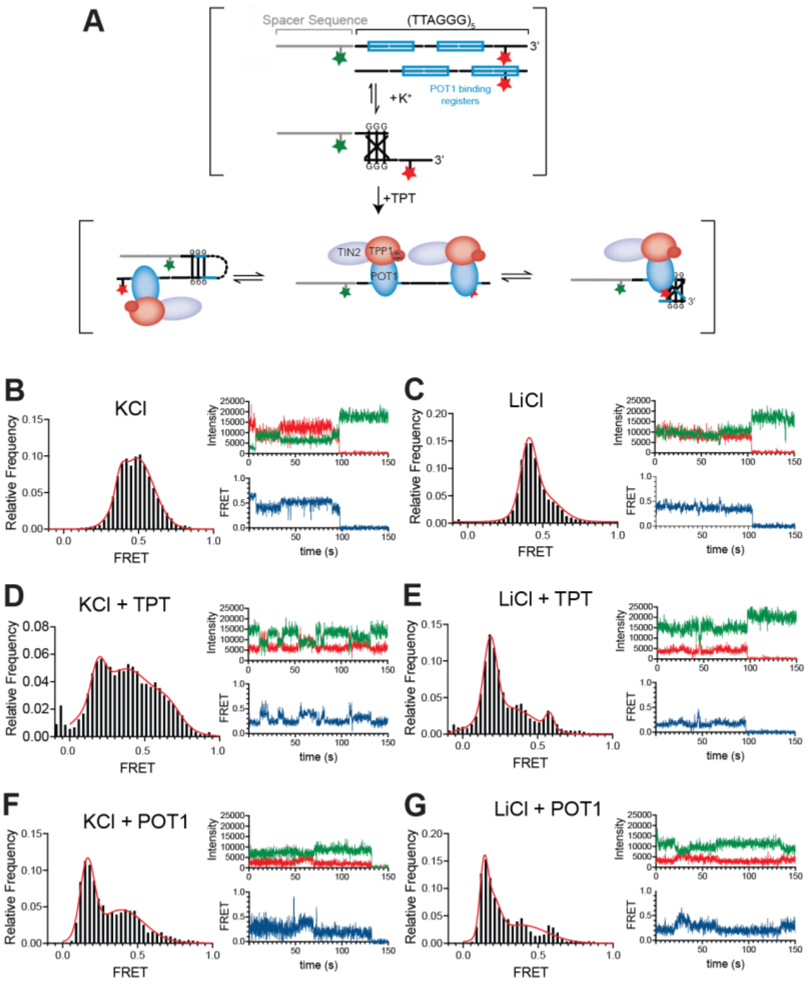

Figure 2. A single-molecule FRET assay reveals DNA dynamics on naked and TPT-bound 5R DNA. A. Cartoon schematic of the smFRET assay. Donor and acceptor dyes on either end of the telomeric sequence report on intramolecular DNA structure formation and dynamics. Addition of TPT could disrupt DNA structure and lead to a change in FRET. **B.** 5R in K+ yielded two FRET populations centered at ~0.45 and 0.6 FRET (left). Single-molecule analysis revealed interconversion of FRET states, indicating DNA folding dynamics (right). **C.** 5R in Li+ resulted in a primary FRET population centered at ~0.45 and a minor population at ~0.6 (left). Analysis of individual traces revealed long dwell times at ~0.45 FRET with short interconversions to ~0.6 FRET. **D.** Addition of TPT to 5R in K+ resulted in the appearance of a low FRET peak at ~0.2 while a majority of the ~0.45 and ~0.6 FRET population remained (left). Analysis of individual traces shows dynamic interconversion of FRET states (right). **E.** Addition of TPT to 5R in Li+ resulted in the appearance of a low FRET peak at ~0.2 while the majority of the ~0.45 and ~0.6 FRET disappeared (left). Analysis of individual traces revealed long dwell times at ~0.2 FRET with short interconversions to higher FRET states (left). **F and G.** Addition of POT1 to 5R in K+ and Li+ resulted in the appearance of a low FRET peak at ~0.2 and a minor FRET peak centered at ~0.45 (left). Analysis of individual traces revealed long dwell times at ~0.2 FRET with short interconversions to higher FRET states (right).

indicates that binding of the complex to 5R extends the ssDNA, as has been shown for other protein-DNA systems studies by smFRET (33). However, in the presence of K^+, the persistence of higher FRET peaks suggests that GQ structure, or other stable DNA conformation, can still occur within the TPT-DNA complex. To test if the presence of TIN2 and TPP1 impacts the structural properties of the protein-DNA complex, we repeated the experiment using just POT1. Addition of 100 nM POT1 to 5R in the presence of either K^+ or Li^+ resulted in the emergence of a predominant FRET peak at ~0.2 FRET (Fig. 3F and G). Thus, we conclude that POT1 alone is better able to resolve DNA structure within the 5R telomeric DNA complex when compared to the TPT complex.

Having analyzed the structural properties of the telomeric DNA substrate in the presence and absence of TPT, we next set out to investigate how DNA structure and TPT combine to affect telomerase recruitment in vitro. To this end, we employed a smFRET assay that reports on telomerase pulldown on 5R DNA. As previously reported, a catalytically active human telomerase enzyme can be reconstituted and purified from rabbit reticulocyte lysates (RRLs) using a two-piece RNA strategy (25). Telomerase enzyme made in this way consists of FLAG-tagged human telomerase reverse transcriptase (hTERT) and the essential template/pseudoknot and CR4/5 fragments of human telomerase RNA (hTR). In a typical experiment that aims to maximize the binding of telomerase to the model 5R DNA substrate, we preincubate the enzyme and DNA together in Li^+ buffer. Pre-bound complexes are then surface immobilized on a quartz microscope slide and imaged in K^+ buffer (Fig. 3A). Previous work using a similar telomerase reconstitution method demonstrated that a site-specific donor dye label located at hTR position U42 can report on an acceptor-labeled DNA 3'-end docking in the template RNA-DNA substrate binding site, resulting in a characteristic high FRET state of ~0.6-0.8 (Fig. 3B) (34). This interpretation is further supported by analysis of recent cryoEM structures of the telomerase-DNA complex (Fig. 3C) (35). Therefore, for the purposes of this study, we hereafter refer to all telomerase-DNA complexes with FRET greater than 0.5 as the 'recruited telomerase complex'. Crucially, dye-labeled enzyme retained catalytic activity when assayed in direct primer extension assays and showed the expected activity and processivity stimulation in the presence of purified TPT (Fig. 3D). Moreover, addition of dNTPs to surface-immobilized stalled telomerase-DNA complexes activated catalysis in the smFRET assay and

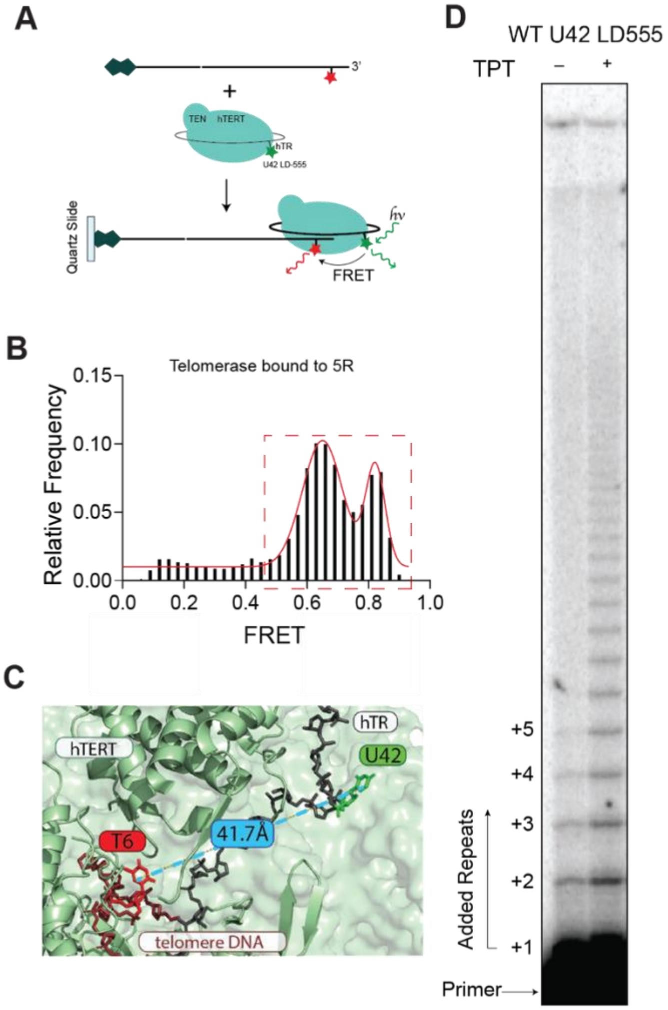

Figure 3. A single-molecule FRET assay reports on telomerase recruitment. A. Cartoon schematic of the smFRET assay. A minimal telomerase enzyme labeled with a donor dye (LD555) at U42 of hTR base-pairs with the 3' end of 5R harboring an acceptor dye (Cy5). This leads to FRETing between the dye-pair when in proximity (bottom). **B.** Telomerase enzyme stably bound to 5R produced two FRET populations at ~0.65 and ~0.8, indicating proximity of donor and acceptor dyes. **C.** Cartoon schematic of the proximity of U42 of hTR and the dye-labeled nucleotide on the telomere DNA. **D.** Primer extension assays using unlabeled and LD555-labeled telomerase on 5R primer. The labeling site at U42 of hTR does not disrupt enzyme function, indicating that the dye position does not prevent telomerase recruitment and activity.

resulted in the time-dependent reduction of the ~0.6 FRET peak (Supplemental Fig. S4). We note that the second FRET~0.8 population did not change upon dNTP addition. This result indicates that our recruitment complexes represent a mixture of states, one that is primed for catalytic activity (FRET ~0.6) and another that has the 3' end of the DNA substrate in close proximity to the active site but is not competent for catalysis (FRET ~0.8).

We next investigated the efficiency of telomerase recruitment to the 5R telomeric DNA substrate using the smFRET pull down assay under different experimental conditions. First, we incubated telomerase with the 5R DNA in either K^+ or Li^+ conditions. Purified U42-labeled telomerase was pre-incubated with 5R DNA in the indicated conditions and then surface-immobilized for analysis by smFRET (see materials and methods for details) (Fig. 4A). To measure 5R DNA immobilization efficiency, data were collected using red laser excitation to directly measure the surface density of the Cy5 labeled 5R DNA. Next, the green laser was used to measure the number of telomerase-DNA complexes exhibiting FRET between the donor dye incorporated in telomerase and the acceptor dye in the 5R DNA (Supplementary Fig. S5). By dividing the total number of complexes exhibiting FRET greater than 0.5 (telomerase recruitment complexes) (Fig. 4B, red boxes) by the total amount of 5R DNA immobilized, we calculate the telomerase recruitment efficiency. Using this analysis approach, we found a ~3-fold increase in telomerase recruitment efficiency in Li^+ versus K^+ (Fig. 4C). This result is consistent with stable GQ structure in the presence of K^+ inhibiting telomerase recruitment to the 5R DNA substrate.

In order to study the impact of TPT binding to the 5R telomeric DNA substrate, we preincubated TPT protein complex in a stoichiometric excess over the 5R DNA. However, at a large molar excess of TPT in our binding reactions, free TPT could prevent binding of telomerase to the DNA substrate. Therefore, to ascertain how much TPT complex was needed to saturate binding to the 5R substrate, we stoichiometrically titrated the TPT complex against our labeled 5R substrate described in Figure 2. We elected to use a starting concentration of 50 nM FRET-labeled 5R DNA, as this is the concentration of DNA primer typically used in our bulk primer extension assays, which show effective TPT-dependent stimulation of telomerase activity and processivity. We added TPT complex in a 1:1, 1:2, and 1:4 stoichiometry of DNA:protein and then diluted samples 50-fold for surface immobilization prior to single-molecule imaging. As

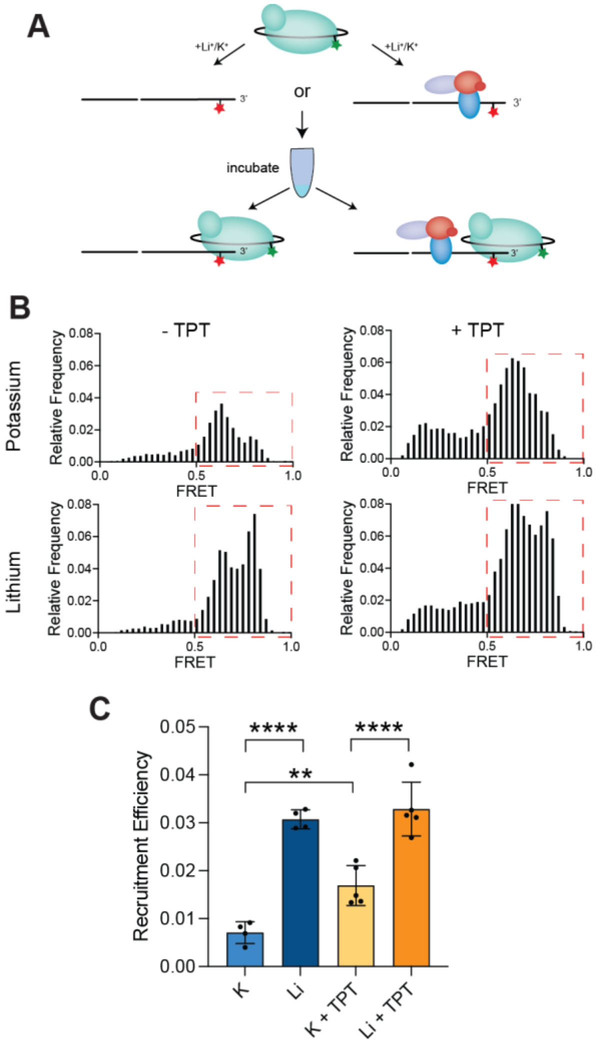

Figure 4. Telomerase recruitment to telomeres is regulated by DNA structure and TPT. A. Cartoon schematic of the telomerase pulldown assay. Telomerase is added to naked DNA or TPT-bound DNA and incubated. DNA is then immobilized on the quartz slide surface. **B.** Histogram data of FRET events across 20 fields of view in each experimental condition. FRET events are normalized for DNA density and FRET values above 0.5 are considered as recruited telomerase enzyme (red box). **C.** Analysis reveals a significant difference in recruitment efficiency between K+ and Li+, even in presence of TPT. Addition of TPT to DNA prior to telomerase pulldown results in an increase in telomerase recruitment efficiency, significantly so in K+.

described above, binding of TPT to the 5R DNA substrate results in a decrease in the observed FRET value due to a more extended conformation of the 5R DNA induced by protein binding. Under our experimental conditions, we found the 1:4 stoichiometry resulted in the formation of a well-defined low FRET peak (Supplementary Fig. S6A), suggesting that this concentration of TPT is sufficient to saturate the DNA. We noted that at the 1:4 stoichiometry of 5R DNA:TPT, we still observed FRET heterogeneity as described in Figure 2. Since our purified telomerase preparations are typically in the low nM concentration range, it was necessary to dilute down the preformed DNA-TPT complexes prior to addition of telomerase. Thus, to ensure that telomerase can still bind to the TPT complex after dilution, we tested the stability of TPT-DNA complex after dilution. To this end, we diluted the preformed TPT-DNA complexes and incubated for varying amounts of time prior to immobilization and single-molecule imaging. Our results suggest that the TPT-DNA complex is stable on the time scale of 10-15 minutes (Supplementary Fig. S6B), allowing sufficient time for telomerase to bind to the complex prior to TPT dissociation.

Next, we performed the in vitro telomerase pulldown experiment in K+ but this time in the presence of TPT. Consistent with previous work in live cells, our experiment revealed that TPT can enhance telomerase recruitment efficiency in vitro in the presence of K^+ (Fig. 4B and C) (36). Surprisingly, the enhancement of telomerase recruitment efficiency by TPT was more pronounced under Li^+ conditions when compared to K^+ conditions (Fig. 4C). Thus, our data suggest that under a more physiological K^+ binding condition, the presence of TPT can facilitate telomerase recruitment to the 3'-end but does not completely suppress the influence of the intrinsic structural properties of the 5R telomeric DNA substrate.

Mutations in telomerase and TPT dissect contributions of protein-protein interactions and DNA structure to recruitment efficiency

To measure the contribution of the well-characterized TPP1-telomerase binding interface to telomerase recruitment efficiency in our smFRET experiments, we introduced several mutations in telomerase and TPP1 that have been described previously (36). A K78E substitution within the TEN domain of hTERT was shown to disrupt a crucial polar contact with TPP1, impairing telomerase recruitment in vivo, and reducing telomerase processivity in the presence of POT1-TPP1 in vitro. Recent structural studies have revealed the proximity of

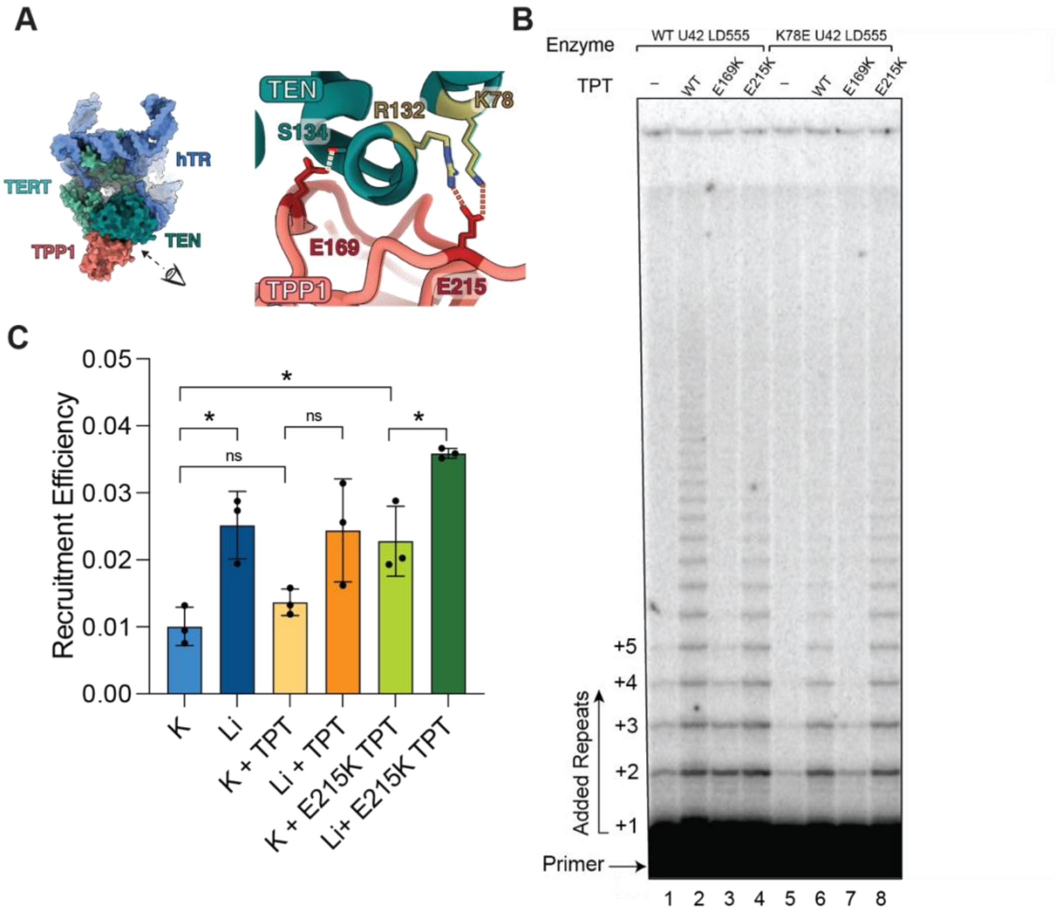

Figure 5. Protein-protein interactions between telomerase and TPP1 increase telomerase recruitment efficiency. A. Cartoon representation of TPP1 E169 and E215, and telomerase K78 amino acid residues. K78 makes interactions with E215 but not with E169 of TPP1. **B.** Primer extension assays comparing the processivity stimulation of wild-type and K78E telomerase by TPT variants. Wild-type TPT is able to boost processivity in wild-type enzyme while stimulating activity, but not processivity in K78E enzyme. E169K TPT has no effect on either enzyme. E215K TPT partially rescues processivity stimulation of K78E mutant while decreasing the processivity of wild-type enzyme. **C.** Comparison of K78E telomerase recruitment efficiency in presence of wild-type and E215K TPT. Wild-type TPT has no significant effect on telomerase recruitment efficiency, while E215K TPT is able to rescue a boost in telomerase recruitment efficiency.

hTERT K78 to TPP1 residues E169 and E215, consistent with previous reports that charge swaps at these TPP1 residues can rescue TPT stimulation, recruitment and activity of telomerase harboring the K78E mutation (Fig. 5A) (21,36)

We first evaluated whether K78E telomerase enzyme made in RRLs with U42 dye-labeled hTR supported telomerase activity and processivity on the 5R telomeric DNA substrate used in our study. To ensure that comparable amounts of WT or K78E telomerase were used in direct primer extension reactions, we quantified the purified telomerase concentration by RNA dot blot (Supplementary Fig. S7). WT and K78E telomerase displayed modest primer extension activity on the 5R primer in the absence of TPT (Fig. 5B, lanes 1 and 5), whereas both enzymes showed boosted activity and processivity in the presence of WT TPT (Fig. 5B, lanes 2 and 6). However, the degree of activity and processivity stimulation by WT TPT for the K78E telomerase was lower than for WT telomerase, as expected (Fig. 5B, lanes 2 and 6). Next, we tested whether charge swaps introduced by the TPP1 E169K or E215K mutations within the TPT complex could rescue the full stimulation for the K78E telomerase enzyme. Interestingly, neither WT nor K78E telomerase were stimulated by TPT containing TPP1 E169K (Fig. 5B, lanes 3 and 7), demonstrating that this mutation disrupts telomerase-TPP1 interactions and is not sufficient to rescue this interaction in the context of K78E telomerase. In contrast, both WT and K78E telomerase were stimulated by TPT containing TPP1 E215K (Fig. 5B, lanes 4 and 8). Notably, the degree of activity and processivity enhancement by TPT containing TPP1 E215K was lower than WT TPT for the WT telomerase enzyme, whereas the K78E telomerase enzyme was better stimulated by TPT carrying the TPP1 E215K mutation. Together, the results of our direct primer extension assays validate our dye-labeled telomerase reagents and indicate that the WT TPT complex enhances both the total activity and processivity of both WT and K78E telomerase. Moreover, introduction of the charge swap in TPP1 by the E215K mutation can recover robust activity and processivity stimulation of the K78E telomerase enzyme.

Having characterized the catalytic activity of our dye-labeled WT and K78E telomerase enzymes in the presence of different TPT complexes, we next explored the impact of these mutations on telomerase recruitment efficiency in our single-molecule assay. In the absence of TPT, K78E telomerase exhibited the same increase in telomerase recruitment efficiency in Li^+ compared to K^+ as observed for WT telomerase (Fig. 5C). The introduction of WT TPT did not boost K78E telomerase recruitment efficiency in either K^+ or Li^+ conditions (Fig. 5C). The impact of GQ folding (comparing K^+ vs Li^+ conditions) on telomerase recruitment was still qualitatively evident in the presence of WT TPT for K78E telomerase; however, this result was not statistically significant as was observed for the WT telomerase enzyme (Fig. 4C). This result demonstrates that our single-molecule recruitment assay reports on the disruption of the hTERT-TPP1 protein binding interaction by the hTERT K78E mutation.

Next, we performed telomerase recruitment experiments using TPT complex harboring the TPP1 E215K mutation. Unlike WT TPT, the presence of E215K TPT complex confers a statistically significant boost in K78E telomerase recruitment efficiency in the presence of K^+ (Fig. 5C), a result that is consistent with our primer extension assays that showed a rescue of K78E telomerase activity and processivity (Fig. 5B). Moreover, the enhanced recruitment efficiency observed in Li^+ versus K^+ persists for the K78E telomerase and E215K TPT (Fig. 5C). Taken together, these results suggest that TPT enhances telomerase recruitment via protein-protein interactions, as previously reported, but the presence of TPT does not completely overcome the refractory impact of GQ folding on telomerase binding to the 3’ end of the 5R telomeric DNA substrate (36,37).

DISCUSSION

Discussion outline

Despite its crucial role in human health and disease, the molecular mechanisms that enable telomerase activity in vivo are not yet fully understood, making it a significant area of ongoing research. A key focus within this field is the regulation of telomerase recruitment to telomeres.

During the S-phase of the cell cycle, when telomerase is active, the number of telomerase molecules roughly matches the number of telomere ends. Additionally, DNA structures and telomere-binding proteins, specifically those in the shelterin complex, protect telomeres from access by DNA repair machinery. This raises an intriguing question: how does telomerase accurately elongate telomeres in cells that express telomerase? Although it is known that the interaction between the shelterin component TPP1 and telomerase is essential for telomerase recruitment in vivo, the precise role of this interaction in the recruitment mechanism remains unclear.

Here, we use a subcomplex of shelterin, Tin2-POT1-TPP1 (TPT) to study the effect of DNA structure and telomeric proteins on telomere DNA dynamics and telomerase recruitment.

We propose a new model of shelterin-mediated telomerase recruitment and simultaneous chromosome protection. In this working model, DNA structure in telomere DNA exists even in the presence of shelterin and negatively regulates telomerase recruitment. At the same time, telomerase interaction with TPP1 promotes telomerase recruitment. Telomerase-TPP1

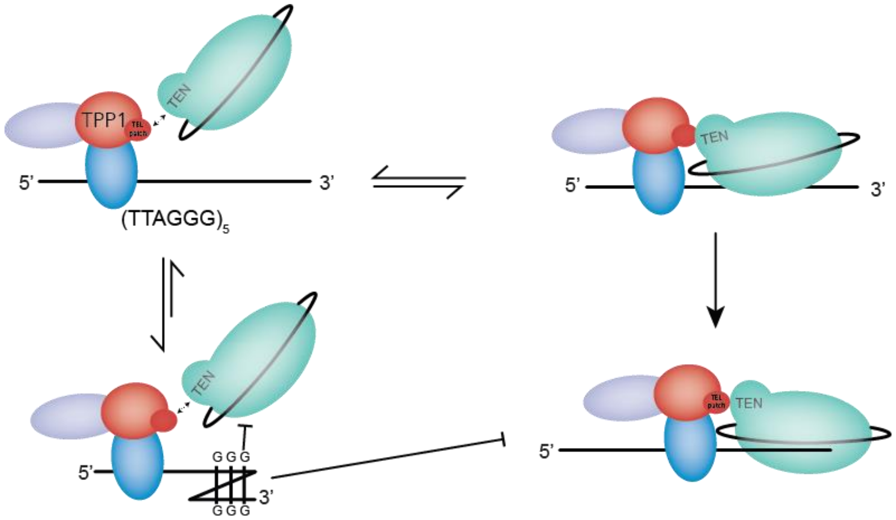

Figure 6. A model for telomerase recruitment regulation. Protein-protein interactions between TPP1 and telomerase increase the local concentration of telomerase at telomeres and retain telomerase at the 3' end. DNA structure formation at telomeres can prevent the telomerase RNA template from base-pairing with 3' telomeric DNA. Dynamic interconversions of DNA structure to an 'open' 3' end allows for complete telomerase recruitment.

interactions increase telomerase retention at the telomere until DNA structure at the 3' end is transiently resolved, which then allows access for telomerase (Fig. 6). Together, these mechanisms may help to regulate proper levels of telomerase activity in telomerase-positive cells.

Using electromobility shift assays we show that a ssDNA primer containing five telomeric repeats can only be bound by one TPT complex at a time, even though it contains two POT1 binding sites (Fig. 1). In contrast, our data show that two POT1 proteins can bind this same primer (Supplemental Fig. S3). This result suggests that five telomeric repeats can only accommodate one TPT complex, supporting the notion that some telomere DNA in the cell likely remains unbound by shelterin. This is in contrast to the common belief that shelterin proteins coat telomere DNA in vivo. (38) While previous studies have shown that telomeric DNA can be coated in shelterin complexes, these studies lacked the shelterin component TIN2, which is essential to POT1 and TPP1 recruitment.

We employed a single-molecule FRET assay to monitor the distance between donor and acceptor dyes on the same. This allows us to probe the structural state of the DNA under various conditions (Fig. 2A). Our findings indicate that TPT is unable to fully unfold the potassium-stabilized DNA structure within a five-repeat telomere primer. In the absence of TPT, the construct displays mid-FRET peaks under both lithium and potassium conditions. This suggests structure formation in potassium and freely jointed chain movement in lithium (Fig. 2B and C). (39) Notably, two distinct mid-FRET peaks are observed in potassium, which we interpret as two different folded conformations of the DNA. When an excess of TPT is added, the mid-FRET peak in lithium conditions largely shifts to a low (0.2) FRET state, indicating DNA unfolding (Fig. 2E). However, a significant mid-FRET peak persists in potassium conditions even after TPT addition (Fig. 2D). In contrast, the addition of POT1 under both cation conditions causes the mid-FRET peaks to largely collapse to a low-FRET peak (Fig. 2F and G). These results are consistent with the distinct EMSA banding patterns observed in 5R-TPT in Li+ or K+ compared to 5R-POT1 (Fig. 1C and D, Supplemental Fig. S3A and B). This suggests that only one TPT complex can bind to a five-repeat ssDNA primer, leaving the remaining unbound DNA free to form structures in the presence of potassium cations. When TPT binds to the most 5' or 3' POT1 binding sites on the ssDNA primer, two full telomeric repeats and two guanines in the adjacent repeat remain unbound. (40) The formation of stable G-triplex structures by three stretches of two guanines has been previously characterized in the thrombin binding adapter. (41, 42) Our data suggest that telomeric DNA may similarly adopt G-triplex formation even in the presence of shelterin. In addition, release of DNA by one of the two OB folds of POT1 can further promote DNA structure formation. Together, these findings imply that ssDNA regions on telomeres, left unbound by TPT, allow transient exposure of free 3' ssDNA, which could be bound by telomerase. Our model does not rule out the possibility that transient unfolding of ssDNA structure may be driven by TPT sliding, as suggested in previous studies. (43-45)

Our results demonstrate that DNA structure impairs telomerase recruitment efficiency, even in the presence of TPT. Using the same DNA primer labeled with Cy5 and a minimally engineered telomerase enzyme tagged with LD555, we found that DNA conformation directly affects telomerase recruitment efficiency (Fig. 3A). Previous studies have shown that TPP1-telomerase interaction is essential for telomerase recruitment but lacked the spatial resolution to assess the structural state of telomeric DNA or the precise positioning of telomerase. (46) In contrast, our single-molecule FRET assay provides nanometer-scale resolution, revealing that structured DNA hinders telomerase recruitment. These findings suggest that TPT alone cannot overcome the barriers posed by G-quadruplexes or other telomeric conformations, highlighting the complexity of telomerase recruitment in vivo.

Consistent with recent structural data, a DNA-bound telomerase results in our dye pair being less than 6nm away from each other, resulting in a high FRET state (Fig. 3C). (47) We consider this state to be a recruited telomerase.

Notably, we identified two distinct, yet TPT-independent high FRET states of 0.65 and 0.8 when telomerase has been recruited (Fig. 3B) Addition of dNTPs results in the disappearance of the ~0.65 FRET peak and is consistent with previous studies using this telomerase construct (Supplemental Fig. S4). (34, 25) In contrast, the ~0.8 FRET peak persists upon dNTP addition (Fig. S4C). Therefore, this peak might represent a DNA-telomerase complex where the primer and hTR labeling positions are in close proximity, but telomerase is not primed for activity. This suggests that a "pre-initiation" complex exists where telomerase is bound to DNA primer but not ideally positioned for activity. Further studies will be required to determine the existence and role of a pre-initiation complex in the telomerase catalytic cycle.

Telomerase recruitment to 5R was more efficient in Li+ than in K+, directly in correlation with the absence of stable GQ structures (Fig. 4C, blue bars). The presence of TPT enhanced telomerase recruitment efficiency in both conditions. Surprisingly, the recruitment efficiency in K+ conditions is still significantly lower in the presence of TPT than that of naked DNA in Li+. This shows that the inhibitory role of GQ structures in K+ cannot be completely overcome by TPT (Fig. 4C). Yet still, TPT presence enhanced telomerase recruitment efficiency in K+ conditions.

We can think of the role of TPT in telomerase recruitment two ways. First, TPP1 interaction with telomerase increases the local concentration of telomerase, thereby increasing the chances of a stochastic telomerase-DNA binding event. The second is that TPP1 interaction with telomerase induces structural changes in the TPT-DNA complex that promotes telomerase binding. We refer to these models as the passive and active models of TPT-stimulated telomerase recruitment, respectively. We reason that if TPT were actively promoting telomerase binding, then the recruitment efficiency of telomerase should not differ between TPT-bound 5R in different cation conditions. In contrast to this, the significant difference in telomerase recruitment efficiency in Li+ and K+¬ conditions remains in the presence of TPT (Fig 4C, yellow and orange bars). Together, our results show that while TPT increases recruitment efficiency of telomerase, its presence on the ssDNA does not abrogate the inhibitory effect of DNA structure formation in K+ conditions as has been traditionally thought. (17, 47)

Finally, we show that disruption of the telomerase-TPP1 interaction surface eliminates the significant stimulation of telomerase recruitment efficiency by TPT. We use the telomerase mutant K78E that has previously been shown to have decreased RAP stimulation in presence of TPP1 compared to wildtype telomerase. (46, 36) This mutant also fails to localize to telomeres in vivo. We confirmed that these findings are consistent for our minimal telomerase construct and (Fig. 5B, lanes 2 and 6). We hypothesized that if the telomerase-TPP1 interaction surface was responsible for a boost in telomerase recruitment efficiency in vitro, then the K78E telomerase mutant should have the same recruitment efficiency in the presence and absence of TPT. Indeed, our results show no significant difference between the naked ssDNA and wildtype TPT conditions (Figure 5C). Importantly, the significant difference of recruitment efficiency between cation conditions remains unchanged. Consistent with recent structural advancements, previous studies have shown that the TPP1 mutant E215K rescues RAP enhancement of the K78E telomerase. (21) We show that this is true for our reagents using primer extension assays (Fig. 5B, lanes 6 and 8). Indeed, addition of the E215K mutant to DNA was able to rescue the recruitment efficiency boost of K78E compared to wildtype TPT (Fig 5C, green bars). This shows that the TPT-telomerase interaction that enhances RAP also enhances telomerase recruitment.

Taken together, our results indicate that while both DNA structure and TPT presence contribute to telomerase recruitment in vitro, DNA structure negatively regulates telomerase while TPT positively regulates telomerase recruitment efficiency.

MATERIALS AND METHODS

CD Measurements

CD spectra were obtained using a Jasco J-1500 CD (Jasco Inc., United States) spectrometer. A quartz cuvette (insert company) with 1 mm or 100 um path lengths were used to acquire CD spectra from 180–350 nm with a 4-nm bandwidth, 0.1-nm step size, and 100 nm/min collection time per data point. The telomeric DNA samples (5R) were diluted to 10 μM stock in TIB containing Lithium or Potassium and placed into the quartz cuvette. The CD spectra were scanned three times, and the average spectrum represents the depicted data.

Electrophoretic Mobility Shift Assays (EMSA)

Electrophoretic Mobility Shift Assays (EMSA) were performed under equilibrium binding conditions using Cy5-labeled DNA oligo. 5 nM DNA oligonucleotides were incubated with TPP1-POT-TIN2 (TPT) at concentrations ranging from 200 nM to 1.56 nM. Reactions were set up in a solution containing 25 μg ml-1 salmon sperm DNA, 0.5 mg ml-1 BSA, 20 mM HEPES (pH 8.0), 2 mM MgCl2, 0.01% NP-40, 5% glycerol and 150 mM LiCl or KCl, as indicated. Protein-DNA complexes were incubated at room temperature for 30 minutes before being separated by gel electrophoresis. Free DNA and TPT-bound DNA were resolved on a 1% Agarose (MB grade, Fisher Scientific cat. 9012-36-6) gel prepared with 0.5× Tris-Borate (TB) buffer run at 4°C in 0.5× TB buffer. Gels were imaged on a Typhoon Phosphorimager (GE Healthcare). Data was quantified using ImageJ and processed with Microsoft Excel software. All experiments were performed in triplicate.

In situ binding of TPT to surface immobilized 5R DNA

Fresh quartz slide channels and buffers were prepared for use in the experiments. Standard T50 Li buffer (10 mM Tris HCl, pH 8.3, 50 mM LiCl) and imaging buffer (TIB) in both Lithium and Potassium variations (50 mM Tris HCl, pH 8.3, 10 mM Trolox, 50 mM LiCl/KCl, 1 mM MgCl2, 0.1 mg mL-1 BSA, 0.8% glucose) were freshly prepared from 10X and 5X stocks respectively, followed by filtration through a 0.2 µm filter. TIB was supplemented with 1% Gloxy (glucose oxidase and catalase oxygen scavenging system) immediately before use. The slide channel was prepared by filling it with 0.2mg mL-1 MPS and incubating for 1 minute. Subsequently, the channel was washed three times with 20 µL T50 LiCl. The channel was then considered ready for use. A 100 nM stock solution of h-5R-double was boiled for 3 minutes at 95°C. A dilution was then made to obtain a 10 pM concentration using T50 LiCl. 40 µL of 10 pM DNA were added to the channel and incubated for ten minutes, followed by a wash consisting of 20 µL of TIB KCl or LiCl, as indicated. For TPT experiments, a 100 nM TPT solution was prepared using TIB (Li or KCl) and supplemented with 1% Gloxy. The TPT solution was added to the channel, and FRET data recording was initiated after waiting for approximately 5 minutes. Histogram data for FRET experiments was recorded in 10 sets of 20 frames (~2s) each for population analysis, and long movies comprising approximately 1500 frames (~180s) were captured for downstream single-molecule analysis.

Stoichiometric TPT binding experiments to 5R DNA measured by smFRET

TPT-DNA binding reactions were set up at 50 nM DNA and 50,100 and 200 nM TPT and incubated for 30 minutes. Reactions were performed in TIB-LiCl. After incubation, reactions were diluted to 125 pM DNA, and 40 µL were immobilized on the quartz slide channel and washed with TIB-KCl supplemented with 1% Gloxy. and 50 mM KCl. Fluorescence intensity data of immobilized complexes was recorded in 10 sets of 20 frames (~2s) each for population analysis and analyzed using in-house MatLab analysis scripts.

Measurement of TPT dissociation from 5R DNA

TPT-DNA binding reactions were set up at 50 nM DNA and incubated for 30 minutes. Reactions were performed in TIB-LiCl/KCl and 200 nM TPT. After incubation, portions of the reaction were diluted to 1nM DNA using TIB-LiCl and incubated for 5, 10, 15 or 30 minutes. After incubation, reactions were diluted to 125 pM DNA, and 40 µL were immediately immobilized on the quartz slide channel and washed with imaging buffer supplemented with 1% gloxy and 50 mM KCl. Fluorescence intensity data of immobilized complexes was recorded in 10 sets of 20 frames (~2s) each for population analysis and analyzed using in-house MatLab analysis scripts.

hTR Fragment Preparation and Labeling

The DNA sequences for the hTR fragments CR4/5 (239-329) and PK (63-195) were amplified from a pBSU1 hTERT plasmid using PCR. Purified PCR products were used for in-vitro transcription (IVT) reactions using T7 RNA polymerase and products were purified with polyacrylamide (PAGE) gel electrophoresis. The PK (63-195) IVT reaction involved addition of 100mM GMP to ensure 5' phosphorylation of the fragment for downstream processing.

The U42 aminoallyl modified PK fragment (32-62) was obtained commercially (Horizon Discovery Group plc, USA) and dye-labeled and purified as described previously with the following exceptions.34 RNA was deprotected prior to the labeling reaction and desalted using a PD Miditrap G-25 column. Instead of Cy3, the self-healing LD555 fluorescent dye (Lumidyne Technologies, Inc.) was used. After labeling, RNA was ethanol precipitated and resuspended in 0.1M TEAA buffer followed by HPLC purification. The product was desalted once again using the PD Miditrap G-25 column and concentrations and labeling efficiencies were determined by Nanodrop. PK Fragments (32-62-LD555 and 63-195) were splint ligated and purified as described previously (25,34).

Telomerase Reconstitution

Minimal human telomerase was reconstituted using the TNT T7 Quick Mix (Promega) system. For each 200 µL of TNT Quick Mix, 5 µg of pnFLAG-hTERT plasmid, 1µM CR4/5 and 0.3-1µM U42 PK fragments were added. hTERT K78E mutant plasmid was Reactions were incubated at 30oC for 3 hours, followed by addition of 5 µL 0.5M EDTA and 30 minutes of incubation at room temperature.

Telomerase Purification

Each RRL reaction was combined with 60 µL of M2 anti-FLAG slurry (MilliporeSigma, USA) pre-blocked using blocking buffer (50 mM Tris-HCl pH 8.3, 3 mM MgCl2, 2 mM DTT, 500 µg mL-1 BSA, 50 µg mL-1 yeast tRNA) and incubated at 4ºC overnight with rotation. Beads were washed extensively, and FLAG-tagged hTERT was eluted from the beads using 60 µL of elution buffer (50 mM Tris-HCl pH 8.3, 3 mM MgCl2, 2 mM DTT, 750 µg mL-1 3X FLAG peptide, 20% glycerol). The mixture was incubated for 1.5 hrs at 4ºC after which beads were filtered using a 0.2 µm Nanosep filter (Pall Life Sciences Corp, USA). Eluent was aliquoted and snap frozen in N2 until further use.

Construct preparation for wild-type (WT) and mutant TPP1-POT1-TIN2

Residues 87-544 of TPP1 (UniProtKB: A0A590TQL1) and POT1 (UniProtKB: Q9NUX5) open reading frames (ORFs) were cloned into a single pFastBacDual expression vector (Invitrogen, Cat# 10712024), and ORF of His8-MBP-SUMO*-TIN2 (UniProtKB: Q9BSI4) was cloned into a pACEBac1 expression vector (Ghanim et al., 2019). NEBaseChanger was used to design mutagenesis primers for the TPP1 mutants (TPP1_E169K and TPP1_E215K). Mutants were prepared by NEB Q5 Site-Directed Mutagenesis Kit (NEB, Cat# E0554) using the wild type (WT) pFastBacDual_TPP1_POT1. Constructs were transformed into chemically-competent cells and grown at 37 °C overnight. The presence of the mutations was confirmed by DNA sequencing and plasmid stocks were generated using Invitrogen HiPure Plasmid Midiprep kit (Invitrogen, Cat# K210005). Recombinant baculoviruses were generated by Bac-to-Bac Baculovirus Expression System (Invitrogen, Cat# 10359016) using EmBacY cells (Geneva Biotech) (Trowitzsch et al., 2010).

Expression and purification of WT and mutant TPP1-POT1-TIN2

TPP1-POT1-TIN2 complex was expressed in S. frugiperda (Sf9) (Sf9, Oxford Expression Technologies Ltd, Cat# 600100) and purified as previously described in Sekne et al., 2022. Briefly, 4 liters of Sf9 cells were infected with recombinant baculoviruses expressing TPP1-

POT1 (WT or mutant TPP1) and TIN2. Cells were grown for 72 h at 27 °C before harvesting by centrifugation and washing with phosphate saline buffer (PBS). Pellets were snap frozen in liquid nitrogen, thawed in ice bath and then resuspended in lysis buffer (25 mM HEPES KOH pH 8.0, 300 mM NaCl, 1 mM MgCl 2, 0.01 mM ZnSO 4 , 0.01% IGEPAL CA-630, 1 mM PMSF, 1 mM DTT and 1x Complete protease inhibitor tablets (Roche, Cat# 11873580001)). Lysates were sonicated, clarified by ultracentrifugation and filtering through a 0.22 µm filter before applying to 25 ml of pre-equilibrated dextrin Sepharose resin (Cytiva, Cat# 28-9355-97). The resin was washed five times with 4 column volumes (CVs) of wash buffer (25 mM HEPES KOH pH 8.0, 300 mM NaCl, 1 mM MgCl2, 10 µM ZnSO4, 0.01% IGEPAL CA-630, 1 mM PMSF and 1 mM DTT) and once with 1 CV of 5 mM ATP and 4 mM MgCl2. Complexes were eluted from the resin by overnight incubation with SUMOstar protease (LifeSensors, Cat#SP4110) at 4 °C. Salt concentration of the sample was adjusted to 150 mM before application to a 5 ml HiTrap heparin HP column (Cytiva, Cat#17040701) pre-equilibrated in heparin buffer (50 mM Tris HCl pH 8.0, 150 mM NaCl, 1 mM MgCl2, 10 µM ZnSO4, 0.01% IGEPAL CA-630, 1 mM PMSF and 1 mM DTT). Sample was eluted over a linear gradient of 150 mM NaCl to 1,000 mM NaCl, concentrated and applied on a HiLoad 16/600 Superdex 200 column (Cytiva, Cat# 28-9893-35) in SEC buffer (25 mM HEPES NaOH pH 8.0, 300 mM NaCl, 1 mM MgCl 2 , 0.01 mM ZnSO 4 , 0.01% IGEPAL CA-630, 10%glycerol, 1 mM PMSF, 1 mM DTT). Peak fractions were pooled, concentrated to 0.3 mg ml -1 (WT), 0.4 mg ml -1 (TPP1_E169K) or 0.35 mg ml -1 (TPP1_E215K), and snap-frozen in liquid nitrogen for storage at -80°C.

POT1 Expression and purification

The open reading frame for His-MBP-3C-POT1 (residues 3-634) was cloned into pFastBac and recombinant Baculovirus was generated using the Bac-to-Bac Baculovirus Expression System and DH10Bac cells. 800 mL of sf9 cells at a density of 1x106 cells mL-1 were infected with 1% (v/v) of virus. Infected cells were incubated at 27ºC for 72 hours and harvested using centrifugation. Cell pellets were resuspended in lysis buffer (50 mM HEPES, pH 7.5, 300 mM

NaCl, 1 mM DTT, 1% NP-40, 1 mM PMSF,1X EDTA-free protease inhibitor (Roche, Cat. #4693159001). Cells were lysed by sonication and cleared by ultracentrifugation. Cleared lysate was applied to pre-equilibrated amylose resin and washed with three column volumes of wash buffer (50 mM HEPES, pH 7.5, 300 mM NaCl, 1 mM TCEP) before eluting protein with 10mM Maltose. Protein was concentrated using spin concentrators and PreScission protease was added. Cleavage reactions were incubated at 4ºC overnight before being buffer exchanged into anion-exchange buffer (50 mM HEPES, pH 7.5, 150 mM NaCl, 1 mM DTT). POT1 was applied to a HiTrap Q column (Cytiva, Cat. #17-1154-01) washed with three column volumes of anion-exchange buffer and eluted with a linear gradient to 660 mM NaCl using a high-salt buffer (1 M NaCl) over 10 CVs. Peak fractions were analyzed by SDS-PAGE, pooled and concentrated before being applied to a Superose 6 Increase 10/300 GL (Cytiva, Cat. # 29-0915-96) pre-equilibrated with storage buffer (50 mM HEPES pH 7.5, 300 mM NaCl, 1 mM TCEP). Peak fractions were analyzed by SDS-PAGE, pooled and concentrated to 1.4 mg ml-1 before being snap frozen in liquid N2.

Telomerase Pulldown Assay

Telomerase binding reactions were set up using 3 uL of purified human telomerase, 1 µL 5 nM DNA oligo (bio-5RCy5) and 1 µL TIB with either LiCl or KCl (50 mM Tris-HCl, pH 8.3, 10 mM Trolox, 50 mM LiCl/KCl, 1 mM MgCl2, 0.1 mg mL-1 BSA, 0.8% glucose). For TPT experiments, TPT-DNA binding reactions were set up at 50 nM DNA and 200 nM TPT, allowed to incubate for 30 minutes and diluted to 5 nM with TIB immediately prior to telomerase addition. DNA-telomerase complexes were incubated at room temperature for at least ten minutes, diluted to 125 pM DNA and deposited on the slide surface. After incubating for ten minutes, channels were washed extensively with TIB supplemented with 1% gloxy. Experiments were performed in triplicates unless otherwise indicated.

smFRET Data Collection and Analysis

Donor and acceptor fluorescence were obtained as previously described. Briefly, Cy3 donor dyes on the deposited telomerase molecules were directly excited using a 532 nm laser; and fluorescence intensity data were obtained from twenty fields of view with an imaging integration time of 100 ms. Red intensity data was recorded in triplicates under direct red excitation at 637 nm. Fluorescence intensity data was analyzed using in-house MatLab scripts, and calculated FRET values were exported into Prism. In Prism, histograms (0.5 bin width) were produced from raw FRET values and exported into Excel. The number of Cy5 molecules under direct red excitation was determined using an in-house MatLab script and averaged across triplicates for each experiment. FRET values between 0.4 and 1 were counted as primer-bound telomerase, summed and normalized for number of Cy5 molecules on the slide surface.

Quartz Slide Preparation

Quartz Slides (G. Finkenbeiner, Inc., USA) were cleaned and PEGylated according to the following protocol (Chandradoss et al., 2014). The slides were manually washed using Alconox (Alconox Inc.) and sonicated in a 5% (w/v) Alconox solution for 15 minutes. Slides were rinsed with water before sonication in water for 5 minutes. Slides were again rinsed and sonicated in Acetone for 20 minutes, followed by a sonication in 1 M KOH for 20 minutes. Slides were rinsed extensively with water and placed in a DURAN staining dish (DWK Life Sciences, USA). Piranha solution was prepared by mixing 450 mL concentrated Sulfuric Acid and 150 mL (3:1 ratio) of 30% H2O2. Slides were treated with Piranha solution for 20 minutes, rinsed, and placed in methanol. Silanizing solution was prepared by mixing 100 mL methanol, 5 mL Glacial Acetic Acid and 3 mL Aminosilane (N-[3-(Trimethoxysilyl)propyl]ethylenediamine). Slides were placed into the silanizing solution, sonicated for one minute and allowed to stand for 20 minutes. Slides were rinsed with methanol and dried with N2. Pegylation solution was prepared by mixing 200 mg mPEG-Succinimidyl Valerate (MW 5,000, Laysan Bio, Inc., USA) and ~2 mg Biotin-PEG-SVA MW 5,000 (Laysan Bio, Inc., USA) with 1 mL of 0.2 uM filtered 0.1 M NaHCO3. Solution was applied to the slide surface and fixed using a cover slip and incubated overnight at room temperature in a homemade moisture chamber. The next day, slides were rinsed, dried with N2 and vacuum sealed for storage at -20°C.

Preparation of 32P end-labeled DNA for primer extension assays and dot blots

γ-32P-labeled ATP was purchased commercially (Revvity Inc., USA). 50 μg of 32P-ATP were incubated with 50 pmol of DNA oligo in 1X PNK buffer (NEB) and 4000 units of T4 PNK ligase (NEB M0202M). Reactions were incubated at 37^{o}C for 2 hours and heat inactivated at 65oC for 20 minutes.

Dot Blot Assay

0.5, 1 and 5 uL reconstituted enzyme were mixed with 2X Formamide loading buffer to 10uL 1X and heated to 70^{o}C for 5 minutes before being placed on ice. Solutions were deposited onto Hybond N+ membrane and allowed to dry. RNA was crosslinked to the membrane using UV transillumination. Membrane was incubated in Church buffer (1% BSA, 1 mM EDTA, 500mM Na2HPO4 pH 7.2, 7% SDS) at 55^{o}C for 30 minutes for pre-hybridization. Radiolabeled oligo probe (5'-CGG TGG AAG GCG GCA GGC CGA GGC-3') at about 5000 cpm was added and left to incubate at 55^{o}C overnight. The membrane was washed three times ten minutes in 0.1SSC/0.1% SDS. Radioactivity was visualized using a phosphorimager and Typhoon scanner. RNA amounts were determined using a standard curve.

Telomerase Activity Assays

Reactions were set up using 1 nmol of reconstituted enzyme, 50 nM end-labeled 5R primer, 10 mM dNTPs in 1X TB (50 mM Tris·HCl, pH 8.3, 50 mM KCl, 3 mM MgCl2, 2 mM DTT) as described previously. Where indicated, TPT (WT, E169K or E215K) were added to the reaction mixture to a final concentration of 200 nM. Reactions were incubated at 37C for 3 hours, quenched with 200 uL of 1X TES buffer (50mM Tris-HCl, 1mM EDTA, 0.1% SDS) and phenol-chloroform extracted, and ethanol precipitated overnight. DNA products were resolved on a

12% Urea-PAGE gel and bands were visualized using a phosphorimager and Typhoon scanner.

REFERENCES

1. Makarov, V. L., Hirose, Y. & Langmore, J. P. Long G tails at both ends of human chromosomes suggest a C strand degradation mechanism for telomere shortening. Cell 88, 657–666 (1997).
2. Pfeiffer, V. & Lingner, J. Replication of Telomeres and the Regulation of Telomerase. Cold Spring Harb. Perspect. Biol. 5, a010405 (2013).
3. Lansdorp, P. M. et al. Heterogeneity in telomere length of human chromosomes. Hum. Mol. Genet. 5, 685–691 (1996).
4. de Lange, T. Shelterin: the protein complex that shapes and safeguards human telomeres. Genes Dev. 19, 2100–2110 (2005).
5. Veldman, T., Etheridge, K. T. & Counter, C. M. Loss of hPot1 function leads to telomere instability and a cut-like phenotype. Curr. Biol. CB 14, 2264–2270 (2004).
6. Pinzaru, A. M. et al. Telomere Replication Stress Induced by POT1 Inactivation Accelerates Tumorigenesis. Cell Rep. 15, 2170–2184 (2016).
7. Harley, C. B., Futcher, A. B. & Greider, C. W. Telomeres shorten during ageing of human fibroblasts. Nature 345, 458–460 (1990).
8. Muraki, K., Nyhan, K., Han, L. & Murnane, J. P. Mechanisms of telomere loss and their consequences for chromosome instability. Front. Oncol. 2, 135 (2012).
9. Autexier, C. & Lue, N. F. The structure and function of telomerase reverse transcriptase. Annu. Rev. Biochem. 75, 493–517 (2006).
10. Collins, K. The biogenesis and regulation of telomerase holoenzymes. Nat. Rev. Mol. Cell Biol. 7, 484–494 (2006).
11. Blackburn, E. H. & Collins, K. Telomerase: An RNP Enzyme Synthesizes DNA. Cold Spring Harb. Perspect. Biol. 3, a003558 (2011).
12. Greider, C. W. Telomerase is processive. Mol. Cell. Biol. 11, 4572–4580 (1991).
13. Garcia, C. K., Wright, W. E. & Shay, J. W. Human diseases of telomerase dysfunction: insights into tissue aging. Nucleic Acids Res. 35, 7406–7416 (2007).
14. Bordeira Gaspar, T. et al. Telomere Maintenance Mechanisms in Cancer. Genes 9, 241 (2018).
15. Nandakumar J, Bell CF, Weidenfeld I, Zaug AJ, Leinwand LA, Cech TR. The TEL patch of telomere protein TPP1 mediates telomerase recruitment and processivity. *Nature*. 2012;492(7428):285-289. doi:10.1038/nature11648

16. Frank, A. K. et al. The Shelterin TIN2 Subunit Mediates Recruitment of Telomerase to Telomeres. PLOS Genet. 11, e1005410 (2015).

17. Colgin, L. M., Baran, K., Baumann, P., Cech, T. R. & Reddel, R. R. Human POT1 Facilitates Telomere Elongation by Telomerase. Curr. Biol. 13, 942–946 (2003).

18. Tesmer, V. M., Brenner, K. A. & Nandakumar, J. Human POT1 protects the telomeric ds-ss DNA junction by capping the 5' end of the chromosome. Science 381, 771–778 (2023).

19. Schmidt, J. C., Zaug, A. J. & Cech, T. R. Live Cell Imaging Reveals the Dynamics of Telomerase Recruitment to Telomeres. Cell 166, 1188-1197.e9 (2016).

20. Pike, A. M., Strong, M. A., Ouyang, J. P. T. & Greider, C. W. TIN2 Functions with TPP1/POT1 To Stimulate Telomerase Processivity. Mol. Cell. Biol. 39, e00593-18 (2019).

21. Sekne, Z., Ghanim, G. E., van Roon, A.-M. M. & Nguyen, T. H. D. Structural basis of human telomerase recruitment by TPP1-POT1. Science 375, 1173–1176 (2022).

22. Henderson, E., Hardin, C. C., Walk, S. K., Tinoco, I. & Blackburn, E. H. Telomeric DNA oligonucleotides form novel intramolecular structures containing guanine-guanine base pairs. Cell 51, 899–908 (1987).

23. Ambrus, A. et al. Human telomeric sequence forms a hybrid-type intramolecular G-quadruplex structure with mixed parallel/antiparallel strands in potassium solution. Nucleic Acids Res. 34, 2723–2735 (2006).
24. Zahler, A. M., Williamson, J. R., Cech, T. R. & Prescott, D. M. Inhibition of telomerase by G-quartet DNA structures. Nature 350, 718–720 (1991).
25. Jansson, L. I. et al. Telomere DNA G-quadruplex folding within actively extending human telomerase. Proc. Natl. Acad. Sci. 116, 9350–9359 (2019).

26. Hwang, H., Buncher, N., Opresko, P. L. & Myong, S. POT1-TPP1 regulates telomeric overhang structural dynamics. Struct. Lond. Engl. 20, 1872–1880 (2012).

27. Rice C, Shastrula PK, Kossenkov AV, et al. Structural and functional analysis of the human POT1-TPP1 telomeric complex. Nat Commun. 2017;8:14928. Published 2017 Apr 10. doi:10.1038/ncomms14928

28. Sen, D. & Gilbert, W. A sodium-potassium switch in the formation of four-stranded G4-DNA. Nature 344, 410–414 (1990).

29. del Villar-Guerra, R., Trent, J. O. & Chaires, J. B. G-quadruplex secondary structure from circular dichroism spectroscopy. Angew. Chem. Int. Ed Engl. 57, 7171–7175 (2018).

30. Loayza, D., Parsons, H., Donigian, J., Hoke, K. & de Lange, T. DNA binding features of human POT1: a nonamer 5'-TAGGGTTAG-3' minimal binding site, sequence

specificity, and internal binding to multimeric sites. J. Biol. Chem. 279, 13241–13248 (2004).

31. Rice, C. et al. Structural and functional analysis of the human POT1-TPP1 telomeric complex. Nat. Commun. 8, 14928 (2017).

32. Lei, M., Podell, E. R. & Cech, T. R. Structure of human POT1 bound to telomeric single-stranded DNA provides a model for chromosome end-protection. Nat. Struct. Mol. Biol. 11, 1223–1229 (2004).

33. Hwang, H. et al. Telomeric Overhang Length Determines Structural Dynamics and Accessibility to Telomerase and ALT-Associated Proteins. Structure 22, 842–853 (2014).

34. Parks, J. W. & Stone, M. D. Coordinated DNA dynamics during the human telomerase catalytic cycle. Nat. Commun. 5, 4146 (2014).

35. Ghanim, G. E. et al. Structure of human telomerase holoenzyme with bound telomeric DNA. Nature 593, 449–453 (2021).

36. Schmidt, J. C., Dalby, A. B. & Cech, T. R. Identification of human TERT elements necessary for telomerase recruitment to telomeres. eLife 3, e03563 (2014).

37. Nandakumar, J. et al. The TEL patch of telomere protein TPP1 mediates telomerase recruitment and processivity. Nature 492, 285–289 (2012).

38. Taylor, D. J., Podell, E. R., Taatjes, D. J. & Cech, T. R. Multiple POT1–TPP1 Proteins Coat and Compact Long Telomeric Single-Stranded DNA. J. Mol. Biol. 410, 10–17 (2011).

39. Tree, D. R., Muralidhar, A., Doyle, P. S. & Dorfman, K. D. Is DNA a Good Model Polymer? Macromolecules 46, 10.1021/ma401507f (2013).

40. Loayza, D., Parsons, H., Donigian, J., Hoke, K. & de Lange, T. DNA binding features of human POT1: a nonamer 5’-TAGGGTTAG-3’ minimal binding site, sequence specificity, and internal binding to multimeric sites. J. Biol. Chem. 279, 13241–13248 (2004).

41. Cerofolini, L. et al. G-triplex structure and formation propensity. Nucleic Acids Res. 42, 13393–13404 (2014).

42. Jiang, H.-X. et al. Divalent cations and molecular crowding buffers stabilize G-triplex at physiologically relevant temperatures. Sci. Rep. 5, 9255 (2015).

43. Gu, P. et al. Distinct functions of POT1 proteins contribute to the regulation of telomerase recruitment to telomeres. Nat. Commun. 12, 5514 (2021).

44. Hwang, H., Buncher, N., Opresko, P. L. & Myong, S. POT1-TPP1 regulates telomeric overhang structural dynamics. Struct. Lond. Engl. 20, 1872–1880 (2012).

45. Mullins, M. R. et al. POT1–TPP1 Binding and Unfolding of Telomere DNA Discriminates against Structural Polymorphism. J. Mol. Biol. 428, 2695–2708 (2016).

46. Schmidt, J. C., Zaug, A. J. & Cech, T. R. Live Cell Imaging Reveals the Dynamics of Telomerase Recruitment to Telomeres. Cell 166, 1188-1197.e9 (2016).

47. Zaug, A. J., Podell, E. R. & Cech, T. R. Human POT1 disrupts telomeric G-quadruplexes allowing telomerase extension in vitro. Proc. Natl. Acad. Sci. U. S. A. 102, 10864–10869 (2005).

Supplementary Information

Table 1 – Oligo Table

Five-Repeat Telomere Primer (5R)	BiotinTGGCGACGGCAGCGAGGCTTTAGGGTTAGGGTTAGGGTTAGGG/iAmMC6T/TAGGG
Double-Labeled 5R	BiotinTGGCGACGGCAGCG**/**iAmMC6T**/**GGCTTTAGGGTTAGGGTTAGGGTTAGGG/iAmMC6T/TAGGG
Activity Assay Primer	TGGCGACGGCAGCGAGGCTTTAGGGTTAGGGTTAGGGTTAGGGTTAGGG
Mut3R POT1 EMSA Primer	TTTGGCTTAGGG/iAmMC6T/TAGGG
hTR-t/PK RNA fragment (32-62)	GGGCCAUUUU(5NU)UGUCUAACCCUAACUGAGAA
DNA splint	CAGCGCGCGGGGAGCAAAAGCACGGCGCCTACGCCCTTCTCAGTTAGGGTTAGACAAAAAATGGCCACCA CCCCTCCCAGG
Dot Blot Probe Primer	CGGTGGAAGGCGGCAGGCCGAGGC
IVT template T7 hTR 32 forward	TAATACGACTCACTATAGGGCCATTTTTTGTCTAACCC
IVT template hTR 195 reverse	AACGGGCCAGCAGCTGAC
IVT template T7 hTR 239 forward	TAATACGACTCACTATAGAACCCCGCCTGG
IVT template T7 hTR 328 reverse	GACCCGCGGCTGACAGAG
IVT template T7 hTR 63 forward	TAATACGACTCACTATAGGGCGTAGGCGCCGTG
pFastBacDual TPP1-E215K-POT1 forward	GCTGCCCACGAAACAGCCCCGGC
pFastBacDual TPP1-E215K-POT1 reverse	AGGCTGAAGCGGTCCACCTGG
pFastBacDual TPP1-E169K-POT1 forward	GGACTGGGAGAAAAAGGAGTTCG
pFastBacDual TPP1-E169K-POT1 reverse	GAGGTGTCCAGGGCC

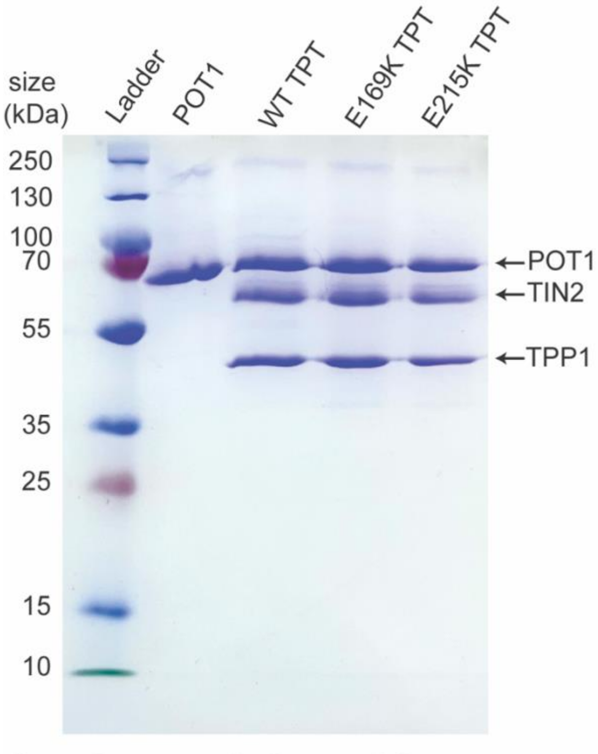

Supplemental Figure S1. SDS-PAGE Gel of purified protein complexes. The gel was prepared using 12% 37.5:1 Acrylamide:Bisacrylamide and proteins were visualized using Coomassie Blue stain. Samples were run against a PageRuler prestained protein ladder (Thermo Scientific).

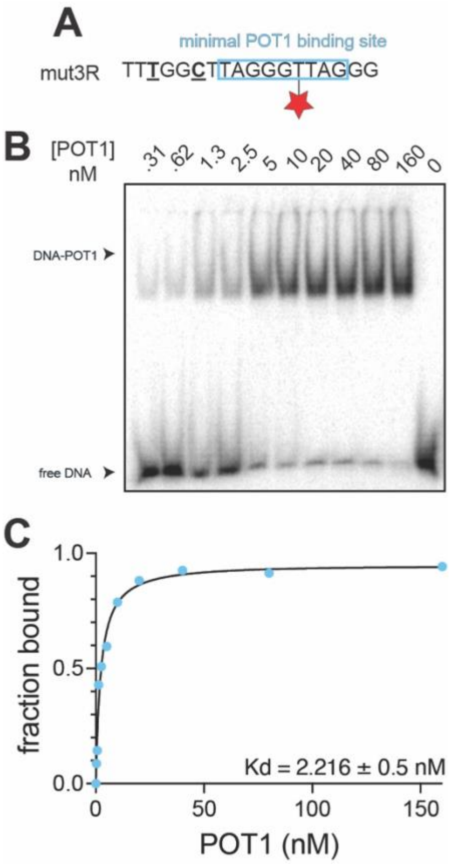

Supplemental Figure S2. Electromobility shift assay analysis of POT1 binding a Cy5-labeled primer. A. The primer was designed to bind the equivalent Cy5-labeled position as in 5R. Two mutations in the 5’ region of the primer (bold and underlined) ensure that POT1 must bind the single available binding site (blue box), which contains the Cy5-modified nucleotide. **B.** Increasing concentrations of POT1 were added to 1 nM DNA. Free DNA was separated from DNA-POT1 complexes on a 4% native PAGE gel. Bands were visualized using a Typhoon scan for Cy5 intensity. **C.** Analysis of the EMSA data reveals a Kd of 2.216 ± 0.5nM.

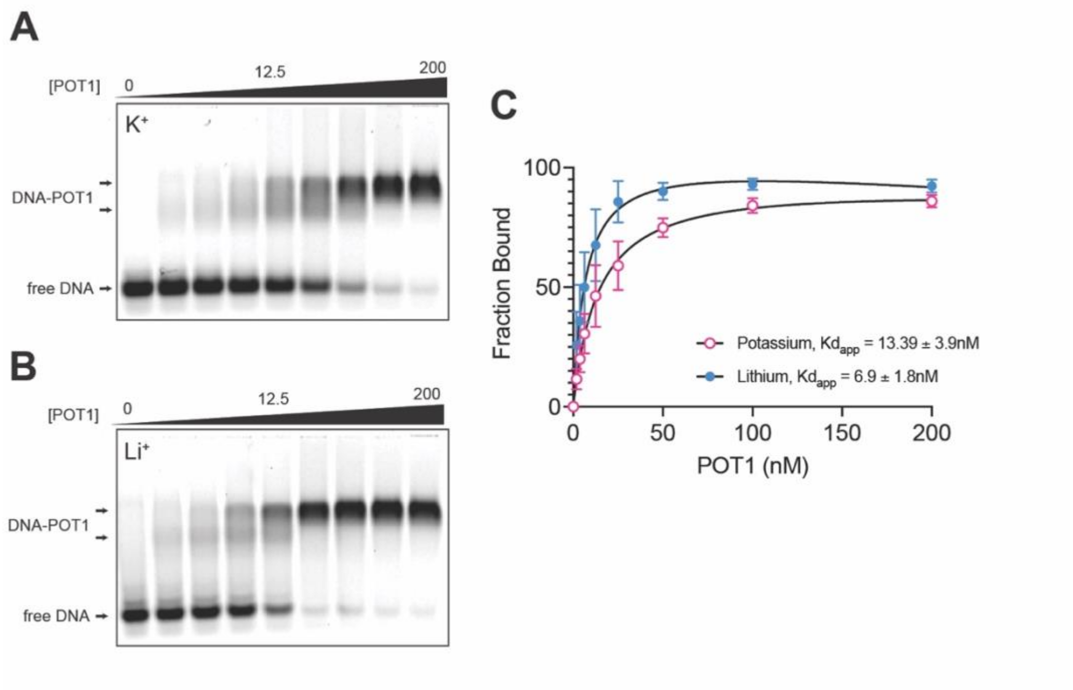

Supplemental Figure S3. Electromobility shift assay analysis of POT1 binding the model telomere oligo 5R. Assays were performed in either potassium (**A**) or lithium (**B**) salt conditions. The DNA concentration was held constant at 5nM and POT1 concentrations ranged from 1.5 to 200nM. Band intensities were visualized by a Typhoon scan of the Cy5 dye on the DNA oligo. In both ion conditions, a low molecular weight band at low POT1 concentrations shifts to a higher molecular weight band at higher POT1 concentrations, indicative of two POT1 molecules binding to 5R. **C.** Analysis of the EMSA data revealed an apparent Kd of 13.9 ± 3.9 nM in potassium and 6.9 ± 1.8 nM in lithium conditions. A higher apparent Kd in potassium is consistent with the need of POT1 to unfold G-quadruplex structures prior to DNA binding.

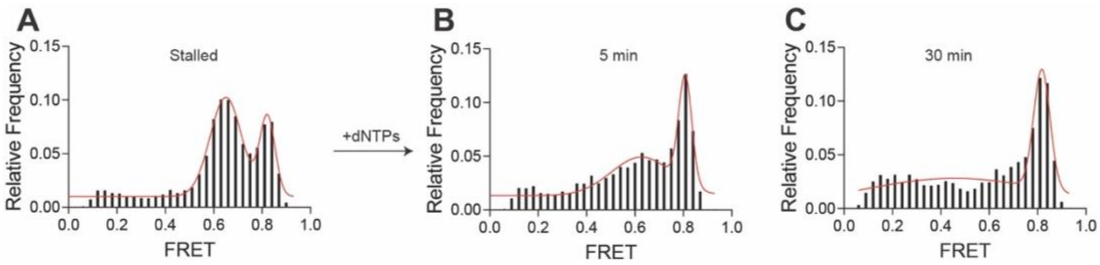

Supplemental Figure S4. FRET behavior of LD555-labeled Telomerase on 5R upon dNTP addition. A. Stalled telomerase-DNA complexes result in two high-FRET peaks at ~0.65 and 0.8. **B.** Five minutes after 10mM dNTP addition, which induces telomerase-catalyzed DNA synthesis, the relative frequency of the ~0.65 FRET peak decreases while the ~0.8 FRET peak remains unchanged This indicates an increased distance between the Cy5-labeled model telomere and the active site of the ~0.65 FRET population, but not of the ~0.8 FRET population. **C.** 30 minutes after dNTP addition, the ~0.6 FRET population has almost disappeared, while the ~0.8 FRET population remains, indicating that the 0.8 FRET population is unable to catalyze the addition of nucleotides to the model telomere substrate.

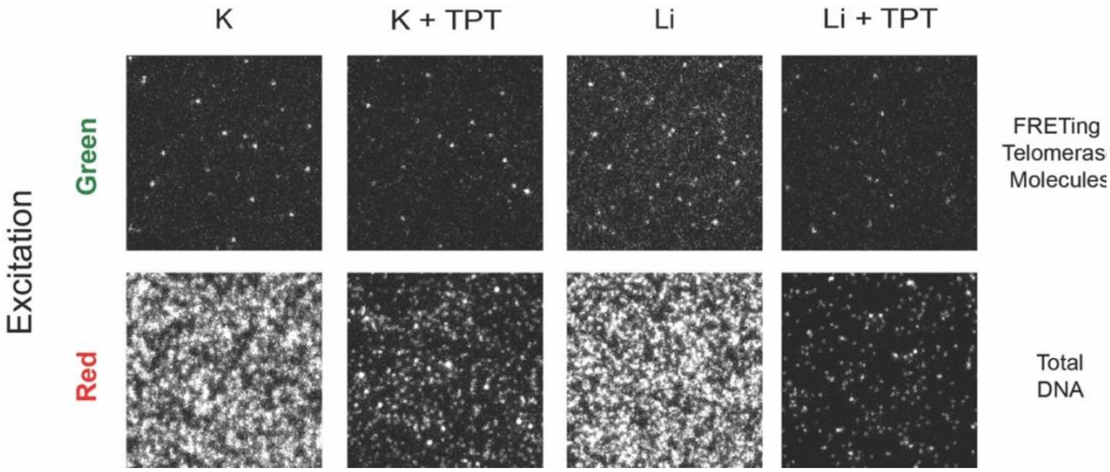

Supplemental Figure S5. Comparison of FRET events and DNA density in telomerase pulldown conditions. The top panel shows a small field of view of FRET events detected in the red channel under green excitation in each pulldown condition (top panel). This is compared to the same field of view under direct red excitation (bottom panel), which visualizes the total DNA deposited on the slide surface. This comparison illustrates the need for normalization of total FRET events in each condition and experimental replicate against its corresponding DNA density.

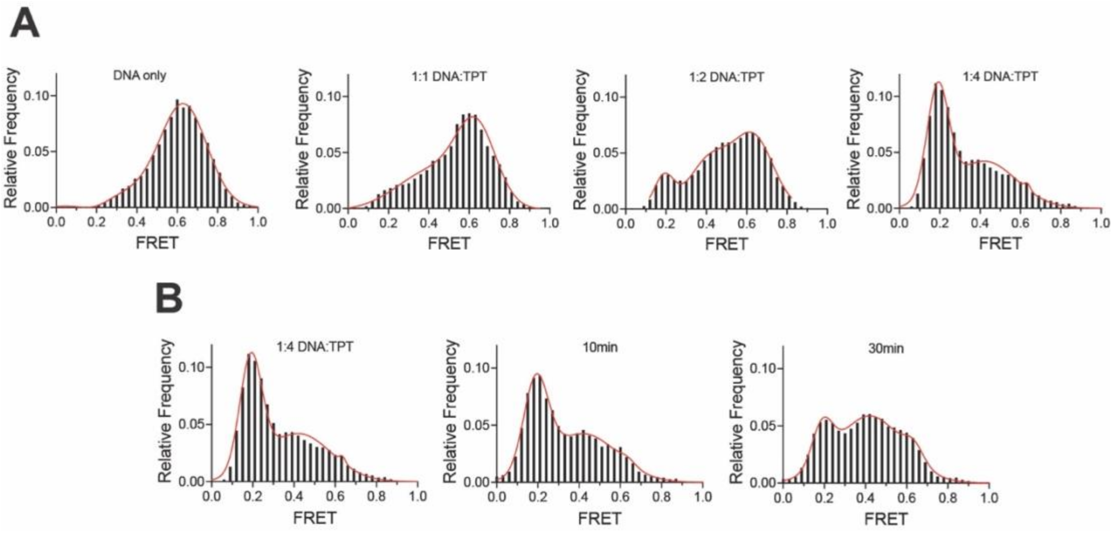

Supplemental Figure S6. Determination of DNA:TPT stoichiometry needed for DNA saturation and analysis of DNA-TPT stability. A. Unbound 5R in potassium containing buffer results in a high FRET population at ~0.65 (left). Incubation of 50nM 5R DNA and 50nM TPT results in the appearance of a minor low FRET peak at ~0.2 and resolution of a mid-FRET peak at ~0.4, however the majority of the ~0.65 FRET peak remains. A 1:2 stoichiometric incubation of DNA and TPT results in a further increase in the relative frequency of the low-mid FRET populations at ~0.2 and ~0.4, while the high FRET population indicative of unbound 5R remains moderately high. Incubating 50nM 5R DNA with 200nM TPT, a concentration well above the apparent Kd of 19.1 ± 3.9, results in a major shift of the high- and mid- FRET populations at ~0.65 and ~0.4 to a major low FRET population at ~0.2 (right). **B.** To ensure that telomerase encounters a DNA-TPT complex in our pulldown experiments, we analyzed the dissociation of TPT from DNA in a mock-telomerase incubation where 50 nM DNA was prebound with 200nM TPT (left) and then diluted to 1nM DNA. Ten minutes after dilution, there is a slight decrease in the low FRET population, indicating the majority of TPT-DNA complexes remaining intact (middle). After 30 minutes, the low FRET population has decreased to the same relative frequency as the high and mid FRET peaks, indicating that a significant amount of TPT has dissociated from the DNA, allowing it to reform DNA structure (right).

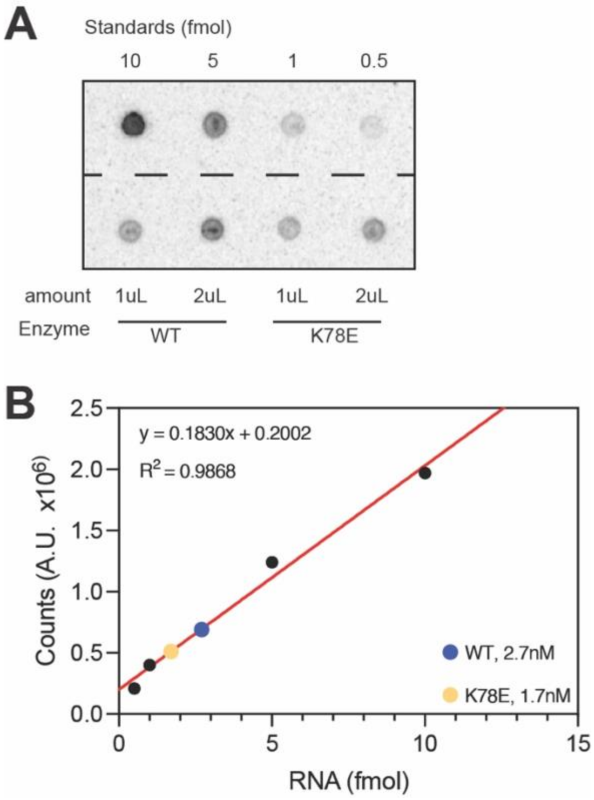

Supplemental Figure S7. Determination of telomerase concentration via dot blot analysis. A. Dot blot analysis was performed on 1 and 2 uL of each, WT and K78E LD555-labeled telomerase enzyme (bottom row). Samples were processed along known amounts of CR4/5 RNA (top row) for the purpose of a standard curve. A radiolabeled probe against the hTR CR4/5 domain was used to detect assembled enzyme. **B.** A standard curve created from the known amounts of CR4/5 RNA reveals enzyme concentrations of 2.7 nM for the wildtype enzyme (blue dot) and 1.7 nM for the K78E enzyme (yellow dot).

CHAPTER 4: 6-thio-2'-deoxyguanosine drives telomere shortening by impairing telomerase translocation after nucleotide addition

Abstract

Telomerase is a ribonucleoprotein that maintains telomere length in highly proliferative cells and thus ensures their proliferative potential. Normal human somatic tissues do not express telomerase. However, telomerase is reactivated in about 90% of human cancers. Thus, specifically targeting telomerase presents itself as a less harmful alternative to current cytotoxic chemotherapy treatments. A nucleoside analog of dGTP, 6-thio-dGT, has shown promising potential as an effective treatment of cancerous cell lines. Treatment of several cancerous cell lines with a precursor of the compound have shown decreased cell viability and telomere damage in those cells. However, the mechanism by which 6-thio-dGTP incorporation into telomeres inhibits telomerase activity and induces telomere dysfunction is unknown. Here, we use a combination of biochemical and biophysical approaches to study the effect of 6-thio-dGTP incorporation into telomere DNA on telomerase activity. Our findings show that incorporation of 6-thio-dGTP into nascent telomere DNA inhibits telomerase by preventing template translocation and thereby stalling telomerase on the ssDNA substrate.

Introduction

Telomeres are protective DNA caps at the end of eukaryotic chromosomes. They are essential for the maintenance of genomic integrity and proliferative potential in eukaryotic cells. Mammalian telomeres are comprised of 9-15 kilobase pairs of the hexameric DNA repeat GGTTAG that terminates in a 3' single stranded DNA end and are bound by the shelterin protein complex.[1] Shelterin is a telomere specific six-protein complex that binds telomere DNA throughout the cell cycle.[2] This prevents the linear ends of chromosomes from being recognized as DNA breaks by cellular DNA repair mechanisms. Due to the end-replication problem, telomeres shorten with each cell cycle which can compromise their protective potential .[3,4,5] Critically short telomeres result in senescence or apoptosis.[6] To retain their proliferative potential, telomere length in healthy and highly proliferative cells, such as bone marrow cells, is maintained by the ribonucleoprotein telomerase. Most normal somatic tissues in humans do not display telomerase activity. However, telomerase activity is aberrantly activated in about 90% of cancer cells and thereby confers immortality in these cells.[7] Telomerase is minimally composed of the protein component telomerase reverse transcriptase (hTERT in humans) and the telomerase RNA (hTR in humans) component. Telomerase maintains telomere length by using its internal RNA template to add hexameric GGTTAG repeats to the 3’ end of each telomere.[8] After each round of repeat addition, the enzyme rearranges its RNA template to processively add DNA repeats in a process called repeat addition processivity (RAP) (Fig. 1). This feature is unique to telomerase and therefore presents itself as an attractive target for novel anti-cancer agents.

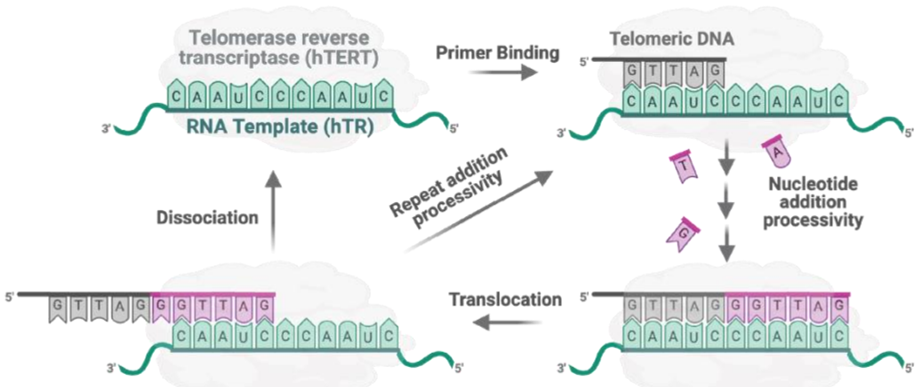

Figure 1. The catalytic cycle of human telomerase. Telomerase uses its internal RNA template to bind telomeric DNA. Nucleotide addition occurs via nucleotide addition processivity (NAP). After one telomere repeat has been added, the template boundary is reached. telomerase has to then translocate the RNA template for continued DNA synthesis, a step prone to DNA dissociation. The requirement for template translocation results in a process called repeat addition processivity.

Telomerase has been the target of anti-cancer drugs since its role in the immortalization of cancerous cells has been discovered. Targeting telomerase activity specifically could lower the toxicity of anti-cancer treatment and thus the negative effect of current chemotherapies on healthy tissues. On June 26, 2024, the US Food and Drug administration approved the first telomerase-targeting anticancer drug. In a historic moment, the drug imetelstat (Rytelo, Geron Corporation) was approved for use in human adults with low- to intermediate-1 risk myelodysplastic syndromes, a group of cancers that prohibit maturation of blood cells in patients.[9,10] Imetelstat is an oligonucleotide therapeutic that inhibits telomerase activity by base-pairing with the template region of human hTR. This outcompetes telomerase binding to its DNA substrate to prevent telomerase activity, leading to shortening telomeres in treated cells. However, a lack of detectable telomere shortening in animals and humans raised questions about the effectiveness of Imetelstat as a telomerase inhibitor *in vivo.*[11,12] In addition, treatment of other kinds of cancer with telomerase-targeting drugs remains unavailable/ The unique catalytic properties of telomerase led to the search for nucleotide analogs that could selectively inhibit telomerase and halt telomere elongation in cancer cells.

To reduce potential toxicity, the Shay lab recently tested 6-thio-dG, a prodrug that, once metabolized to 6-thio-dGTP (6tdGTP), can be preferentially incorporated into telomeres by telomerase. They found that 6-thio-dG treatment caused telomere shortening in cancer cells and was less toxic to telomerase deficient, normal cells.[13] In preclinical studies, 6-thio-dG could overcome chemotherapy resistance and induce telomere dysfunction in melanoma, lung, and pediatric brain cancer tumor xenografts in mice. In addition, these cells exhibit telomere dysfunction as observed by gamma-H2AX presence at telomeres after treatment. Importantly, healthy cell lines were largely unaffected by treatment with 6-thio-dG. However, the mechanism of inhibition by 6tdGTP is unknown.

Primer extension assays previously performed by our collaborators, the Opresko lab at University of Pittsburgh, have shown that telomerase inhibition is not due to a chain-terminating effect by 6-thio-dGTP and that it is independent of primer sequence.[14,15] In addition, they found that the catalytic efficiencies of dGTP and 6tdGTP were similar. Finally, they showed that incorporation of 6tdGTP halts DNA synthesis by telomerase by negatively affecting template translocation. However, this conclusion does not reveal the exact mechanism by which template translocation is impaired. For instance, it is possible that 6tdGTP prevents formation of a stable DNA-RNA primer, causing the enzyme to dissociate from the primer. Another hypothesis is that 6tdGTP prevents telomerase activity by altering the position of the 3' end in the active site after template translocation.

This work is a collaborative effort between the Stone Research Group and the Opresko Lab. Here, the Opresko lab conducts primer extension, electromobility shift and C-trap assays (Figures 2 and 3) to investigate the mechanism by which 6tdGTP incorporation results in telomerase inhibition. Their bulk experiments show that telomerase can bind a primer containing 6tdGTP as efficient as wildtype primer and that 6tdGTP at the 3' position lowers telomerase activity more than an internal 6tdGTP. This points away from DNA dissociation as a cause for 6tdGTP-mediated telomerase inhibition. To determine the mechanism by which 6tdGTP inhibits telomerase beyond DNA dissociation, we need to understand how 6tdGTP affects the DNA dynamics in the telomerase-DNA complex during activity. Therefore, we utilized a single-molecule FRET assay to probe the DNA dynamics that occur during telomerase activity using dGTP and 6tdGTP. Taken together, we are able to show incorporation of 6tdGTP results in a stalled telomerase-DNA complex that is unable to continue DNA synthesis.

Results

Opresko Lab: POT1 and TPP1 fail to rescue telomerase inhibition

We previously found that telomerase incorporation of 6tdGTP into telomere DNA strongly inhibits further extension after the first translocation step to add another repeat. This indicates that 6tdGTP presence inhibits specific step(s) in the catalytic cycle and prevents continued RAP.[15] The telomerase catalytic cycle begins when the telomeric ssDNA overhang base-pairs with the complementary 3' end of the 11-nucleotide telomerase RNA template (Fig. 2A), comprising a 5 nucleotide (nt) alignment region and 6nt templating bases.[16] After incorporation of an incoming dNTP (purple), the active site moves to position the next template base to insert the next dNTP. Telomere elongation continues to the 5’ template boundary; then telomerase can dissociate or translocate on the DNA product to realign the template for processive repeat addition.[17,18]

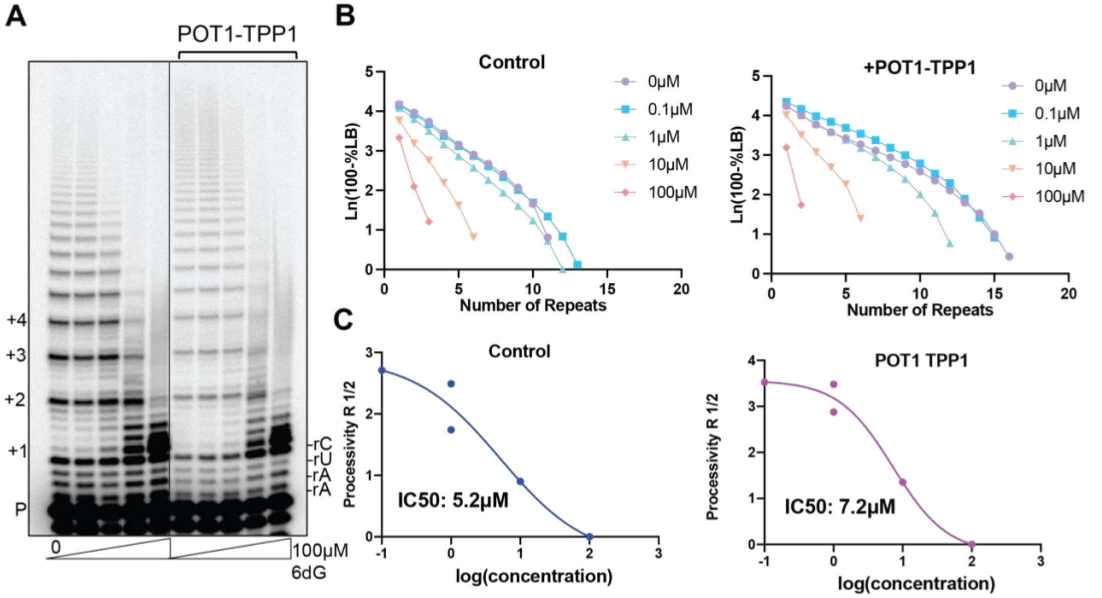

Figure 2. POT1-TPP1 fails to rescue telomerase activity with 6tdG. A. Direct telomerase assays were conducted in the absence or presence of 500 nM POT1 and 500 nM TPP1, as indicated, and 5 nM ^{32}P-end labeled primer (TTAGGGTTAGCGTTAGGG) designed to position POT1 at the 10 nt primer 5′ end. Reactions contained cellular-concentration dNTPs 0-100µM 6-thio-dGTP. Letters on the right indicate template base; P indicates unextended 18-mer primer. **B.** Processivity was calculated on the basis of total products normalized to loading control. **C.** IC50 values calculated from processivity R 1/2.

In biochemical studies, we previously determined that the telomerase RAP half-maximal inhibitory concentration IC_{50} for 6tdGTP is 5 μM; defined as the concentration required to reduce repeat processivity by half.[14] Since the shelterin dimer POT1-TPP1 is known to facilitate RAP, we asked if its presence on telomere DNA containing 6tdGTP alters the RAP IC50, and whether it can reduce 6tdGTP-mediated telomerase inhibition. To this end, we conducted primer extension assays in presence and absence of POT1-TPP1. To test the effect of 6tdGTP incorporation on activity in these assays, we added cellular relevant concentrations of natural dNTPs (5µM dGTP, 24µM dATP, 29µM dCTP, and 37µM dTTP) and titrated 6tdGTP from 0 to 100 µM.

In telomerase reactions without POT1-TPP1 (lanes 1-5) telomerase processivity is inversely related to 6tdGTP concentration, resulting in an IC_{50} value of 5.2µM, which is consistent with our previous result.[14] As expected, the reaction conducted with POT1-TPP1 but without 6tdGTP (lane 6) has higher processivity compared to the control (lane 1), indicating POT1-TPP1-mediated RAP stimulation. However, reactions with 6tdGTP and POT1-TPP1 (lanes 7-10) show strongly reduced telomerase processivity with an IC_{50} value of 7.2µM. This data indicates that POT1-TPP1 fails to reduce telomerase inhibition caused by 6-thio-dGTP.

Opresko Lab: Telomerase can bind to a substrate with 6-thio-dG

We next tested whether presence of a 3' 6tdGTP on the telomere DNA primer disrupts telomerase binding. For this, we conducted electrophoretic mobility shift assays (EMSAs) with 1-250nM active Halo-FLAG-tagged telomerase and 2.5nM fluorescently labeled DNA with and without 6-thio-dG at the 3' end of the telomeric sequence (Fig. 3A). Halo-FLAG-tagged telomerase conjugated photostable Janella fluorophores allows visualization of telomerase but does not impair telomerase activity. Our results show no significant difference in the binding affinity of telomerase for wildtype and 6tdGTP primer. Therefore, this data suggests that 6tdGTP presence at the end of a telomere does not disrupt telomerase binding. However, EMSA data cannot determine whether DNA-bound telomerase is primed for activity or, importantly, reveal

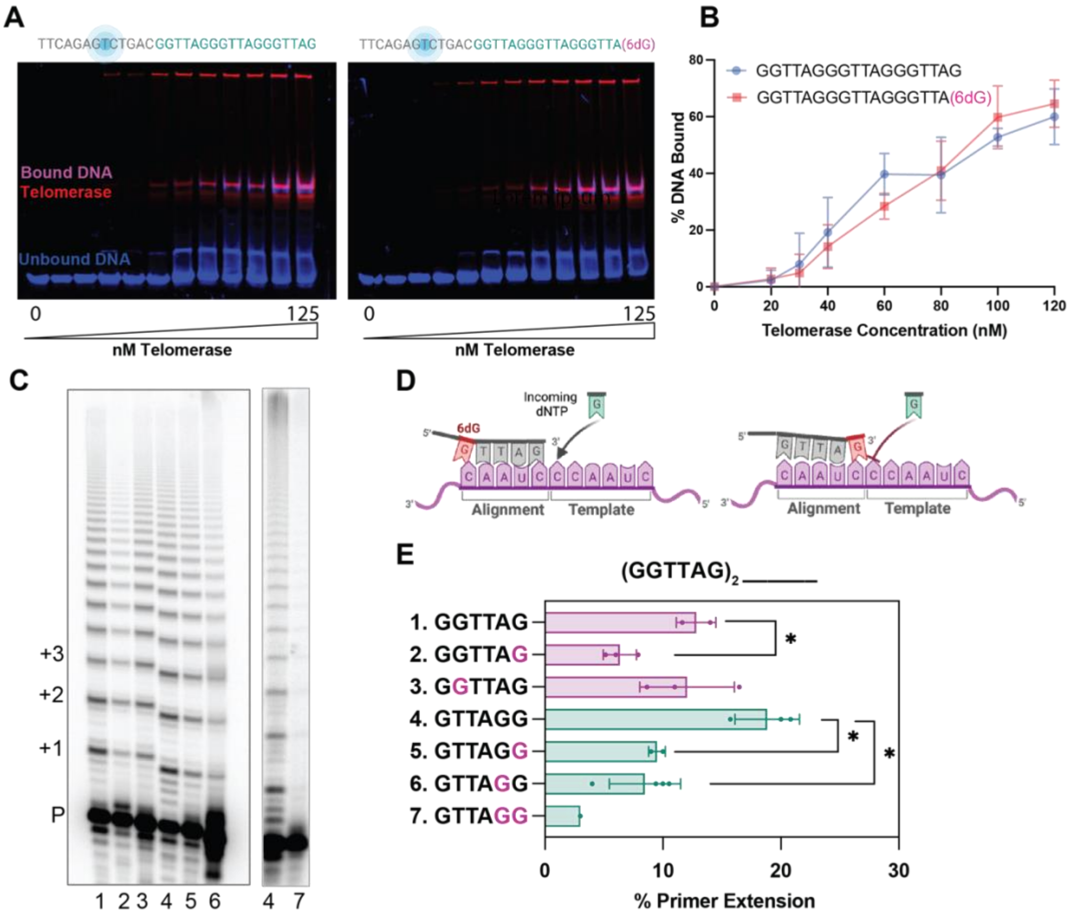

Figure 3. **Telomerase can bind DNA containing 6tdG. A.** EMSAs with 2.5nM unbound DNA (blue), 1-80nM Telomerase (red), and telomerase bound DNA (Pink). **B.** Graph representing % DNA bound to telomerase. **C.** Telomerase reactions conducted with 6-thio-dG at different positions of the substrate primer. P marks the unextended primer and numbers indicate the number of added repeats. **D.** Cartoons of telomeric primer (gray) with 6-thio-dG (red), telomerase RNA template (purple), and incoming dNTP (green). **E.** Quantitation of percent primer extension. *$p<0.05$, 2-tailed Student's T test. Sequence of telomeric primer shown on the Y axis. Magenta G's indicate 6-thio-dG modification.

the DNA dynamics that occur upon complex formation. Given that 6tdGTP presence does not affect binding of telomerase, it is possible that DNA-RNA dynamics that occur in the active site following 6tdGTP incorporation impair activity.

Opresko Lab: Pre-existing 6-thio-dG in the telomere impairs telomerase activity

We hypothesized that because binding of telomerase is unaffected by a terminal 6tdGTP on telomere DNA, 6tdGTP-induced dynamics of the RNA-DNA hybrid near the active site may disrupt telomerase activity. To test this, we designed a series of 18-mer telomeric ssDNA primers containing a pre-existing 6tdGTP base at different positions in the last five nucleotides (Fig. 3F, $(GGTTAG)_2$ followed by sequences 1-7). We conducted telomerase primer extension assays with 5'-radiolabeled primers and resolved the products by gel electrophoresis (Fig 3E). Each major band represents addition of one telomeric repeat. To compare telomerase activity in each condition, we extracted the total percent of primer extended for each. We found that as the 6tdGTP base is moved closer to the primer 3' end, telomerase inhibition is increased (Fig. 3E, compare lane 1 with 2, and lane 4 with 5 and 6). Since we previously found that telomerase can add two consecutive 6tdGTP, we also tested a primer with two 6tdGTP at the 3' end. Tandem terminal 6tdGTP almost completely abolished telomerase activity (compare lanes 4 and 7), which is consistent with the hypothesis that 6tdGTP presence alters DNA-RNA dynamics near the active site. Thus, the ability of 6tdGTP to inhibit telomerase activity by potentially impairing stable annealing with the template region and DNA coordination in the active site depends on its position in the primer.

Stone Lab: 6tdGTP incorporation prevents RNA-DNA dynamics required for telomerase activity

Our binding results are inconsistent with a model in which 6-thio-dG insertion inhibits RAP by impairing telomerase binding. However, the experiments conducted by the Opresko lab cannot reveal potential DNA-RNA dynamics in the telomerase complex prior to and during activity. Therefore, to examine how 6tdGTP impacts the dynamics between telomerase RNA and telomere DNA during catalysis, we used a single-molecule approach Förster Resonance Energy Transfer (FRET) assay that reports on the energy transfer of between a donor dye (LD555) on hTR (base U42) reconstituted with hTERT (Figure 4A) and an acceptor dye on the

DNA primer. This assay allows for the visualization of the distance between the two dyes, therefore allowing us to observe RNA-DNA dynamics during telomerase activity in real time. We first incubated telomerase with the primer before immobilizing complexes on a quartz slide via a biotin-streptavidin linkage. Telomerase stably bound to a primer result in a high FRET state of about 0.7 (Figure 4B, “stalled”). Upon addition of dNTPs, we see the expected shift in FRET values first to a mid-FRET at 5-15 minutes and eventually to a low FRET, indicating that telomerase is moving away from the acceptor dye on the DNA upon addition of nucleotides to nascent DNA (Fig 4B).[19,20] In contrast, addition of activity buffer containing and 6tdGTP to stalled complexes does not result in the expected drop in FRET, indicating inhibition of telomerase activity by 6tdGTP (Fig. 4C, middle). This suggests that 6tdGTP incorporation inhibits telomerase mediated dNTP addition, either by preventing appropriate coordination of the primer for nucleotide addition or by preventing template translocation.

To test that inhibition of telomerase activity is due to incorporation of 6tdGTP and not lack thereof, we performed a chase containing wildtype dNTPs. Our reasoning was that activity of telomerase, and thus a drop in FRET, would be restored upon addition of dNTPs if 6tdGTP was unable to be incorporated by the enzyme. Instead, a drop in FRET was not observed up to 30 minutes after addition of dNTPs, indicating that 6tdGTP incorporated into nascent DNA inhibits telomerase (Fig. 4C, right). This is consistent with results of primer extension assays previously performed by the Opresko lab.

To examine the dynamics of individual complexes during catalysis, we identified roughly one hundred single-molecule traces that exhibit the trademark anticorrelation of donor and acceptor dye intensities for each condition, and for stalled telomerase molecules not supplied with activity buffer. From each of these data sets, we synthesized a FRET heat map that summarizes the FRET behavior of all traces in a data set over time. As expected, the population not supplied with dNTPs had a stable high FRET behavior before dropping to a zero FRET state, indicative of acceptor dye bleaching (Fig. 4D, top panel). When supplied with wildtype dNTPs, complexes exhibited a reduction in FRET over time, eventually reaching a low

FRET value of 0.2, consistent with histogram data (Fig. 4D, middle panel). In contrast, complexes supplied with 6tdGTP instead of dGTP, complexes are stuck between a 0.4 and the initial high FRET value, indicating that DNA is no longer synthesized after an initial push in activity (Fig. 4D, bottom panel).

Further examination of FRET traces of individual telomerase-DNA complexes revealed a possible mechanism of telomerase inhibition by 6tdGTP. As observed in the heat map, complexes that were supplied with wildtype dNTPs exhibit a stepwise decrease in FRET behavior, from a high FRET of ~0.7 to a low FRET of ~0.2 (Fig. 4E, top). During this process, FRET values intermittently increase back from 0.4 to the initial high FRET value and from 0.2 to 0.4. This pattern has been identified previously using the same assay as indicative of DNA extension by telomerase.[19] Examining molecules supplied with activity buffer containing 6tdGTP, it is revealed that complexes jump between 0.4 and 0.6 FRET values. (Fig. 4E, bottom). Intermittently, complexes probe the 0.2 FRET state but cannot achieve a sustained low FRET state. In addition, we do not see an accelerated dissociation of telomerase from the DNA, which would be indicated by an accumulation of zero FRET states.

Instead, the population size of molecules that drop to a zero FRET state are comparable to those of stalled telomerase-DNA complexes and are likely caused by photobleaching of Cy5 dye. (Figure 4D, top panel).

Our results suggest that 6tdGTP incorporation stalls telomerase on the telomere DNA after an initial push in catalysis. Given that 6tdGTP is not a chain terminator of telomerase activity, it is likely that incorporation of two 6tdGTP affects DNA-RNA structure properties or DNA conformation in the active site, thereby preventing sustained telomerase activity.

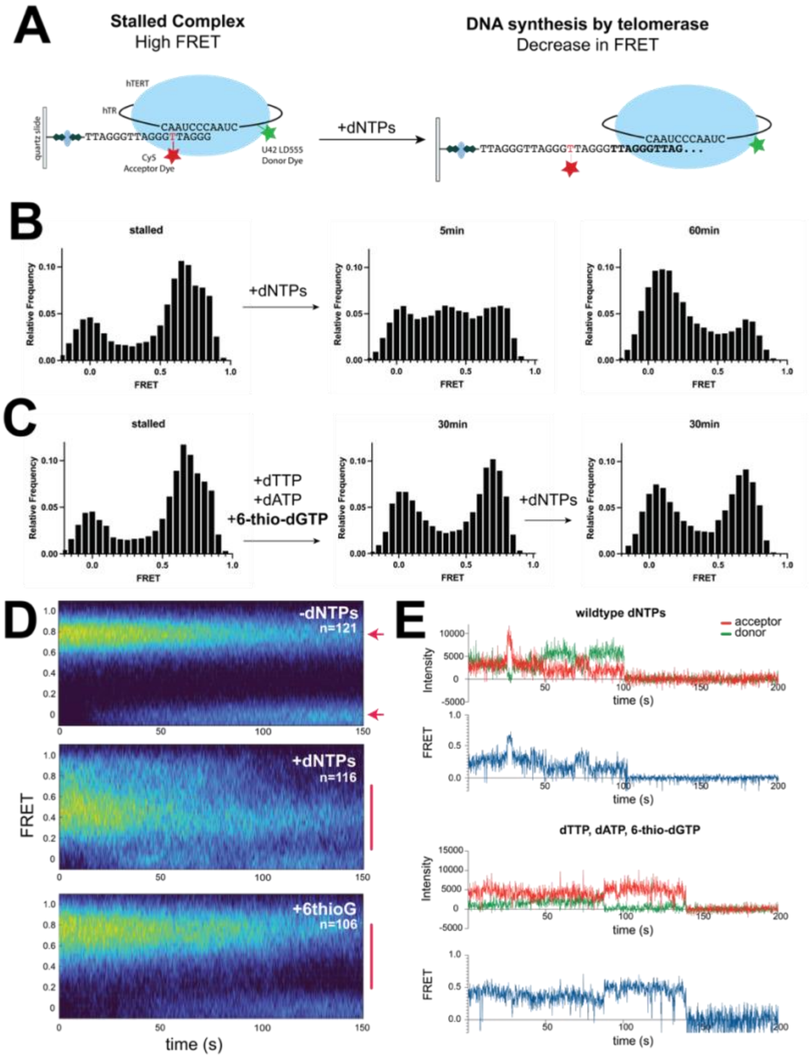

Figure 4. smFRET assay of telomerase activity in presence of 6tdG. A. Illustration of Experimental Setup. LD555-labeled telomerase is pulled down on Cy5-labeled (TTAGGG)3 primer and immobilized on a quartz slide via a 5’ biotin. This complex results in a stable high FRET state. Addition of activity buffer containing dNTPs results in telomerase activity leading to a drop in FRET due to telomerase moving down the ssDNA and away from the acceptor dye. **B.** Addition of dNTPs to stalled complexes results in a gradual shift from a high FRET value to a low FRET state, indicating movement of telomerase away from the acceptor dye and thus active ssDNA elongation. **C.** Addition of dATP, dTTP and 6-thio-dGTP to stalled complexes does not change the histogram, indicating that telomerase activity is limited. Addition of wildtype dNTPs does not rescue this behavior, indicating that incorporation of 6-thio-dGTP into the nascent ssDNA inhibits telomerase activity. **D.** Compiled analysis of FRET states of individual molecules over time. Arrows indicate an initial telomerase-DNA complex formation (top) and telomerase dissociation from the DNA primer (bottom). Addition of dNTPs to staled telomerase-DNA complexes results in a gradual decrease in FRET (middle panel) while addition of 6-thio-dGTP results in an initial drop in FRET that then remain constant over time (bottom panel). **E.** Example traces of single telomerase molecules during catalysis using wildtype dNTPs (top) or 6-thio-dGTP (bottom).

Discussion

Understanding the mechanism of telomerase inhibitors is key to the development of effective anti-cancer drugs. One promising compound that could be used for effective anti-cancer treatment is 6-thio-dG which gets metabolized to 6-thio-dGTP (6tdGTP) in the cell. In previous studies, 6tdGTP has been shown to effectively kill cancer cells by inhibiting telomerase activity. While prior work has established that 6tdGTP incorporation in the DNA primer is required for inhibition, the mechanism by which 6tdGTP inhibits telomerase activity is unknown. Here, we present evidence that incorporation of 6-thio-dGTP in telomere DNA inhibits telomerase activity by stalling the enzyme in a non-productive complex.

By *in vitro* primer extension assays, we show that POT1-TPP1 bound to DNA containing 6tdGTP is unable to rescue telomerase activity. POT1-TPP1 is known to stimulate repeat addition processivity (RAP) of telomerase by slowing DNA dissociation and increasing the efficiency of template translocation.[21] Therefore, if 6tdGTP increases the rate of DNA dissociation from the complex, POT1-TPP1 should be able to rescue this defect. In contrast, our results show that POT1-TPP1 is unable to rescue telomerase activity. This indicates that DNA template translocation occurs in the presence of 6tdGTP, but that the new DNA-RNA hybrid structure is perturbed by the presence of consecutive 6tdGTP at the 3' end, therefore preventing catalysis. Another possibility is that the contacts POT1-TPP1 makes with telomere DNA and telomerase are insufficient to overcome 6tdGTP induced primer dissociation. While POT1 binds telomere DNA with nanomolar affinity, the affinity of the DNA-POT1-TPP1 complex for telomerase is unknown.[22] Even though POT1-TPP1 can decrease the rate of DNA dissociation from the complex, our data indicates that this effect cannot overcome either DNA dissociation upon 6tdGTP incorporation. However, our results do not reveal whether the inhibitory effect of 6tdGTP is due to a lack of template translocation, primer dissociation or production of a nun-functional DNA: telomerase complex upon template translocation.

To further test the stability of the DNA-telomerase complex upon 6tdGTP addition, we performed electromobility shift assays with primer containing 6tdGTP. We show that telomerase can bind a primer that contains 6dG, which is in contrast to the hypothesis that the DNA: telomerase complex dissociates upon 6tdGTP incorporation. This result is consistent with previous primer extension assays that showed that 6tdGTP is not a chain terminator and that 6tdGTP leads to a stalled complex.[15] In addition, our C-trap results comparing telomerase binding either wildtype or 6tdGTP-containing DNA primer reveal no significant difference in binding time between the two primers. A lack of difference in telomerase binding stability of wildtype and 6tdGTP DNA primer indicates that the mechanism of inhibition is not by facilitating DNA destabilization. However, DNA-RNA dynamics that occur during RAP might promote 6tdGTP-containing primer dissociation to a higher degree than wildtype primer since sulfur cannot form hydrogen bonds as stably as oxygen.

We next asked how the position of 6tdGTP in the DNA primer affects telomerase activity. We argue that if 6tdGTP is destabilizing to the DNA: RNA hybrid, telomerase activity between different 6tdGTP positions of 6tdGTP should affect telomerase activity in varying ways. Our results show that 6tdGTP presence at the 3' end is more deleterious to telomerase activity than primer with an internal 6tdGTP. In addition, having two consecutive 6tdGTP further reduces telomerase activity compared to that of just one. Interestingly, telomerase exhibits similar activity levels if either of two dGs at the 3' end are 6tdGTP. Because 6tdGTP is not a chain terminator, these results indicate that presence of 6tdGTP near the 3' end destabilizes DNA: RNA hybrid formation at that location, which is supported by our smFRET data. This could negatively affect the positioning of the DNA: RNA hybrid in the active site and thereby prevent further dNTP addition. However, a dissociation of DNA from the complex due to DNA: RNA hybrid destabilization cannot be ruled out.

While our bulk biochemical assays were unable to distinguish between several possible modes of 6tdGTP induced telomerase inhibition, we took to single-molecule FRET to monitor the dynamics between the 3' DNA end and telomerase RNA that occur during telomerase activity. Our results show that upon addition of 6tdGTP to the reaction mix, the FRET value of a population of telomerase-DNA complexes remains unchanged, even after an extensive amount of time. This is in contrast to the same experiment conducted with wildtype dGTP, where addition of dNTPs to stalled DNA-telomerase complexes leads to a gradual reduction of FRET, therefore indicating extension of DNA as shown previously.[19,20] In addition, analysis of hundreds of individual FRET traces shows that 6tdGTP incorporation leads to a static FRET value of these complexes and no increase in zero FRET states. This shows that complexes are not dissociating from the DNA but rather getting “stuck” on the DNA primer. Together, these results show that telomerase inhibition by 6tdGTP incorporation is not due to increased dissociation of DNA from the enzyme, but due to the formation of a DNA-RNA hybrid that is not extendable by telomerase. Further experiments are required to determine the direct cause of this inhibition. We hypothesize that failure to make important contacts with the active site upon 6tdGTP incorporation leads to the inability to complete RAP.

Taken together, our study gives novel insight into the mechanism of telomerase inhibition by 6-thio-dGTP incorporation into a DNA primer. We show that incorporation of 6tdGTP at the 3’ proximal nucleotides is especially deleterious to telomerase activity *in vitro* and that this incorporation does not induce dissociation of the enzyme from the DNA.

Materials and Methods

Telomerase preparation

HEK-293T (ATCC) cells were grown to 90% confluency in Dulbecco's modified Eagle's medium (Gibco) supplemented with 10% FBS (Hyclone) and 1% penicillin-streptomycin (Corning) at 37°C and 5% CO_2. Cells were transfected with 10 µg of pSUPER-hTR plasmid and 2.5 µg of pVan107 hTERT plasmid diluted in 625 µl of Opti-MEM (Gibco) mixed with 25 µl of Lipofectamine 2000 (ThermoFisher) diluted in 625 µl of Opti-MEM. Cells expressing hTR and 3xFLAG-tagged human hTERT were harvested 48 hr post-transfection, trypsinized and washed with PBS, and then lysed in CHAPS buffer (10 mM Tris-HCl, 1 mM $MgCl_2$, 1 mM EDTA, 0.5% CHAPS, 10% glycerol, 5 mM β-mercaptoethanol, 120 U RNasin Plus (Promega), 1 µg/ml each of pepstatin, aprotinin, leupeptin and chymostatin, and 1 mM AEBSF) for 30 min at 4°C. 80µL of anti-FLAG M2 bead slurry (Sigma) (per T75 flask) was washed three times with 10 volumes of 1X human telomerase buffer (50 mM Tris-HCl, pH 8, 50 mM KCl, 1 mM MgCl2, 1 mM spermidine and 5 mM β-mercaptoethanol) in 30% glycerol and harvested by centrifugation for 1 min at 3500 rpm and 4ºC. The bead slurry was added to the cell lysate and nutated for 4-6 hours at 4ºC. The beads were harvested by 1 min centrifugation at 3500 rpm, and washed 3X with 1X human telomerase buffer with 30% glycerol. Telomerase was eluted from the beads with a 2x the bead volume of 250 µg/mL 3X FLAG® peptide (Sigma Aldrich) in 1X telomerase buffer containing 150 mM KCl. The bead slurry was nutated for 30 min at 4ºC. The eluted telomerase was collected using Mini Bio-Spin® Chromatography columns (Bio-Rad). Samples were flash-frozen and stored a -80ºC.

End-labelling of DNA primers

50 pmol of PAGE purified DNA oligonucleotides (IDT) (Table 1) were end labeled with $\gamma^{32}P$ ATP (Perkin Elmer) using T4 polynucleotide kinase (NEB) in 1X PNK Buffer (70mM Tris-HCl, pH 7.6, 10mM $MgCl_2$, 5mM DTT) in a 20 µl reaction volume. The reaction was incubated for 1

h at 37ºC followed by heat inactivation at 65ºC for 20 minutes. G-25 spin columns (GE Healthcare) were used to purify the end-labeled primer.

Telomerase activity assay

Reactions (20 µl) contained 1X human telomerase buffer, 5 nM of ^{32}P-end-labeled primer as indicated in the figure legends and dNTPs at cellular relevant concentrations (24 µM dATP, 29 µM dCTP, 37 µM dTTP, 5.2 µM dGTP) and varying concentrations of 6-thio-dGTP (TriLink) as indicated. The reactions were started by the addition of 3 µl of immunopurified telomerase eluent, incubated at 37ºC for 1 hour, then terminated with 2 µl of 0.5mM EDTA and heat-inactivated at 65ºC for 20 minutes. An equal volume of loading buffer (94% formamide, 0.1XTBE, 0.1% bromophenol blue, 0.1% xylene cyanol) was added to the reaction eluent. The samples were heat denatured for 10 min at 100°C and loaded onto a 14% denaturing acrylamide gel (7M urea, 1X TBE) and electrophoresed for 90 min at constant 38W. Samples were imaged using a Typhoon phosphorimager (GE Healthcare). Percent primer extension was calculated with ImageQuant TL 8.2 by measuring the intensity of each product band and dividing by the total radioactivity in the lane or total products, as indicated in the figure legends. Processivity was calculated as previously described[56,57].

Dot blot quantification of telomerase concentration

The concentration of telomerase pseudoknot RNA in the eluted telomerase preparation was measured as described. Briefly, a serial dilution of in vitro transcribed pseudoknot region of hTR (Supplementary Fig. [1]) was prepared as standards for quantification (0.1, 0.5, 1, 5, 10, 50, 100, 250 fmol µL^{-1}). An aliquot of each standard and eluted telomerase (10 µl) was added to 90 µl of formamide buffer (90% formamide, 1× tris–borate EDTA (TBE)). The samples were incubated at 70 °C for 10 min and then placed on ice. Positively charged Hybond H+ membranes and Whatman filter papers (GE Healthcare Life Sciences) pre-incubated with 1× TBE were assembled onto the GE manifold dot blot apparatus and the samples were loaded onto the membrane via vacuum blotting. The membrane was air dried and then UV-crosslinked using a Stratagene Stratalinker 1800 with the Auto-Crosslink program. The membrane was prehybridized at 55 °C in 25 ml of Church buffer (1% BSA, 1 mM EDTA pH 7.5, 500 mM Na_2HPO_4 pH 7.2, 7% SDS) for 30 min. A total of 1×10^6 CPM of ^{32}P-labeled hTR oligonucleotide probe (Table 1) was added to the hybridization buffer and incubated overnight at 55 °C. The membrane was washed 3× with 0.1× SSC, 0.1× SDS buffer. After vacuum sealing, the membrane was exposed to a phosphorimager screen for 1–3 h and imaged using a Typhoon scanner. ImageQuant TL 8.2 was used to quantify the blot intensities for the standard curve.

POT1 and TPP1 purification

Full-length human POT1 was expressed as a SUMOstar-(His)6- POT1 fusion protein in baculovirus-infected SF9 cells (Thermo Fisher Scientific), as previously described[58]. POT1 was first purified using a His-Trap column (GE Healthcare) and eluted with 200mM imidazole. After tag cleavage with SUMOstar protease (Ulp1 variant, LifeSensors), the protein was further purified by Superdex 200 size-exclusion chromatography (GE Healthcare Life Sciences) in 25 mM Tris-Cl (pH 8) and 150 mM NaCl. Purified TPP1-N (amino acids 89–334) protein was obtained from soluble lysates of isopropyl β-D-thiogalactopyranoside-induced BL21(DE3) pLysS cells (Promega) after nickel agarose chromatography, treatment with Ulp1 protease to cleave the Smt3 tag31 and size-exclusion chromatography. Expression was induced with 0.8 mM IPTG in cells for about 13 h at 24 °C, and then harvested by centrifugation at 4500 rpm for 20 min. Cell pellets were lysed in buffer (20 mM Tris pH 7.5, 500 mM NaCl, 10 mM imidazole) with a protease inhibitor cocktail (Roche Molecular Biochemicals). Following sonication, the lysate was centrifuged 40,000 rpm for 75 min at 4 °C. The supernatant was filtered through a 0.2 micron filter and loaded onto a HisTrap FF column (GE LifeSciences), followed by washing and elution with 20 and 200 mM imidazole, respectively, using an ATKA Pure FPLC (GE Healthcare). Fractions containing TPP1 were concentrated and exchanged into buffer (25 mM Tris pH 8.0, 150 mM NaCl, 5 mM DTT) using a Centricon-10 device (Amicon). The sample was incubated with SUMO (Ulp1) protease (Invitrogen) overnight at 4 °C with gentle mixing by rotation at 20 rpm to cleave the tag. Samples were then loaded on a HiLoad 16/600 Superdex 200 column (GE Healthcare). Eluted fractions containing TPP1 were collected and pooled. Protein concentration was determined by Bradford Assay (BioRad) and purity was determined by SDS–PAGE and Coomassie staining.

Electrophoretic mobility shift assay

Variable concentrations (0-80nM) of Telomerase protein were mixed with 2.5 nM flourescein labeled DNA (Table 1) in binding buffer (20 mM HEPES-KOH pH 7.5, 100 mM KCl, 0.5 mM MgCl2, 0.5 mM TCEP-HCl, 0.05% v/v IGEPAL Co-630, 8% glycerol, 50 µg/mL bovine serum albumin) and incubated for 30 min at room temperature (22ºC).10 µL was separated on a 4-20% polyacrylamide-TBE gel in 1x TBE buffer. Gels were imaged using the near-IR setting of a Typhoon scanner (GE).

Telomerase and Primer Preparation

Minimal human telomerase LD555 labeled at U42 was produced as described previously.[19,23] Briefly, telomerase was reconstituted in rabbit reticulocyte lysate supplied with in vitro transcribed CR4/5 239-325 and U42 LD555 PK 32-195 fragments as well as pNFLAG hTERT plasmid and purified via an N-terminal FLAG tag. Single-stranded primer $(TTAGGG)_3$ was purchased with a 5’ biotin and a C6 amino modifier at T6 from the 3’ end. Oligo was labeled with Cy5-NHS and HPLC purified using a C8 column.

Single-Molecule FRET Data Acquisition and Processing

Slides were prepared as described previously and assembled using biocompatible double-sided tape. Telomerase binding reactions were set up at 5uL using 3uL hTelomerase, 1uL 5nM Cy5 primer in T50 (50mM Tris-HCl pH 8.3, 50mM LiCl) and 1uL Telomerase Imaging Buffer LiCl (TIBL, 50mM Tris-HCl pH 8.3, 50mM LiCl, 10mM Trolox, 3mM MgCl2, 0.8% Glucose).

Reactions were incubated at room temperature for 30 minutes, diluted to 40uL using TIBL and immobilized on a PEGylated quartz slide. The solution was incubated on the slide for 10 minutes before washing with 60uL of TIB KCL (TIBK, 50mM Tris-HCl pH 8.3, 50mM KCl, 10mM Trolox, 3mM MgCl2, 0.8% Glucose) containing 1% glucose-oxidase. Histogram data was taken by recording intensity values of molecules across 20 fields of view for 2 seconds each. Next, channels are washed with activity buffer containing dATP, dTTP and either dGTP or 6-thio-dGTP in TIBK. Long movies are taken upon mounting of the slide while histogram data as described above is recorded at 5, 15 and 30 minutes.

Movies were analyzed using in-house MatLab scripts. Briefly, an algorithm finds individual molecules, performs background subtraction and records green and red fluorescence intensities from which it calculates a FRET values. FRET values are imported into Prism where they are binned into a histogram.

Table 1. Oligo Table

Name	**Sequence**
Oligo1	GGTTAGGGTTAGGGTTAG
Oligo1-6dGlast	GGTTAGGGTTAGGGTTA/6dG/
Oligo1-6dGcentral	GGTTAGGGTTAGG/6dG/TTAG
Oligo2	GTTAGGGTTAGGGTTAGG
Oligo2-6dGlast	GTTAGGGTTAGGGTTAG/6dG/
Oligo2-6dG2ndlast	GTTAGGGTTAGGGTTA/6dG/G
Oligo2-two6dGend	GTTAGGGTTAGGGTTAG/6dG/6dG/
Primer A5	TTAGGGTTAGCGTTAGGG
EMSAoligo1	TTCAGAG/ifluorT/CTGACGGTTAGGGTTAGGGTTAG
EMSAoligo2	TTCAGAG/ifluorT/CTGACGGTTAGGGTTAGGGTTA/6dG/
hTR dot blot probe	CGGTGGAAGGCGGCAGGCCGAGGC

References

1. de Lange T. Shelterin: the protein complex that shapes and safeguards human telomeres. *Genes Dev*. 2005;19(18):2100-2110. doi:10.1101/gad.1346005

2. Lim CJ, Cech TR. Shaping human telomeres: from shelterin and CST complexes to telomeric chromatin organization. *Nat Rev Mol Cell Biol*. 2021;22(4):283-298. doi:10.1038/s41580-021-00328-y

3. Levy MZ, Allsopp RC, Futcher AB, Greider CW, Harley CB. Telomere end-replication problem and cell aging. *J Mol Biol*. 1992;225(4):951-960. doi:10.1016/0022-2836(92)90096-3

4. Cong YS, Wright WE, Shay JW. Human Telomerase and Its Regulation. *Microbiol Mol Biol Rev*. 2002;66(3):407-425. doi:10.1128/MMBR.66.3.407-425.2002

5. Avilion AA, Piatyszek MA, Gupta J, Shay JW, Bacchetti S, Greider CW. Human telomerase RNA and telomerase activity in immortal cell lines and tumor tissues. *Cancer Res*. 1996;56(3):645-650.

6. Zhang X, Mar V, Zhou W, Harrington L, Robinson MO. Telomere shortening and apoptosis in telomerase-inhibited human tumor cells. *Genes Dev*. 1999;13(18):2388-2399.

7. Shay JW, Bacchetti S. A survey of telomerase activity in human cancer. *Eur J Cancer Oxf Engl 1990*. 1997;33(5):787-791. doi:10.1016/S0959-8049(97)00062-2

8. Wu RA, Upton HE, Vogan JM, Collins K. Telomerase Mechanism of Telomere Synthesis. *Annu Rev Biochem*. 2017;86:439-460. doi:10.1146/annurev-biochem-061516-045019

9. Hofmann WK, Lübbert M, Hoelzer D, Phillip Koeffler H. Myelodysplastic syndromes. *Hematol J Off J Eur Haematol Assoc*. 2004;5(1):1-8. doi:10.1038/sj.thj.6200335

10. Parker, Mufti. Ineffective haemopoiesis and apoptosis in myelodysplastic syndromes. *Br J Haematol*. 1998;101(2):220-230. doi:10.1046/j.1365-2141.1998.00708.x

11. Steensma DP, Fenaux P, Van Eygen K, et al. Imetelstat Achieves Meaningful and Durable Transfusion Independence in High Transfusion-Burden Patients With Lower-Risk Myelodysplastic Syndromes in a Phase II Study. *J Clin Oncol Off J Am Soc Clin Oncol*. 2021;39(1):48-56. doi:10.1200/JCO.20.01895

12. Mascarenhas J, Komrokji RS, Palandri F, et al. Randomized, Single-Blind, Multicenter Phase II Study of Two Doses of Imetelstat in Relapsed or Refractory Myelofibrosis. *J Clin Oncol*. 2021;39(26):2881-2892. doi:10.1200/JCO.20.02864

13. Mender I, Gryaznov S, Dikmen ZG, Wright WE, Shay JW. Induction of Telomere Dysfunction Mediated By the Telomerase Substrate Precursor 6-Thio-2’-Deoxyguanosine. *Cancer Discov*. 2015;5(1):82-95. doi:10.1158/2159-8290.CD-14-0609

14. Sanford SL, Welfer GA, Freudenthal BD, Opresko PL. Mechanisms of telomerase inhibition by oxidized and therapeutic dNTPs. *Nat Commun*. 2020;11:5288. doi:10.1038/s41467-020-19115-y

15. Sanford SL, Welfer GA, Freudenthal BD, Opresko PL. How DNA damage and non-canonical nucleotides alter the telomerase catalytic cycle. *DNA Repair*. 2021;107:103198. doi:10.1016/j.dnarep.2021.103198

16. Ghanim GE, Fountain AJ, van Roon AMM, et al. Structure of human telomerase holoenzyme with bound telomeric DNA. *Nature*. 2021;593(7859):449-453. doi:10.1038/s41586-021-03415-4

17. Greider CW. Telomerase is processive. *Mol Cell Biol*. 1991;11(9):4572-4580. doi:10.1128/mcb.11.9.4572-4580.1991

18. Chen JL, Greider CW. Template boundary definition in mammalian telomerase. *Genes Dev*. 2003;17(22):2747-2752. doi:10.1101/gad.1140303

19. Jansson LI, Hentschel J, Parks JW, et al. Telomere DNA G-quadruplex folding within actively extending human telomerase. *Proc Natl Acad Sci*. 2019;116(19):9350-9359. doi:10.1073/pnas.1814777116

20. Parks JW, Stone MD. Coordinated DNA dynamics during the human telomerase catalytic cycle. *Nat Commun*. 2014;5(1):4146. doi:10.1038/ncomms5146

21. Latrick CM, Cech TR. POT1–TPP1 enhances telomerase processivity by slowing primer dissociation and aiding translocation. *EMBO J*. 2010;29(5):924-933. doi:10.1038/emboj.2009.409

22. Rice C, Shastrula PK, Kossenkov AV, et al. Structural and functional analysis of the human POT1-TPP1 telomeric complex. *Nat Commun*. 2017;8:14928. doi:10.1038/ncomms14928

23. Weinrich SL, Pruzan R, Ma L, et al. Reconstitution of human telomerase with the template RNA component hTR and the catalytic protein subunit hTRT. *Nat Genet*. 1997;17(4):498-502. doi:10.1038/ng1297-498

CHAPTER 5: Future directions for continuation of this study

Introduction

Despite its importance in human health and disease, telomere biology is still not fully understood and remains an active area of research. The high repetitiveness of telomere DNA presents a particular challenge to understanding the organization of telomeric protein and nucleosomes and thus the mechanisms that contribute to telomere maintenance. A second challenge that have hindered progress in dissecting telomere maintenance mechanisms is the inability to produce large amounts of homogeneous samples of functional telomerase enzyme. This limits many common biochemical methods that are traditionally used to study enzyme mechanisms. Single-molecule methods, on the other hand, only require small sample sizes and are thus ideally suited to study telomerase. In addition, single-molecule Förster Resonance Energy Transfer (smFRET) adds the ability to monitor inter- and intramolecular dynamics during biological processes at high spatiotemporal resolution. This feature is lacking in traditional biochemical methods. Therefore, smFRET is particularly appropriate for *in vitro* investigations of the dynamics that underlie the mechanisms of telomere organization and maintenance. During my graduate studies, I have made exciting progress in leveraging smFRET to study several aspects of telomere maintenance. Here, I will describe this progress and the challenges that have prohibited completion of these projects. I will first describe my progress in using smFRET applications of Zero-Mode Waveguides (ZMWs) to study telomerase enzyme kinetics and discuss possible future applications of the method. Next, I will elaborate on my progress in using total internal reflection microscopy (TIRF) to monitor telomerase recruitment dynamics at telomeres in real-time. In addition, I will discuss how adding complexities to this system could enable us to better understand factors that affect telomerase recruitment *in vivo*. Finally, I will discuss how we can leverage existing methods to study C-strand fill in, a process that occurs after telomerase-mediated 3’ end extension of the

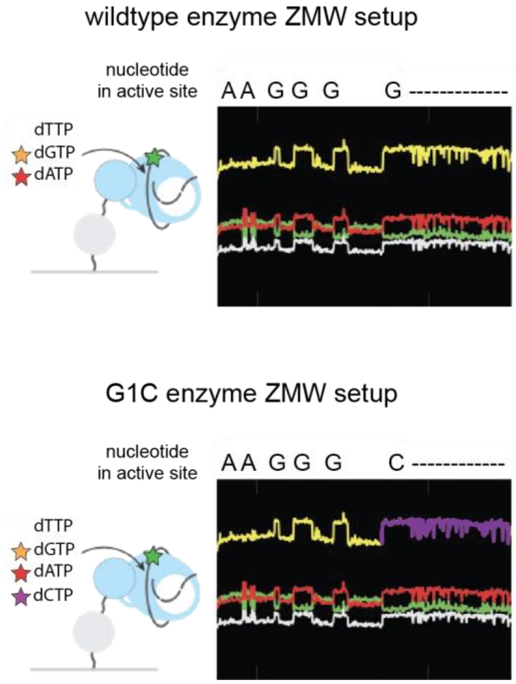

Figure 1. Modified ZMW experiment setup to decipher stretches of dGTP signal. Top. The traditional ZMW setup utilizes dye-labeled dGTP and dATP to monitor their proximity to the active site as determined by anticorrelation to donor dye intensity near the active site. Consecutive dGTP incorporations make assignment of signals to individual dGTP incorporations impossible. **Bottom**. A modified setup utilizes a mutant enzyme where the middle C in the RNA template switched to a G, resulting in incorporation of G instead of C in nascent telomere DNA. Using a dye-labeled dCTP in addition to the other two labeled nucleotides will allow for us to distinguish incorporation of the different dGTP positions.
telomere, to produce a double-stranded telomere segment.

Dissecting the mechanism of telomerase template translocation using ZMW

The unique feature of template translocation during the telomerase catalytic cycle has remained an intriguing field of study. As outlined in chapter II of this thesis, our lab has made large strides in determining detailed kinetic properties of dNTP incorporation into nascent telomere DNA by telomerase. However, these findings also provided novel observations whose underlying biochemical mechanisms remain obscured. The first observation that we made in the data were long pauses in dNTP residence in the active site after the incorporation of the dG at the end of the template region (G6), which we attribute to template translocation. After this pause, we consistently observed long stretches of dGTP residence in the active site prior to successful dGTP incorporation as signified by a loss in FRET signal (see chapter II, Fig.

S10). Template translocation occurs after the incorporation of the first G in the 'GGG' stretch of a telomeric repeat, meaning that the first two nucleotides incorporated post-translocation are two guanosines. Because of this, we are unable to determine the significance of the long residence time of dGTP in the active site. We hypothesize that dGTP binding to the active site could occur prior to proper realignment of the template, therefore leading to the enzymes' inability to incorporate this nucleotide and leading to the long residence time. To test this, I designed three template mutants that separately carry a guanosine at one of the cytosine residues in the RNA template.

We termed these mutants G6C for the GGTTA$\underline{G_6}$ position, G1C for the $\underline{G_1}$GTTAG and G2C for the G$\underline{G_2}$TTAG positions, indicating the position of G → C incorporation in nascent telomere DNA. Using these mutants, we can modify the ZMW assay conditions and add Cy5.5-labeled dCTP to detect incorporation of dCTP at the template mutant location (Fig. 1). This way, we can determine which nucleotide has increased residence time in the active site prior to incorporation and provide closer insight into the kinetics and molecular mechanism of template translocation.

I successfully produced all three template mutants using our established RRL reconstitution system and U42 LD555-labeling and splint ligation of the mutant hTR fragments (Table 1). With the mutants in hand, I first tested their catalytic activity using primer extension assays as previously described. I focused my efforts on the G1C mutant, since we hypothesized that this nucleotide exhibited extended residence time in the telomerase active site while template translocation occurred. I performed experiments comparing G1C activity to wildtype enzyme on both wildtype (TTAGGG)$_3$ primer and on mutant (TTAG$\underline{C}$G)$_3$ primer. Our results yielded interesting observations. While the G1C enzyme showed activity on both primers, the resulting banding pattern was different from that of wildtype enzyme, even on wildtype primer (Fig. 2, lane 1 and 2). The wildtype enzyme exhibits the usual banding pattern indicating template translocation after G6, signified by increased intensity at that position.

While the G1C enzyme also exhibits these bands, the second and third repeats have high intensity bands at the G2 and T2 positions and the A position, respectively. In addition, primer extension halts after the third repeat is completed, indicating that either the G1C enzyme stalls and is unable to translocate the template or that it dissociates from the DNA primer entirely. In addition, a G → C substitution at any location in the telomere DNA prevents G-quadruplex formation. G-quadruplexes have previously been shown to be important for telomerase processivity[1], so a failure to form stable G-quadruplexes could explain

Figure 2. Primer extension assay using wildtype and G1C enzyme and wildtype and mutant primers. To test G1C enzyme activity, we compared its activity on a wildtype $(TTAGGG)_3$ primer to that of wildtype enzyme (lane 1 and 2). To test of the C→G mutation in the template affects telomerase binding to wildtype primer, we also tested the mutant enzyme using complementary mutant $(TTAGCG)_3$ enzyme (lane 3).

the decreased processivity of G1C enzyme. It remains unclear why enzyme function halts after the third full repeat is synthesized and could present an opportunity for further exploration.

Surprisingly, G1C activity on C1G primer, whose sequence is complementary to the RNA template, is limited compares to wildtype primer. Even in the presence of dCTP, enzyme activity is very weak and terminates after two full repeats are synthesized (Fig. 2, lane 3). In addition, even though hard to decipher, it seems the T1 and A in the first repeat and the G1 in the second repeat have higher intensity bands. This indicates increased enzyme dissociation at that primer position. Enzyme dissociation after G1 instead of the G6 position after the first newly synthesized repeat indicates that incorporation of four cytosines into a telomere primer promotes telomerase dissociation. While speculatory, this again suggests that a lack of G-quadruplex formation is responsible for this observation.

While these results are intriguing, I did not have time to further explore G1C mutant function and to perform the ZMW experiment using the G1C or other template mutants. This is an exciting opportunity for a future student to continue. Eventually, the goal of this study is to extend the ZMW assay to include POT1-TPP1-TIN2 (PTT). PTT has been shown to increase telomerase processivity, so performing the ZMW assay on PTT-bound DNA primer will provide valuable insight into the kinetics, and mechanism, of template translocation and processivity[2,3]

Table 1. Oligo Table

Oligo Name	**Sequence**
G1C hTR fragment	5' G.G.G.C.C.A.U.U.U.U.5-LC-N-U.U.G.U.C.U.A.A.C.G.C.U.A.A.C.U.G.A.G.A.A 3'
G2C hTR fragment	5' G.G.G.C.C.A.U.U.U.U.5-LC-N-U.U.G.U.C.U.A.A.G.C.C.U.A.A.G.U.G.A.G.A.A 3'
G6C hTR fragment	5' G.G.G.C.C.A.U.U.U.U.5-LC-N-U.U.G.U.G.U.A.A.C.C.G.U.A.A.C.U.G.A.G.A.A 3'
G1C splint	CAGCGCGCGGGGAGCAAAAGCACGGCGCCTACGCCCTTCTCAGTTAGCGTTAGACAAAAAATGGCCACCACCCCTCCCAG
G2C splint	GGGGAGCAAAAGCACGGCGCCTACGCCCTTCTCAGTTAGGCTTAGACAAAAAATGGCCACCACCCCTCCCAGG
G6C splint	CAGCGCGCGGGGAGCAAAAGCACGGCGCCTACGCCCTTCTCAGTTACGGTTAGACAAAAAATGGCCACCACCCCTCCCAGG

Real-time detection of telomerase recruitment to telomeres

From the very first day in the Stone Lab, I was determined to find out how telomerase finds the very 3’ end of the telomere. Telomerase faces several intriguing challenges in binding the very 3’ end of each telomere. Telomerase is fairly scarce during its window of activity, telomeres and associated factors are highly repetitive and telomere DNA is protected by shelterin proteins.[4,5]

I first set out to build a model telomere consisting of both double-and single stranded regions to closely resemble *in vivo* conditions. To this end, I was provided with a plasmid (pRST5) that carries 270 basepairs of telomeric repeats (Fig. 3A). I amplified this plasmid using DH10Beta cells and ampicillin selection and purified it using a maxiprep kit (Qiagen). I then doube-digested the plasmid using BamHI and HindII restriction enyzymes to excise the telomere sequence from the plasmid. Since telomere DNA is highly repetitive, we had concerns over using standard procedures for the purification of the excised DNA fragment from an agarose gel. To prevent any DNA “slipping” during the purification, we opted to try an electroelution approach rather than the usual gel extraction. Here, I used a razorblade to cut a well into the agarose downstream of the sample well (Fig 3B). Alternatively, I could have used

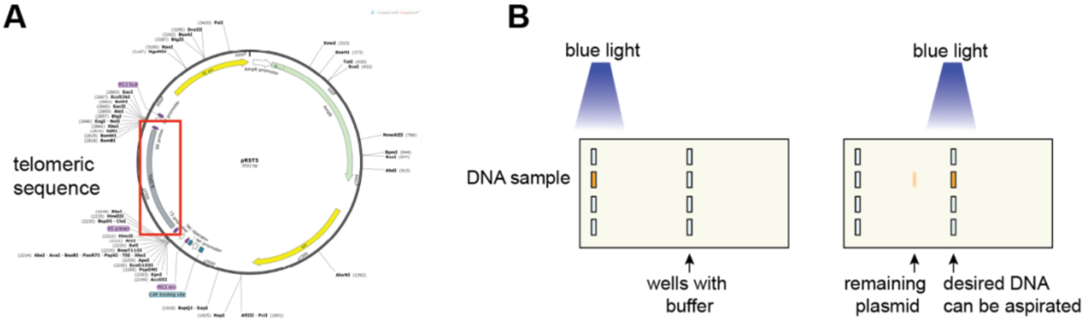

Figure 3. Concept of long telomere DNA production. A. Plasmid map of pRST5, which was used to excise a ~270 nt telomeric DNA piece. **B.** cartoon representation of the SYBRsafe and blue light strategy to electroeluted telomeric DNA.

a second comb to create a downstream well. To visualize the DNA, I used SYBR safe DNA stain rather than ethidium bromide due to DNA integrity concerns. DNA stained with SYBR safe can be visualized using blue light. I then loaded the sample and made sure the buffer level does not exceed the gel height to ensure DNA will not diffuse into the buffer. I ran the gel at standard conditions and followed the DNA band using the blue light. Once the DNA eluted into the downstream well, I used a micropipette to aspire the eluted DNA. Note that I had to refill the well with running buffer for continued elution of any DNA left in the gel. I then confirmed DNA concentration by nanodrop, and ethanol precipitated the DNA. While this method worked to some degree, it was very challenging to achieve high yields. In addition, for the purpose of my study I needed to modify the DNA not only with a biotin, but also with a Cy5 dye, both of

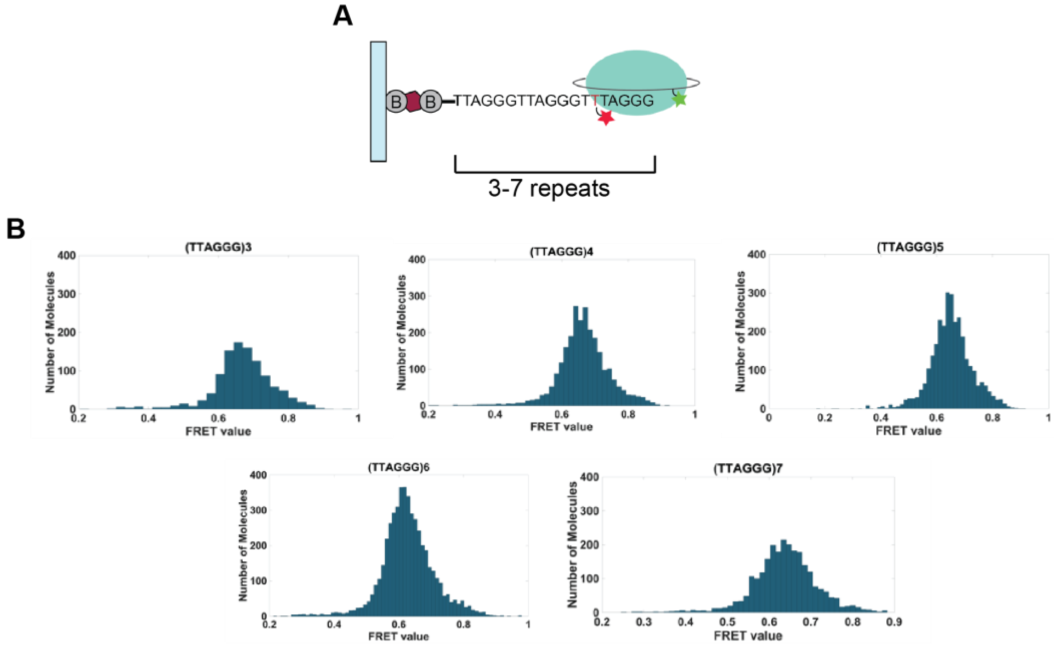

Figure 4. Telomerase binds telomeric substrates of varying lengths. A. Cartoon representation of the smFRET setup. LD555-lbeled telomerase is incubated with excess Cy5-labeled DNA primer. Primer is pulled down on the slide surface via a biotin-streptavidin linkage. **B.** Histogram representation of the FRET distribution of telomerase molecules pulled down on DNA primers ranging in size from three to seven TTAGGG repeats, with the labeling site at the same position from the 3' end.

which would have been too challenging for my time frame. Therefore, we opted to move on with synthetic ssDNA (IDT) of varying lengths (4-7 telomere repeats) that come modified with a 5’ biotin and an amino-modified thymine base toward the 3’ end. That being said, the electroelution methodology proved itself very useful for the purpose of purifying telomeric DNA and could be exploited by current and future students.

I used NHS-Cy5 (Cytiva) to label each of the telomeric DNA oligos. I next wanted to test whether each of these constructs result in the same FRET value upon being bound by telomerase. To this end, I incubated each DNA oligo with our U42-LD555 labeled reconstituted telomerase and visualized telomerase binding events using our total internal reflection (TIRF) microscopy smFRET setup (Fig. 4A). I found that each of the DNA: telomerase complexes produced the same ~0.65 FRET state (Fig. 4B). However, different DNA constructs produced different amounts of bound telomerase molecules. This could be attributed to varying labeling efficiencies of these oligos, as the concentration was only determined by DNA concentration, not by fluorescence intensity. Because previous studies have already characterized the difference in accessibility of different telomeric ssDNA constructs due to G-quadruplex formation, I decided not to focus on this aspect.[6] Instead, my next step was to perform live flow assays of telomerase onto these constructs. I constructed flow channels that were controlled by a 0.2-gauge syringe needle inserted into tubing on one end, while inserting the tubing on the other end into a microcentrifuge tube filled with the desired buffer (Fig. 5A). I first immobilized 20 uL of 125 pM $(TTAGGG)_3$ DNA (3R) onto the slide, followed by a thorough wash with TIB (KCl) (Fig. 5B, left). I then started recording a movie under green excitation and pulled ~200 pM telomerase in TIB spiked with gloxy into the channel (Fig. 5B, middle). I was able to observe arrival of telomerase by an increasing number of fluorescent spots in the green channel. Over the course of 200 seconds, I observed telomerase-DNA binding events by the emergence of fluorescence in the red channel (Fig. 5B, right). To analyze the data, I used in-house MatLab scripts that found all stable binding events at the very end of the movie. I used MatLab to create a histogram of the FRET states of all molecules, which resulted in a broad peak centered at around 0.75 FRET (Fig. 6A). Upon analysis of hundreds of individual binding events, I found that telomerase binding to the 3’ end occurred instantaneously without any discernable telomerase search behavior (Fig. 6B). Binding of telomerase was stable, and I did not see dissociation of telomerase molecules prior to Cy5 bleaching. The lack of observable telomerase-DNA dynamics prior to stable binding suggests that our time resolution of 100 ms might not be high enough to reveal any dynamics that may happen. I next sought to understand how occupancy of the model telomere by TIN2-POT1-TPP1 (TPT) affects telomerase-DNA dynamics. To this end, I added 200nM of purified TPT complex, provided by the Nguyen Lab at LMC Cambridge, to the DNA prior to addition of telomerase. This experiment resulted in only one successful telomerase binding event (Fig 6D), a large difference in the hundreds of binding events we saw on naked DNA. This could be due to the protective mechanism of TPT or by telomerase sequestration by TPT molecules on the slide surface. Quartz slide surfaces are known to be sticky towards proteins, and so TPT could

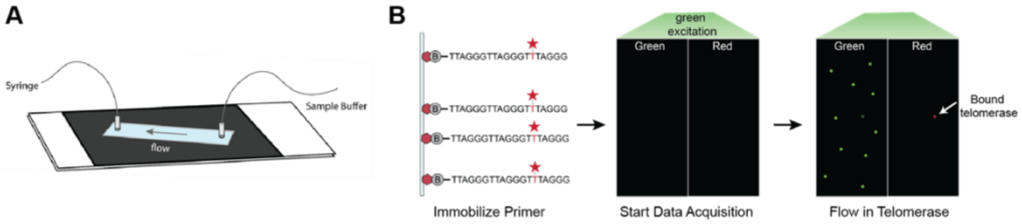

Figure 5. Setup and data collection of a flow smFRET experiment. A. Cartoon representation of a flow channel. Holes are drilled into the quartz slide prior to PEGylation. Black biocompatible double-sided tape is cut to the size of a cover slip, and a channel is cut out of the center. Tubing is attached to either hole using a tubing scaffold to reduce sample volume in the tubing but ensure fixing of the tubing in the hole. They are secured by applying epoxy. A syringe needle is attached to the outlet tubing while the inlet is placed in a buffer reservoir. This allows for negative pressure to pull buffer through the channel. **B.** Cartoon representation of the data collection process. DNA oligo is immobilized at 10pM until density is sufficient. Green laser is turned on and the data collection is started. Being careful not to move the slide, buffer containing ~600pM telomerase is pulled into the sample chamber until LD555 intensity is observed. Data is then collected for as long as is desired.

have been immobilized on the slide independent of DNA. Analysis of the data revealed that there were many telomerase-DNA encounters that did not produce any FRET, as indicated by an increase in green fluorescence without an increase in red fluorescence (Fig. 6D, left arrow). This is indicative of telomerase arriving at the DNA-TPT complex away from the 3’ end. However, I also observed transient, dynamic FRET states that I analyzed and binned into a histogram. The resulting histogram has a wide FRET distribution, indicative of highly dynamic telomerase-DNA encounters (Fig 6C). Our data suggests that presence of TPT decreases

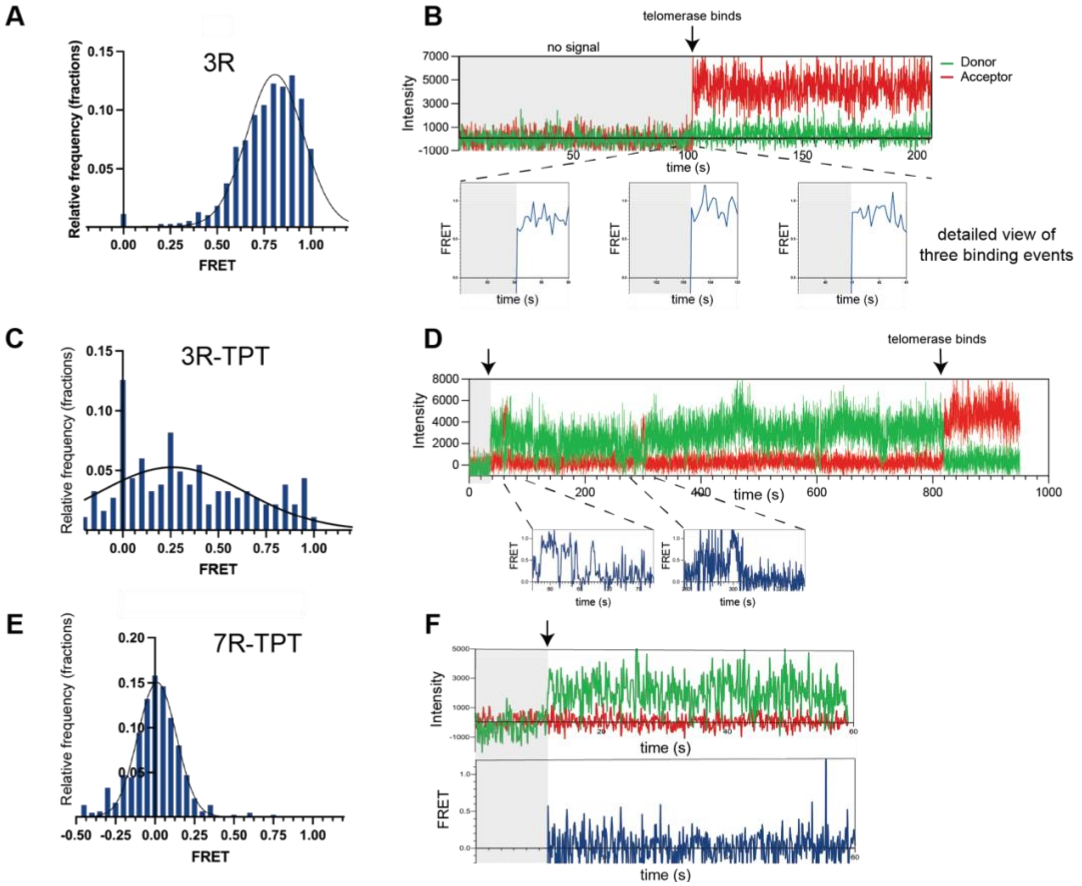

Figure 6. Results of telomerase flow experiments on 3 and 7-repeat DNA primer +/- TPT. A. Histogram data of all FRET events using a naked 3-repeat DNA primer and telomerase. **B.** Example trace of a telomerase molecule binding a DNA primer. Binding is instantaneous; detail of the FRET change of three binding events is shown below. **C.** Histogram data of all FRET events using a 3-repeat DNA primer bound by TPT. **D.** Intensity and FRET plot of the only binding events observed in the 3R-TPT data set. Blown up in detail are FRET events that did not result in stable binding. Arrows indicate arrival of telomerase at the DNA (left) and stable binding of telomerase to 3’ DNA (right). **E.** Histogram Data of all FRET events using a 7-repeat primer bound by TPT. A zero FRET indicates arrival of telomerase at the DNA primer, but insufficient proximity to the acceptor dye towards the 3’ end to result in FRET. **F.** Example trace showing telomerase arriving at the DNA (arrow) and lack to produce any FRET change, indicative of its inability to access the 3’ end.

telomerase binding efficiency. It also suggests that telomerase has transient access to the 3’ end as indicated by the short and highly dynamic FRET instances, but that this does not always lead to a stable binding event (Fig. 6C).

We next sought to understand how multiple TPT present on telomere DNA affect telomerase recruitment behavior. To this end, we repeated the experiment with a DNA construct that carries seven telomeric repeats (7R) that can in theory be bound by three TPT complexes.[7] This experiment showed many telomerase-DNA encounters with a lack of FRET and no productive binding events (Fig 6E and F). This indicates that telomerase is interacting with the DNA but cannot access the 3' end. These results suggest that the presence of multiple TPT complexes on telomere DNA prevents telomerase access, consistent with precious studies that shows that POT1 inhibits telomerase activity.[8] However, these results contradict our finding that TPT-telomerase interactions promote telomerase recruitment (see chapter 3).

This experimental setup has many caveats including sticky slides and might not be ideally suited for its purpose. Improvements to the slide surface quality and of the experimental setup could make this assay very powerful. However, if we have reached the limits of this assay in a TIRF setup, this assay could be pursued using ZMWs (see chapter 2).

This assay is also well suited for changing the experimental conditions. While exciting, performing this experiment on naked DNA does not adequately represent physiological conditions and thus might not accurately reflect the *in vivo* telomerase search mechanism. However, by using increasingly complex DNA constructs, this assay could be a powerful way to explore how different telomere factors affect telomerase. For example, our lab has recently started to explore how the telomere proteins TRF1 and TRF2 affect nucleosome dynamics and DNA accessibility. Exploring how to re-design and optimize this assay to include telomeric nucleosomes and telomere proteins could be an exciting thesis project for a future student. This would be particularly exciting since recent cryo-EM efforts have discovered that human telomerase RNA associates with the histone proteins H2A and H2B.[9] This assay could be a powerful tool to explore the role of histone proteins in telomerase recruitment and function.

I hope that future students will further explore telomerase recruitment using this thesis as a guide.

Beyond telomerase: the P-to-P switch mechanism and its stimulation by the CST complex

Telomerase is essential for the maintenance of human telomere length. However, a second polymerase is responsible for synthesizing the C-rich strand of the telomere to produce duplex DNA in a process called C-strand fill in. This enzyme is called Primase-Polymerase α (PP) and is a heterotrimeric protein comprised of two primase and two polymerase chains, which form the primase and polymerase domains, respectively. C-strand fill in occurs in three fundamental phases. In the first, PP binds the telomeric ssDNA with its primase catalytic subunit and produces an RNA primer. Once the primer reaches a length of 7-10 nucleotides, a switch in active sites is triggered.[10,11] This switch is termed the P-to-P switch and describes the transfer of the RNA primer from the primase to the polymerase active site. Once this switch is completed, a DNA-RNA hybrid is created, and polymerase synthesizes DNA until it reaches the 5' end of the telomere DNA junction. While recent structural data has revealed some aspects of the mechanism of the P-to-P switch, its entire molecular mechanism and underlying dynamics is unknown.[12] In addition, a telomere-specific protein complex called CST (Ctc1-Stn1-Ten1) has been shown to promote this switch by an unknown mechanism.[13] Here, in collaboration with Neal Lue at Cornell Medical school, we set out to understand the molecular mechanism of the P-to-P switch and its stimulation by the CST complex. Previous *in vitro* work from the Lue lab has shown that CST presence decreases the length of the RNA primer that is synthesized prior to the switch and that it promotes polymerase activity. However, biochemical assays are not able to reveal the mechanism behind these observations. Instead, we designed a single- molecule FRET assay that reports on DNA-RNA dynamics during PP

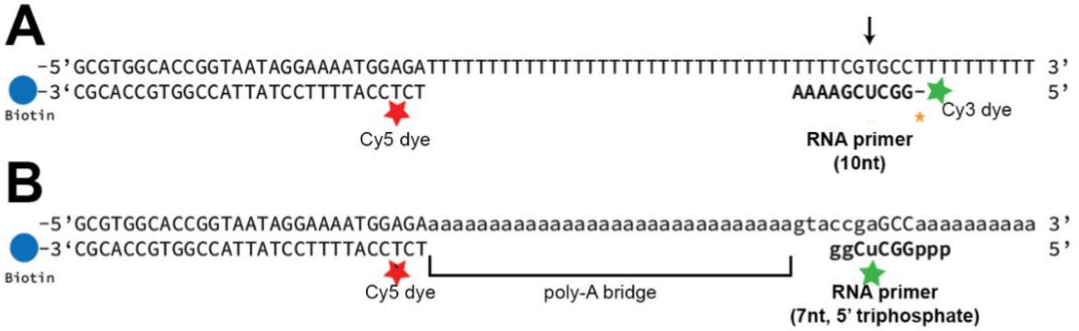

Figure 7. Cartoon Schematic of changes to the initial smFRET setup to study the P-to-P switch. A. Previous design. The arrow indicates a nucleotide mismatch that could prevent primer binding. A yellow asterisk indicates a missing 5' triphosphate cap required for primase activity. **B.** Improved design. The primer sequence contains more G and C nucleotides to increase melting temperature. The poly-A-stretch was switched to poly-T to prevent random primase activity.

catalysis. Preliminary work in our lab had used a single-molecule FRET setup with fluorescent dyes on the DNA and the RNA primer, which resulted in a stable FRET state (Figure 7A). Addition of PP to this construct resulted in a highly dynamic FRET behavior, indicating that PP changes DNA conformation. Upon analysis of the experimental setup, I noticed some problems. First, literature has shown that PP requires a 5' triphosphate at the RNA primer to function properly, a feature that was lacking in the current setup (Fig. 7A, yellow star).[14] I also noticed that there was a nucleotide mismatch in the RNA primer (Fig. 7A, arrow). I re-designed the RNA primer sequence to match the DNA template and increased the GC content to increase the melting temperature for more stable binding. I also added a second, 7-nucleotide RNA primer (MB41) as previous studies have shown that the original primer length of 10 nucleotides (MB42) would force the primer into the polymerase active site, meaning we would not be able to observe the switch.[15] The 10-nucleotide RNA primer will be used to obtain a post-switch FRET signature. Finally, I changed the internal 30-nucleotide poly-T sequence to a poly-A sequence to prevent aberrant PP activity. PP requires a pyrimidine to initiate primer synthesis.[16,17] With this change, PP cannot initiate uncontrolled primer synthesis on the poly-A sequence, which results in clean data. With this new construct, I could observe DNA dynamics during PP catalysis and possibly identify DNA dynamics unique to the P-to-P switch (Fig. 7B). I first obtained FRET data of the construct without PP to establish a starting point. Initial results indicated that the poly-A bridge of 30 nucleotides was too long to result in FRET between the Cy5 and Cy3 dyes. In addition, the annealing efficiency of the 7 nucleotide RNA primer was very low, and I only saw 11 Cy3 spots. I then redesigned the DNA construct with 10- and 20-nucleotide poly-A sequences and changed the protocol from annealing the RNA primer to flowing it onto the DNA on the slide. Experiments with the two new DNA constructs resulted in FRET values of 0.4 for the 20-nucleotide poly-A stretch and 0.6 for the 10-nucleotide poly A stretch (Fig. 8A and B). Changing the RNA addition strategy to a flow-in post DNA immobilization was successful and we observed thousands of FRET events.

Prior to the addition of PP to our FRET constructs, the Lue lab performed activity assays to ensure that PP was active on it and able to extend the RNA primer. To this end, they first used radiolabeled dCTP or dTTP to the constructs in the presence of either RNA. Results showed that

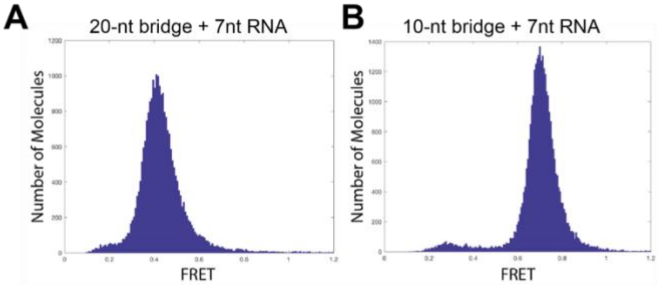

Figure 8. Histogram representation of smFRET data indicating primer bound to DNA template. A. MB41 primer labeled with Cy3 bound to ssDNA with a 20-nucleotide bridge to the double-stranded portion of the DNA construct, which is labeled with acceptor dye Cy5. This construct results in a FRET value of ~0.45. **B.** The same primer bound to a ssDNA with a 10-nucleotide bridge. This construct results in a higher FRET of ~0.7.

the 7-nucleotide primer resulted in very low activity (Fig. 9A). In contrast, PP produced RNA-dDNA hybrid products that terminate after less than 20 nucleotides in length from the MB42 primer. In addition, a small high molecular weight band can be observed, which we hypothesize represents a primer with 30 nucleotides of T added to it, at which point it terminates because no other dNTPs are present. They next tested whether CST will promote PP activity. Interestingly, PP showed activity on MB41 primer in the presence of CST only when dCTP and dATP were added in addition to dTTP (Fig 9B). CST was able to promote the synthesis of high molecular weight products from

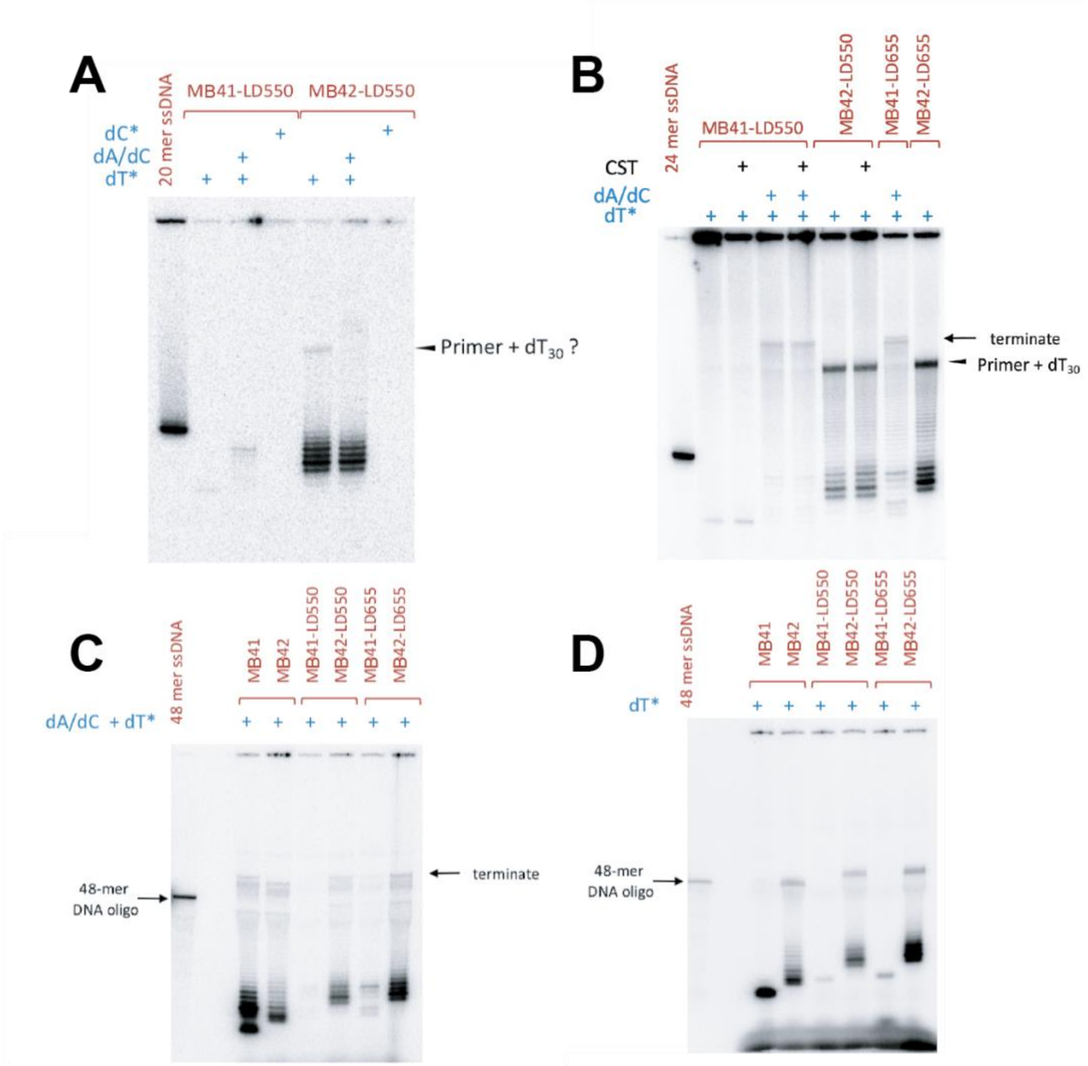

Figure 9. Primer extension assays using *C. glabrata* PP and our new primer design. A. The extension of RNA primers MB41-LD550 and MB42-LD550 by PP were tested in the presence of radiolabeled dTTP and dCTP. A radiolabeled 20-mer DNA was used as a loading and length control. **B.** Stimulation of PP activity by CST was tested using both RNA primers with either LD555 or LD655 fluorescent dyes and radiolabeled dTTP. **C.** Comparison of the PP-mediated extension of dye-labeled RNA and unlabeled RNA primers in the presence of dCTP, dATP and radiolabeled dTTP. **D.** Comparison of the PP-mediated extension of dye-labeled RNA and unlabeled RNA primers in the presence of only radiolabeled dTTP.

the 10-nucleotide primer, indicating that CST stimulates the switch from the primase to the DNA polymerase active site of PP (Fig. 9B). This also suggested that the length of the MB42 primer did not force it into the DNA polymerase active site, as CST would not show any effect on DNA polymerase activity in this assay. Thus, this primer was still

suited for P-to-P switch experiments in the smFRET setup. We next wanted to ensure that the Cy5 dye on the RNA did not interfere with PP activity. The Lue lab repeated the previous experiments with both labeled and unlabeled primers and found that presence of the dye inhibited PP activity on the MB41 primer (Fig. 9D and D. We thus decided to continue our smFRET experiments with the MB42 primer.

I next tested if PP addition to our construct affected the FRET state of it and whether I could observe DNA dynamics indicative of PP DNA handling dynamics. I added 20nM of purified PP to the slide channel and obtained both histogram data from 20 fields of view as well as long movies for analysis of dynamics in individual complexes. The histogram data suggested that addition of PP was destabilizing to the DNA-RNA hybrid as indicated by a large increase in zero FRET peak compared to naked DNA data (Fig. 10A).

However, the overall FRET behavior of the population was largely unchanged, with the exception of the mid-FRET peak broadening a bit. I thus decided to analyze single-molecule traces to get a better understanding of the broadening. I discovered that compared to the -PP control, about 20% of molecules exhibited considerable dynamics when PP was present (Fig. 11). This indicates that PP is binding and manipulating the DNA-RNA hybrid. However, the dynamic behavior had no discernable pattern to it, so it remains unclear what the significance of each FRET state is. We thus decided to include 8- and 9-

nucleotide primers in our assay to possibly reveal pre- and post- P-to-P switch states. Our reasoning was

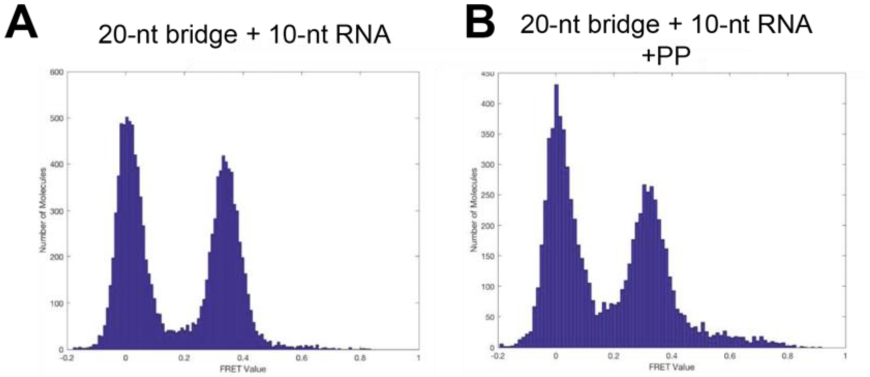

Figure 10. Histogram representation of smFRET data of the naked nucleic acid construct A. In the absence of PP, the nucleic acid construct has sharp FRET peaks at 0 and ~0.35. **B.** Upon addition of PP to the construct, the FRET peak centered at 0.35 widens to include high FRET values (0.4-0.8) and low FRET values (0.2) while the main peak at 0.35 remains.

that a shorter primer will not be as likely to trigger the switch, and we could assign a FRET state to pre- and post-switch states. Due to other projects taking priority as well as concerns over the age and thus integrity of the PP complex, I stopped work on this project at that time in hopes to continue it later. However, the exciting work presented in chapter 3 kept me away from this project. Currently, a new graduate student is pursuing this project. Upon discussion of the FRET data with the Lue lab, they decided to not pursue a FRET construct with labeled nucleic acids since it considerably limited our observation of any protein dynamics. Therefore, they decided to switch to labeled PP complex. This work is currently underway and has shown some exciting success in purification of the complex from bacterial cells.

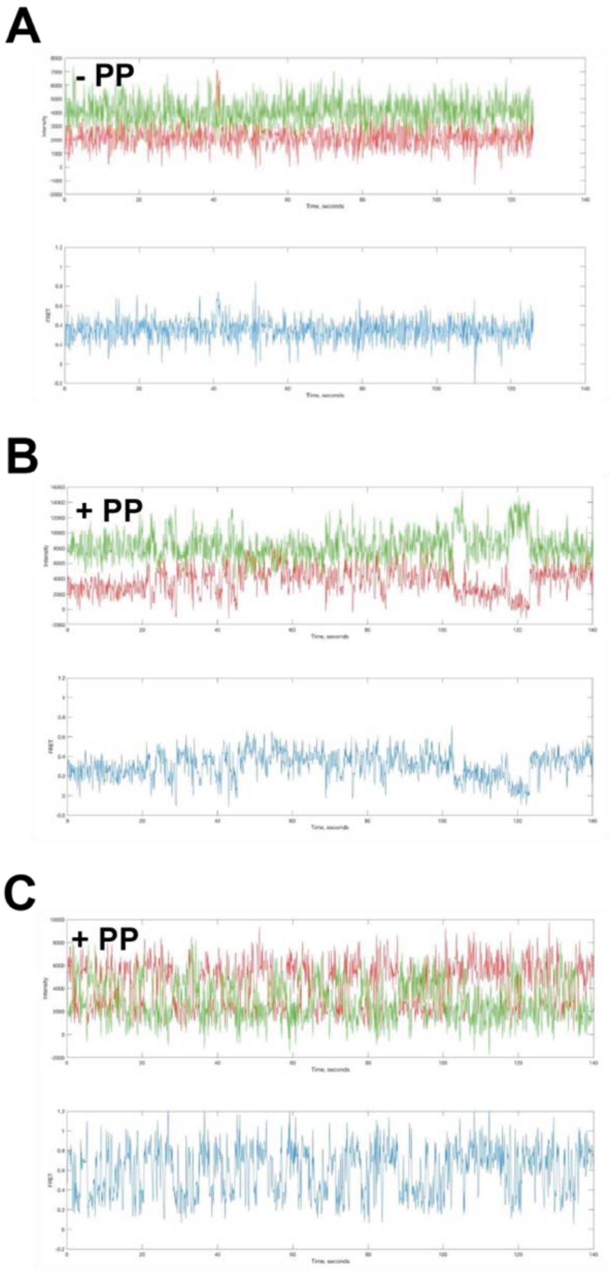

Figure 11*.* Analysis of single MB42 molecules bound to DNA substrate in absence and presence of PP. A. A representative single-molecule FRET trace of the naked nucleic acid construct. The FRET is steady at about 0.3 and does not exhibit any dynamic behavior. **B and C.** Representative single-molecule traces of the nucleic acid construct bound by TPT. Upon addition of PP to the nucleic acid construct, about 20% of molecules observed exhibited considerable dynamics as shown here. This represents PP altering of the DNA structure between the RNA primer and the double-stranded DNA portion of the DNA construct.

Table 2. Oligo Table

Oligo Name	**Sequence**
DNA handle	5’-TC/iAmMC6T/CCATTTTCCTATTACCGGTGCCACGC/3Bio/- 3’
30-nt bridge	5’-GCGTGGCACCGGTAATAGGAAAATGGAGAAAAAAAAAAAAAAAAAAAAAAAAAAAAAAGTACCGAGCCAAAAAAAAAA – 3’
7-nt RNA/ MB41	5’ - GGCU*CGG – 3’
10-nt RNA/ MB42	5’ - GGCU*CGGUAC – 3’
20-nt bridge	5’-GCGTGGCACCGGTAATAGGAAAATGGAGAAAAAAAAAAAAAAAAAAGTACCGAGCCAAAAAAAAAA – 3’
10-nt bridge	5’-GCGTGGCACCGGTAATAGGAAAATGGAGAAAAAAAAAAGTACCGAGCCAAAAAAAAAA - 3’

References

1. Jansson LI, Hentschel J, Parks JW, et al. Telomere DNA G-quadruplex folding within actively extending human telomerase. *Proc Natl Acad Sci*. 2019;116(19):9350-9359. doi:10.1073/pnas.1814777116

2. Wang F, Podell ER, Zaug AJ, et al. The POT1-TPP1 telomere complex is a telomerase processivity factor. *Nature*. 2007;445(7127):506-510. doi:10.1038/nature05454

3. Pike AM, Strong MA, Ouyang JPT, Greider CW. TIN2 Functions with TPP1/POT1 To Stimulate Telomerase Processivity. *Mol Cell Biol*. 2019;39(21):e00593-18. doi:10.1128/MCB.00593-18

4. Xi L, Cech TR. Inventory of telomerase components in human cells reveals multiple subpopulations of hTR and hTERT. *Nucleic Acids Res*. 2014;42(13):8565-8577. doi:10.1093/nar/gku560

5. Lim CJ, Cech TR. Shaping human telomeres: from shelterin and CST complexes to telomeric chromatin organization. *Nat Rev Mol Cell Biol*. 2021;22(4):283-298. doi:10.1038/s41580-021-00328-y

6. Hwang H, Kreig A, Calvert J, et al. Telomeric Overhang Length Determines Structural Dynamics and Accessibility to Telomerase and ALT-Associated Proteins. *Structure*. 2014;22(6):842-853. doi:10.1016/j.str.2014.03.013

7. Smith EW, Lattmann S, Liu ZB, Ahsan B, Rhodes D. Insights into POT1 structural dynamics revealed by cryo-EM. *PLOS ONE*. 2022;17(2):e0264073. doi:10.1371/journal.pone.0264073

8. Kelleher C, Kurth I, Lingner J. Human Protection of Telomeres 1 (POT1) Is a Negative Regulator of Telomerase Activity In Vitro. *Mol Cell Biol*. 2005;25(2):808-818. doi:10.1128/MCB.25.2.808-818.2005

9. Ghanim GE, Fountain AJ, van Roon AMM, et al. Structure of human telomerase holoenzyme with bound telomeric DNA. *Nature*. 2021;593(7859):449-453. doi:10.1038/s41586-021-03415-4

10. Sheaff RJ, Kuchta RD, Ilsley D. Calf Thymus DNA Polymerase .alpha.-Primase: “Communication” and Primer.cntdot.Template Movement between the Two Active Sites. *Biochemistry*. 1994;33(8):2247-2254. doi:10.1021/bi00174a035

11. Kuchta RD, Reid B, Chang LM. DNA primase. Processivity and the primase to polymerase alpha activity switch. *J Biol Chem*. 1990;265(27):16158-16165. doi:10.1016/S0021-9258(17)46202-8

12. He Q, Lin X, Chavez BL, Agrawal S, Lusk BL, Lim CJ. Structures of the human CST-Polα–primase complex bound to telomere templates. *Nature*. 2022;608(7924):826-832. doi:10.1038/s41586-022-05040-1

13. Lue NF, Chan J, Wright WE, Hurwitz J. The CDC13-STN1-TEN1 complex stimulates Pol α activity by promoting RNA priming and primase-to-polymerase switch. *Nat Commun*. 2014;5(1):5762. doi:10.1038/ncomms6762

14. Yan J, Holzer S, Pellegrini L, Bell SD. An archaeal primase functions as a nanoscale caliper to define primer length. *Proc Natl Acad Sci*. 2018;115(26):6697-6702. doi:10.1073/pnas.1806351115

15. Yuan Z, Georgescu R, Li H, O'Donnell ME. Molecular choreography of primer synthesis by the eukaryotic Pol α-primase. *bioRxiv*. Published online May 3, 2023:2023.05.03.539257. doi:10.1101/2023.05.03.539257

16. Hay RT, Hendrickson EA, DePamphilis ML. Sequence specificity for the initiation of RNA-primed simian virus 40 DNA synthesis *in vivo*. *J Mol Biol*. 1984;175(2):131-157. doi:10.1016/0022-2836(84)90471-6

17. Yamaguchi M, Hendrickson EA, DePamphilis ML. DNA primase-DNA polymerase alpha from simian cells: sequence specificity of initiation sites on simian virus 40 DNA. *Mol Cell Biol*. 1985;5(5):1170-1183.